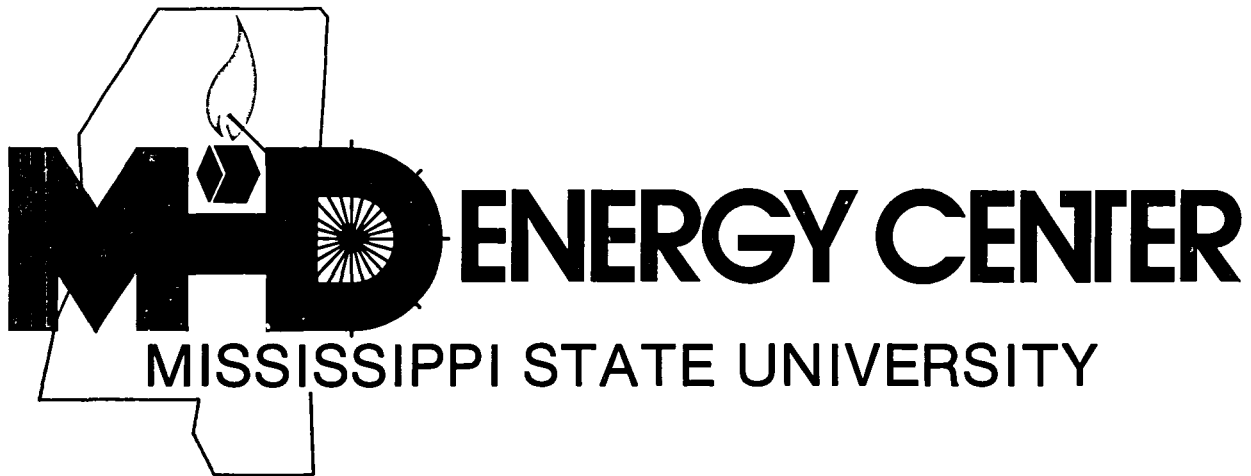# CARS TEMPERATURE MEASUREMENTS
IN THE
FUEL PREBURNER OF THE SPACE SHUTTLE MAIN ENGINE:
A FEASIBILITY STUDY

NASA-CR-170764
19830017507

ENERGY CENTER

MISSISSIPPI STATE UNIVERSITY

E. J. BEITING and J. C. LUTHE

NF02675

CONTRACT NAS8-34907

MARCH, 1983

CARS Temperature Measurements

in the

Fuel Preburner of the Space Shuttle Main Engine: A Feasibility Study

By

E. J. Beiting and J. C. Luthe

MHD Energy Center
Mississippi State University
Mississippi State, MS 39762

Contract NAS8-34907

March, 1983

Table of Contents

List of Figures

List of Figures (continued)

I. *Introduction*

A. Scope

This report discusses the feasibility of making temperature profile measurements in the fuel preburner of the main engine of the space shuttle (SSME) using coherent anti-Stokes Raman spectroscopy (CARS). The principal thrust of the work is to identify problems associated with making CARS measurements in high temperature gas phase hydrogen at very high pressures ($\sim$ 400 atmospheres). To this end a theoretical study was made of the characteristics of the CAR spectra of H_2 as a function of temperature and pressure and the accuracy with which temperatures can be extracted from this spectra. In addition the experimental problems associated with carrying out these measurements on a SSME at NSTL were identified. A conceptual design of a CARS system suitable for this work is included.

Many of the results of the calculations made in this report are plotted as a function of temperature. In the course of presenting these results, it was necessary to decide whether the number density or the pressure should be treated as a fixed parameter. During a test firing, the SSME is throttled and the fuel preburner acts neither as a constant density nor a constant pressure environment. Since most physical quantities scale with number density rather than pressure (linewidth, optical dispersion, CARS signal strength, etc.) it was decided to present results holding density constant. The unit of density used throughout this report is the amagat (1 amagat density equals the density of a gas at 1 atmosphere pressure at 0° C). Conversion from density to pressure is accomplished via the equation of state. For convenience Appendix A presents isotherms for hydrogen gas for the pressures, densities and temperatures of interest in this study.

B. Characteristics of the Fuel Preburner

The following values were stated as design criteria for the temperature profiling system in RFP No. 8-1-2-EC-25732 and are taken as the characteristics of the preburner where measurements are required.

1. Temperature of gas:
   a. Steady state 2100 R° (1167 K)
   b. Transient maximum 3000 R° (1667 K)
   c. Normal minimum 1500 R° (833 K)

1

d. Transient minimum 200 R° (111 K)

2. Gas composition from H_2 to Steam + H_2 + O_2.

3. Gas velocity: $\sim$ 200 fps (61 m/sec) maximum.

4. Chamber pressure: 5500 psi (374 atmospheres).

5. Combustion chamber material: Haynes 188 + Zirconium Oxide Coating.

6. Coating (wall) temperature: 2100 R° (1167 K)

7. Measurement accuracy: 10 R° (5.6 K)

8. Measurement resolution:

   a. Thermal - 10 R° (5.6 K)

   b. Spatial - from 0.25 to 0.50 inch square (1.6 to 3.2 cm^2)

9. Time Response: 10 milliseconds

Hydrogen and oxygen are fed into the fuel preburner in equal amounts by weight and hence lead to the reaction 16 H_2 + O_2 → $2H_2O$ + 14 H_2. Presumably this reaction takes place near the injector head and is completed by the time the gas mixture reaches the ends of the baffle plates and ports (see Figures 20a and 21b). Because little oxygen is expected to be present in the line of sight of the ports, it was decided at the initial contractor's meeting that there would be little point in studying O_2 as a probe species. In accordance with discussions held at Marshall Space Center and NSTL, the gas streamlines in the preburner are assumed to be steady except at the center. The maximum duration of a test firing is 500 seconds. Information on the fuel preburner, the SSME test stand, instrument accessibility to the preburner, physical environment adjacent to the preburner during a test run, etc. can be found in Section VII.

C. Background

CARS is a relatively new combustion diagnostic tool that is undergoing rapid development [1,2,3]. It is an example of four-wave mixing in which three photons, usually two at a pump frequency ω_1 and one at a Stokes frequency ω_2 mix through the third order susceptibility of a medium to produce a fourth or anti-Stokes photon at frequency ω_3. The intensity of the anti-Stokes beam I_3 can be written

$$I_3 = \left(\frac{4\pi^2\omega_3}{c^2}\right)^2 I_1^2 \, I_2 \, |x|^2 \, z^2$$

where I_1 and I_2 are the pump and Stokes laser beam intensities, z is the

length in which these beams coherently interact and χ is the third order susceptibility of the medium which consists of a frequency dependent resonant part, $\chi' + i\chi''$, and a nonresonant part, χ_{nr}. When the frequency difference $\omega_1 - \omega_2$ approaches the frequency of a Raman active energy resonance of a major species in the bulk media, the resonant susceptibility becomes large compared to the non-resonant susceptibility. Because the intensity depends on the absolute value squared of the total susceptibility, the spectra appears as a resonant modulation on a non-resonant background.

The resonant susceptibility is a function of the number density and the population difference between the levels involved in the transitions. This latter dependence means that the spectrum of a ro-vibration band of a molecule will be temperature sensitive since the population distribution of the rotational energy levels is governed by the Boltzman factor. Hence the temperature, number density, and bulk non-resonant susceptibility of the medium must be known in addition to the molecular parameters in order to theoretically model the CAR spectra of a molecular species in a multi-component gas medium. The bulk non-resonant susceptibility is obtained from a knowledge of the individual susceptibilities of the component gases and their approximate relative concentrations. The temperature can be obtained by examining the CAR spectrum of a major species. Comparison of the experimental spectra to calculated spectra has been the most reliable method of extracting accurate temperature information. Several excellent reviews of the theory and applications of CARS which discuss these considerations are available in the literature [4,5].

The accuracy with which temperature measurements can be made using CARS depends to a large extent on how well the CAR spectra of the chemical species under study can be theoretically modeled. The molecules present in the preburners are H_2, O_2, and H_2O, all of which have been successfully modeled for atmospheric pressure CARS combustion studies [6,7,8]. However, the complexity of the water spectra with its many closely spaced rotational lines invites one to consider this species for thermometry only as a last alternative. Since hydrogen will be the major species in the fuel preburner, it is the species of choice for temperature measurements. Oxygen is a trace species after combustion occurs and in accordance

3

with the above discussion will not be considered in this study.

In many respects, H_2 is an ideal molecule for CARS thermometry. It has widely spaced rotational levels ($B_e = 60.85$ cm^{-1}) reducing the number of rotational energy levels populated at elevated temperatures and hence reducing the number of Q-branch spectral lines. In addition it has a large vibration-rotation interaction constant ($\alpha_e = 3.06$ cm^{-1}) leading to widely spaced rotational lines. These properties mean that the individual intensities of the few and widely spaced rotational lines can be studied which greatly simplifies analysis. Furthermore, the energy difference between the lowest and first excited vibrational levels is so great ($\simeq 4400$ cm^{-1}) that no significant population of this excited level is expected even at the maximum expected temperatures. The small linewidth pressure broadening coefficient (.0015 cm^{-1}/amagat) and the large spacing between rotational lines ($\simeq 20$ cm^{-1}) indicates that spectral lines will not overlap even at the high densities present in the preburner.

Thermometry using the broadband CAR spectra of H_2 has been performed in an atmospheric pressure H_2-air diffusion flame [6,7]. The relative intensity peaks of individual rotational lines were used to extract the temperatures in a range of 900 K to 2100 K. Standard deviations of 2% - 8% were obtained with the poor precision due to the low signal-to-noise ratios that are characteristic of low number density environments.

II. _Calculated H$_2$ CAR Spectra_

There are several methods that can be used to extract temperature measurements from CAR spectra. Three are considered in this report. Two are simply variants of measuring intensity of individual ro-vibrational lines or groups of lines and these are discussed in Sections VI and VII. The third is to record all the rotational lines in a given spectral interval (i.e. 100 cm^{-1}) and to compare this data with a library of computed spectra calculated for the expected experimental conditions and temperatures. This method is perhaps the surest and most accurate method of extracting temperature from the spectra since many lines are observed and anomalies can be easily detected. However, it is more difficult and expensive to implement than the other methods.

Calculation of non-linear spectra, such as CARS, of a multiline molecular species is considerably more complex than the prediction of linear absorption or emission spectra. Much of this complexity is caused by the interference that takes place among the transitions and the interaction of these transitions with the nonresonant background. A synopsis of the theory used to calculate CAR spectra is presented here. Various details can be found in the appendices. An effort has been made to point out some of the approximations used and limits of this theory.

In general, the dipole moment per unit volume $\vec{P}$ induced in a medium by electric fields $\vec{E}(\vec{r},i)$ can be written

$$\vec{P}(\vec{r},i) = \sum_{n=1}^{\infty} \vec{P}^{(n)}(\vec{r},i)$$

$$= \sum_{n=1}^{\infty} \chi^{(n)}(\omega_1,\omega_2,..\omega_n)\ \vec{E}(\vec{r},1)\ \vec{E}(\vec{r},2)...\vec{E}(\vec{r},n)$$

(1)

where $\vec{r}$ is the space coordinate, i represents the polarization of the field, ω is the angular frequency and $\chi^{(n)}$ is the susceptibility tensor of rank n + 1. If one considers only isotropic or centrosymmetric media, all even-numbered terms in this sum are zero because of inversion symmetry. Then, truncating the series at n = 3, Eq. (1) can be written as

$$P_\alpha(\vec{r},i) = \chi^{(1)}_{\alpha\beta}(\omega_1)E_\beta(\omega_1) + \chi^{(3)}_{\alpha\beta\gamma\delta}(\omega_1,\omega_2,\omega_3)\ E_\beta(\vec{r},1)E_\gamma(\vec{r},2)E_\delta(\vec{r},3)$$

(2)

where the summation over repeated indices convention is used.

In general, $\chi^{(3)}$ has 81 elements. However, for isotropic media only 21 are nonzero, of which only 3 are independent [9]

$$\chi_{1111} = \chi_{xxxx} = \chi_{yyyy} = \chi_{zzzz}$$

$$\chi_{1122} = \chi_{xxyy} = \chi_{yyxx} = \chi_{xxzz} = \chi_{zzxx} = \chi_{yyzz} = \chi_{zzyy}$$

$$\chi_{1212} = \chi_{xyxy} = \chi_{yxyx} = \chi_{xzxz} = \chi_{zxzx} = \chi_{yzyz} = \chi_{zyzy}$$ $\qquad$ (3)

$$\chi_{1221} = \chi_{xyyx} = \chi_{yxxy} = \chi_{xzzx} = \chi_{zxxz} = \chi_{yzzy} = \chi_{zyyz}$$

with $\quad \chi_{1111} = \chi_{1122} + \chi_{1212} + \chi_{1221}$

Most practical applications of CARS use the same frequencies for two of the E fields (three-color CARS) making $\chi_{1122} = \chi_{1212}$, since $\chi^{(3)}$ is invariant to the six permutations of the pairs (β,ω_1), (γ,ω_2), (δ,ω_3). Hence, for this case there are only two independent elements (i.e. $\chi^{(3)}_{1111}$, $\chi^{(3)}_{1221}$).

If the summation of the $\chi^{(3)}$ of Eq. (2) is performed for these conditions, the third order polarization vector becomes [10]

$$\vec{P}^{(3)} = \left[6 \chi^{(3)}_{1122}(\omega_1,\omega_1,-\omega_2)\hat{e}_1(\hat{e}_1 \cdot \hat{e}_2) \right.$$
$$\left. + 3\chi^{(3)}_{1221}(\omega_1,\omega_1,-\omega_2)\hat{e}_2 \right] E(1)^2 E(2)* \qquad (4)$$
$$\times \exp[i(2\vec{k}_1-\vec{k}_2)\cdot\vec{r}]$$
$$= \chi_{CARS}\,\hat{e}_{CARS}\, E(1)^2 E(2)* \exp[i(2\vec{k}_1-\vec{k}_2)\cdot\vec{r}]$$

where the input fields E(1) and E(2) are assumed to be plane waves with polarization vectors $\hat{e}_1$ and $\hat{e}_2$ and wave vectors in the medium of $\vec{k}_1$ and $\vec{k}_2$ ($k = n\omega/c$, $n = \sqrt{1 + 4\pi\chi^{(1)}}$). If the Stokes and pump fields are parallel ($\hat{e}_2 = \hat{e}_1$), $\hat{e}_{CARS} = \hat{e}_1$ (the three fields have the same polarization) and

$$\chi_{CARS} = 6\chi^{(3)}_{1122} + 3\chi^{(3)}_{1221}\,(\omega_1,\omega_1,-\omega_2) = 3\chi^{(3)}_{1111}\,(\omega_1,\omega_1,-\omega_2) \qquad (5)$$

If the polarizations of the Stokes and pump fields are perpendicular ($\hat{e}_1 \perp \hat{e}_2$), the anti-Stokes polarization is parallel to the Stokes field ($\hat{e}_{CARS} = \hat{e}$) with

$$\chi_{CARS} = 3\chi^{(3)}_{1221}\,(\omega_1,\omega_1,-\omega_2). \qquad (6)$$

In this latter configuration, the CARS susceptibility is less than in the first configuration by the term $6\chi^{(3)}_{1122}$.

6

Substitution of the linear polarization $P^{(1)}$ into Maxwell's equations leads to the usual plane wave solution with frequency and polarization vector unchanged but with wave vector $k = \frac{n\omega}{c}$ where $n = \sqrt{1 + 4\pi\chi^{(1)}}$. Similarly, one can obtain an expression for the intensity of the CARS wave with Maxwell's equations using Eq. (4) for $P^{(3)}$. If, in addition to the above restrictions, it is assumed that

1. all input fields are plane monochromatic waves,
2. the polarization vector is written as an expansion of plane wave frequencies,
3. the CARS wave is a plane wave whose amplitude can be a function of longitudinal position, and
4. $\Delta k \equiv 2k_1 - k_2 - k_3 \ll 2k_3$,

then the time-averaged intensity of the anti-Stokes wave created in a length ℓ is given by [10]

$$I_3 = \frac{16\pi^4\omega_3^2}{n_1 n_2 n_3 c^4} \; |\chi_{CARS}|^2 \; I_1^2 I_2 \ell^2 \left[\frac{\sin(\Delta k\ell/2)}{\Delta k\ell/2}\right]^2. \tag{7}$$

For exact phase matching $\Delta k = 0$ and

$$I_3 = \frac{16\pi^4\omega_3^2}{n_1 n_2 n_3 c^4} \; |\chi_{CARS}|^2 \; I_1^2 I_2 \ell^2 \tag{8}$$

The frequency dependence of χ_{CARS} is obtained from a quantum mechanical calculation of the microscopic molecular dipole moment arising from the third power of the microscopic fields. Averaging this over all molecular orientations and multiplying the result by the specie number density yields the bulk dipole moment $P^{(3)}$. $\chi^{(3)}$ is obtained as the coefficient of the various third order products. Using diagrammatic perturbation theory one obtains 24, four-fold sums over all molecular states [11]. If

1. all terms containing no Raman resonant terms in the denominator are lumped into a nonresonant term, χ_{NR},
2. there are no one- or two-photon resonances, and
3. the Stokes and pump fields have parallel polarizations $(\hat{e}_1 = \hat{e}_2)$,

then χ_{CARS} can be written in terms of the differential cross section for

spontaneous Raman scattering, $\frac{d\sigma}{d\Omega}$, for two stationary states (k and n) of the molecule, viz [10]

$$\chi_{CARS} = \chi_{NR} + \frac{(N_n-N_k)\hbar_1 c}{\hbar n_2 \omega_2^4} \left(\frac{d\sigma}{d\Omega}\right) \frac{1}{\Omega_{kn}-\omega_1+\omega_2-i\gamma_{kn}} \qquad (9)$$

where N_i is the number density in the ith state, Ω_{kn} is the energy difference between states k and n, and γ_{kn} is the homogeneous line half width (HWHM). (Equations (7) and (8) differ by a factor of 1/16 and Eq. (9) differs by a factor of 2 from those given by Ref. [10].)

As noted above, the equations were derived under the assumption that the input radiation is monochromatic. However, all real light sources have finite line widths, and in particular, CARS employed for thermometry on practical combustion systems uses a broadband Stokes field in order to simultaneously view many transitions of molecular species. Yuratich [12] has considered the problem of finite line widths of the incident fields in detail. If the input waves are approximated as stationary stochastic processes, he finds that the anti-Stokes spectral intensity I_3 is given by the double convolution

$$I_3 \propto \int L_1(\omega_1) \left[\int \left| \chi_{CARS}(\omega_2-\omega_1) \right|^2 L_1(\omega_3+\omega_2-\omega_1) L_2(\omega_2) \, d\omega_2 \right] d\omega_1 \qquad (10)$$

where $L_1(\omega_1)$ is the normalized lineshape of the pump intensity (using a single pump laser). $L_2(\omega_2)$ is the normalized lineshape of the Stokes intensity.

Equation (9) is the expression for the susceptibility for a single resonance. A molecule has many closely spaced resonances and the CARS susceptibility will be the sum over all such resonances, i.e.

$$\chi_{CARS} = \chi_{NR} + \frac{Nn_1 c^4}{\hbar n_2 \omega_2^4} \sum_j \frac{\Delta_j \frac{d\sigma}{d\Omega}\Big|_j}{\Omega_j-(\omega_1-\omega_2)-i\gamma_j} \qquad (11)$$

where N is the number density of the Raman active molecule and Δ_j is the population difference between upper and lower vibration-rotation states. Substituting Eq. (11) into Eq. (10) and performing the integrations over frequency intervals where the molecular resonances occur will yield a CAR spectrum for realistic physical situations.

If the line width of the Stokes radiation is assumed to be much greater than the pump laser line width, $\Delta\omega_2 >> \Delta\omega_1$, then the narrow $d\omega_1$ integration can be performed and

$$I_3(\omega_3) \sim \int \left| \chi_{CARS}(\omega_2 - \omega_1^o) \right|^2 \; L_1(\omega_3 + \omega_2 - \omega_1^o) \; L_2(\omega_2) d\omega_2 \qquad (12)$$

where ω_1^o is the center frequency of $L_1(\omega_1)$. Using Gaussian lineshapes for the laser spectral profiles, this integral can be numerically performed to obtain a CAR spectrum. This is the approach used successfully by Hall [14] to generate synthetic CAR spectra of N_2 and CO.

It is possible to integrate Eq. (10) using Lorentzian or Gaussian lineshapes and obtain an analytical solution in terms of the complex error function without resorting to the broad line width approximation. These solutions were obtained for several combinations of Gaussian and Lorentzian lineshapes by Yuratich [12].

Spectra presented in this report were calculated using a computer program based on the analytical solution of Yuratich. Comparisons of CAR spectra of molecular nitrogen using the two methods yield similar results [13].

Evaluation of Eq. (10) begins with the calculation of χ_{CARS}. Rewriting Eq. (11) results in

$$\chi_{CARS} = \chi_{NR} + \sum_j \frac{a_j}{\Omega_j + \omega_2 - \omega_1 - i\gamma_j} \qquad (13)$$

where

$$a_j = \frac{N n_1 c^4}{\hbar n_2 \omega_2^4} \; \Delta_j \frac{d\sigma}{d\Omega} \bigg|_j \; .$$

The rotational selection rules for CARS are the same as those for Raman scattering [10], i.e. $\Delta J = 0, \pm 2$. For forward scattering, the spontaneous Raman cross section can be expressed in terms of the components of the derived polarizability tensor. For the Q branch [14]

$$\frac{d\sigma}{d\Omega}\bigg|_Q = \left(\frac{\omega_2}{c}\right)^4 \frac{\hbar}{2\omega_o} \left[\frac{\alpha^2}{M} + \frac{7}{45} \frac{\gamma^2}{M} b_J^J\right] (v + 1) \qquad (14)$$

where M and ω_o are the reduced mass and molecular oscillator frequency respectively; b_J^J is the Placzek-Teller coefficient [5]; α and γ are the derivatives with respect to internuclear coordinate of the mean molecular

9

polarizability and anisotropy; v is the vibrational quantum number of the initial level. Evaluation of Eq. (14) for the case of H_2 is delineated in Appendix B. The calculation of the population difference Δ_j of Eq. (13) is outlined in Appendix C and the formulae for the energy differences Ω_j are presented in Appendix D. The homogeneous line half widths, γ_j, are functions of temperature and pressure and a discussion of these quantities is presented in Section III. χ_{NR} is a measured constant that must be scaled with number density. The value for the nonresonant susceptibility for deuterium was used in this study [17].

The lineshapes $L(x)$ in Eqs. (10) and (12) may be of any profile. Laser line widths may be Lorentzian

$$L_L(x) = \frac{\gamma_L}{\pi(x^2 + \gamma_L)^2} \; ; \quad \int L_L(x)dx = 1 \qquad (15)$$

or Gaussian

$$L_G(x) = \frac{\exp(-x^2/\gamma_G^2)}{\gamma_G \sqrt{\pi}} \; ; \quad \int L_G(x)dx = 1 \qquad (16)$$

where $\gamma_G = \gamma_L / \sqrt{\ell n 2}$ and γ are HWHM. For multimode laser fields, the output is more closely approximated by a Gaussian profile. Substitution of Eq. (16) into Eq. (12) for the Stokes and pump laser fields and integrating yields broadband CAR spectra. This calculation using the analytical expression of Yuratich is detailed in Appendix E.

H_2 CAR spectra were calculated for a range of temperatures, densities, and Stokes beam widths. Figures (1) and (2) show computed, normalized spectra for two temperatures (800, 1600 K) that span the operating range. The four spectra in each figure show the effects of the variation of number density from 1 amagat (upper row) to 100 amagat (lower row) and the variation of Stokes beam width from 100 cm^{-1} (left column) to 250 cm^{-1} (right column). For all spectra, a Stokes beam center of 14679 cm^{-1} was used, so that the resultant anti-Stokes beam is centered between the Q(0) and Q(5) lines. Appendix F contains a series of such spectra for 800 $\leq$ T $\leq$ 1800 K, at 100 K steps.

The prominent features of the spectra in these figures are the line broadening with increasing temperature and density, and the relative peak intensity rescaling with Stokes beam narrowing. Since the spectral

Top-left panel:

INTENSITY (NORMALIZED)

T = 800 K
ρ = I A
Γ_s = 100 (cm⁻¹)

WAVENUMBER (cm⁻¹)

Top-right panel:

INTENSITY (NORMALIZED)

T = 800 K
ρ = I A
Γ_s = 250 (cm⁻¹)

WAVENUMBER (cm⁻¹)

Bottom-left panel:

INTENSITY (NORMALIZED)

T = 800 K
ρ = 100 A
Γ_s = 100 (cm⁻¹)

WAVENUMBER (cm⁻¹)

Bottom-right panel:

INTENSITY (NORMALIZED)

T = 800 K
ρ = 100 A
Γ_s = 250 (cm⁻¹)

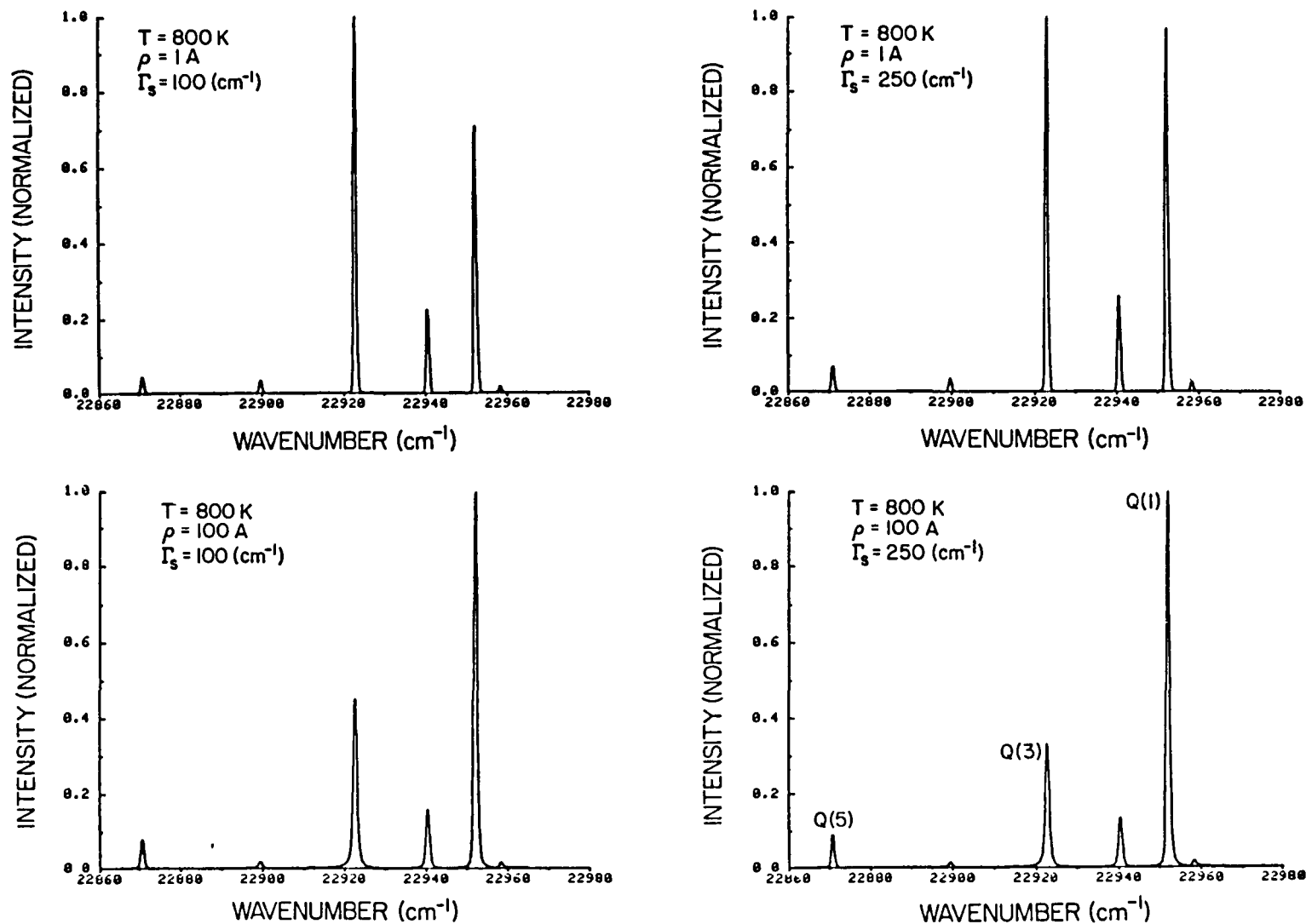Q(1)
Q(3)
Q(5)

WAVENUMBER (cm⁻¹)

Figure 1. Calculated CAR spectra of H_2 for a temperature of 800 K. Spectra were computed for densities of 1 and 100 amagat and Stokes beams with spectral widths of 100 and 250 cm⁻¹. Each spectrum is normalized to the maximum peak intensity for that spectrum.
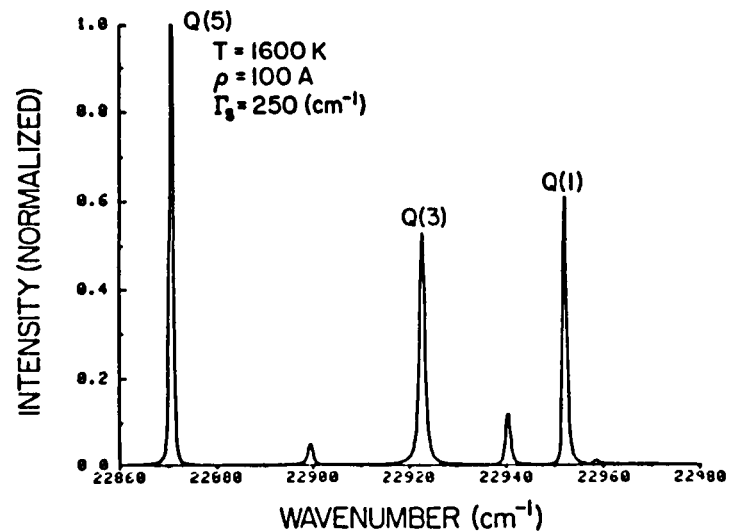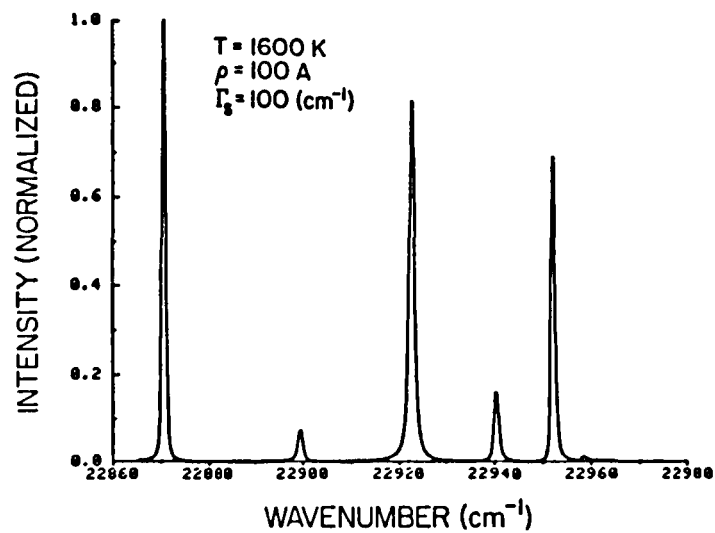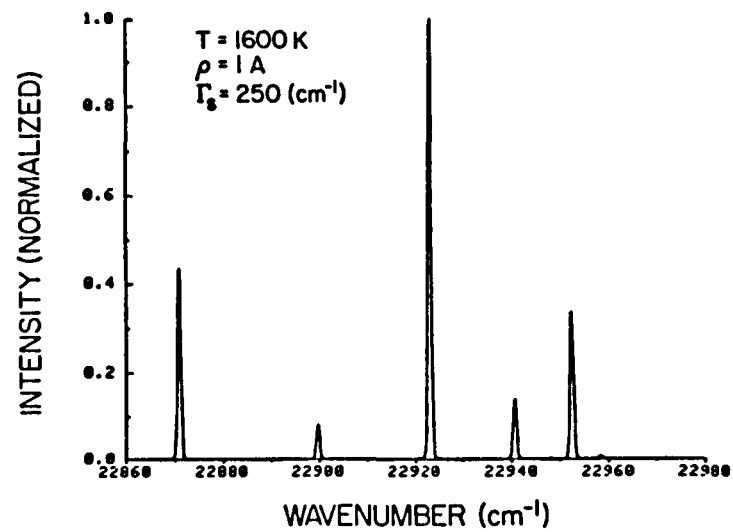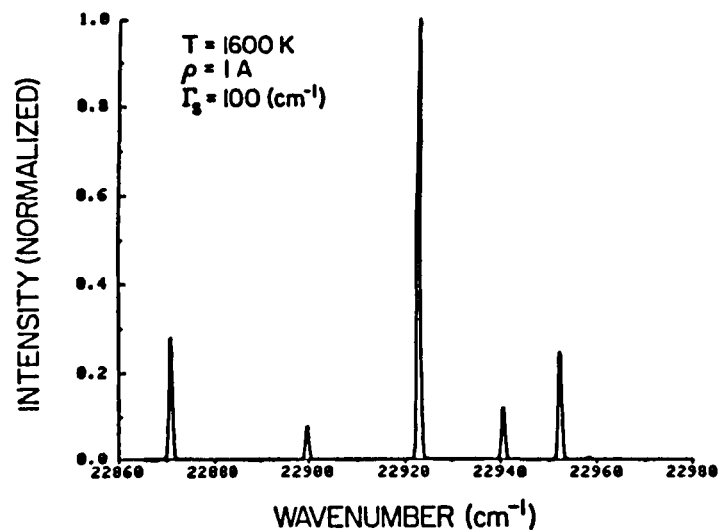
Figure 2. Calculated CAR spectra of H_2 for a temperature of 1600 K. Other details same as those in Figure 1.

extent, Q(0) to Q(5), is about 100 cm^{-1}, the relative peak heights (Q(3)/Q(1), Q(5)/Q(3)) for the 100 cm^{-1} Stokes width compared to the 250 cm^{-1} width differs by a factor of 1.37 and 0.65; i.e. the Q(1) and Q(5) lines are reduced in intensity by factors of 1.37 and 1.53 for 100 cm^{-1} width, thus the ratios differ by the factors 1.37 and 1/1.53.

III. H_2 Linewidth

The calculation of the Raman linewidth of H_2 is extremely important since the power of the CARS signal is inversely proportional to its square or for broadband CARS it is inversely proportional to the linewidth. Furthermore, to extract temperature measurements from the ratio of the signal strengths of the individual rotational lines, it is necessary to know the variation of the linewidth with rotational quantum number J. Unfortunately, the behavior of the H_2 linewidth is complex and its variation with J and with temperature at high densities is not well known.

The variation of hydrogen's linewidth with density can be divided into three regimes. At low density (≤ 0.1 amagat) line broadening is due principly to the Doppler effect. For Raman scattering this line has a Gaussian profile whose width (FWHM) can be written [18]

$$\Delta \nu_D = \frac{2}{c} (2\ell n2 \frac{kT}{m})^{\frac{1}{2}} [4(\nu_o^2 + \nu_o^2 \nu_R) \sin^2(\frac{\theta}{2}) + \nu_R^2]^{\frac{1}{2}} \qquad (17)$$

where ν_o is the exciting frequency, ν_R is the frequency of the Raman resonance, θ is the scattering angle and the other symbols have their usual meaning. For CARS, only scattering in the forward direction is considered ($\theta = 0$) and

$$\Delta \nu_D = \frac{2\nu_R}{c} (2\ell n2 \frac{kT}{m})^{\frac{1}{2}} \qquad (18)$$

In this range, the linewidth is independent of density and varies as the square root of temperature.

When the mean free path for elastic collisions is comparable to the wavelength of the scattered light, but is less than the mean free path for collisional line broadening, the linewidth can become less than that due to Doppler broadening. This phenomena, known as Dicke narrowing [19], is important in reducing the linewidth of molecular hydrogen in the density regime between ~ 0.5 amagat and ~ 25 amagat [20]. Above this density, the lineshape becomes Lorentzian and its width increases linearly with the density (homogeneous or pressure broadening regime). Theoretically this linear variation with density is a consequence of assuming that only binary collisions take place. If the time between collisions is long

compared to the collision time, this criterion is met. Hunt et al. [21] have estimated for H_2 that the time between collisions is approximately three times the collision time for pressures of $\sim$ 100 atmospheres for a hard sphere collision model. This would seem to indicate that linear pressure broadening would be suspect above this value. However, Allin et al. [22] have found linear variation holds between 30 and 600 atmospheres of pressure, presumably at room temperature. Since the collison frequency scales $n\sqrt{T}$ and the pressure as nT, where n is the number density and T the absolute temperature, the collision frequency will decrease with increasing temperature for a given pressure indicating that the line will broaden linearly in this range at elevated temperatures.

The effects of Doppler and pressure broadening can be accounted for simultaneously using an expression for the resonant part of the third order susceptibility developed by Henesian and Byer [23]

$$\chi^{(3)} = \frac{Nn_1c^4\sqrt{\pi}\, i}{\hslash n_2\omega_2^4\Delta\omega_D} \sum_j \Delta_j \left.\frac{\partial\sigma}{\partial\Omega}\right|_j w^\ast(\delta_j + iE_j) \tag{19}$$

where $w(z)$ = complex error function (see Appendix E)

$$\delta_j = [\Omega_j - (\omega_1 - \omega_2)]/\Delta\omega_D$$

$$E_j = \frac{\Gamma_j}{4\pi\Delta\nu_j}$$

$\Delta\omega_D (= 2\pi\Delta\nu_D)$ is defined by Eq. (18), Γ_j is the linewidth (FWHM), and the other quantities are defined as in Eq. (11). Dicke narrowing can be included in a simple way introduced by Galatry [24]. This requires that Γ_j be replaced by

$$\Gamma_J \rightarrow \frac{D_o(T)k^2}{\pi\rho} + A_J(T)\rho \tag{20}$$

where D_o is the diffusion coefficient for the scattering molecule, ρ is the density, A_J is the pressure broadening coefficient, and k is an effective wave vector for Raman scattering i.e. [20]

$$k = [2k_1k_2(1-\cos\theta)^2 + (k_1-k_2)^2]^{\frac{1}{2}} \tag{21}$$

which for the case of CARS ($\theta = 0$) becomes the difference between the wave

15

vectors of the incident and emitted photons. (This means that the line-
width will be a minimum in the forward direction and a maximum in the
backward direction. See, for example Lallemand et al. [25].) It should
be noted that at high pressures ($E_j \gg 1$)

$$w(z) \rightarrow \frac{1}{i\sqrt{\pi}\ z}$$

and Eq. (19) reduces to Eq. (11), the usual expression for the suscepti-
bility.

The diffusion coefficient D is usually written as D_o/ρ and has a
temperature dependence that varies at T^α where α varies between 1.5
(rigid elastic spheres model) and 2 (Maxwellian models) [26]. The more
conservative value of 1.5 is adopted here which, after the temperature
dependence of ρ is removed, implies that $D_o \sim T^{\frac{1}{2}}$. Several spectroscopic
determinations of D_o have been made ([20], [27]) but the measurement of
the diffusion of parahydrogen through normal hydrogen made by Harteck and
Schmidt [28] is the most accurate to date. Their value of 1.396 $\pm$
0.0025 cm^2 sec^{-1} at 785 torr and 20° C is used in these calculations.

There is little data on the temperature dependence of the broadening
coefficient at elevated temperatures. The half width of the Raman lines
is given by nvσ' where v is the average velocity of the colliding pair
and σ' is the real part of the optical cross section [29]. If σ' is
assumed temperature independent, the linewidth would have a $\sqrt{T}$ dependence.
This is consistent with the data of Lallemand and Simova [30] who meas-
ured the temperature dependence of the broadening coefficient of the Q(1)
line of H$_2$ between room temperature and 150° C. (These measurements were
made using a backward wave Raman amplifier and hence their linewidth is
larger than that of the forward wave.) Lallemand and Simova found their
results in disagreement with the theory of Ref. [29]. For simplicity,
the $\sqrt{T}$ dependence of A_j will be used in our estimates of linewidth.

There have been a variety of measurements made of the pressure
broadening coefficients of forward direction Raman scattering of hydrogen
at room temperature for the lowest values of J(0-4). Table 1 compares
these and also lists some theoretical values. Columns 1 and 2 show the
broadening coefficients measured by spontaneous Raman scattering over a

16

TABLE 1

H_2 Pressure Broadening Coefficients (10^{-3} cm^{-1}/amagat)

Line	Allin et al.[a] [22] (1967)	Murray et al.[b] [20] (1972)	Foltz et al.[c] [34] (1966)	Hunt et al.[d] [21] (1970)	Owyoung[e] [27] (1978)	Van Kranendonk[f] [29] (1963) (Theory)	Hunt et al.[g] (1970) (Theory)
Q(0)	2.32 ± 0.04	2.2 ± 0.15		2.78 ± 0.10		2.2	2.59
Q(1)	1.40 ± 0.03	1.5 ± 0.1	1.77	1.83 ± 0.10	1.71 ± 0.02	0.6	.72
Q(2)	2.53 ± 0.03	2.6 ± 0.2		3.05 ± 0.10		2.6	2.87
Q(3)	3.66 ± 0.04	5.5 ± 1		4.60 ± 0.10		3.6	3.87
Q(4)				3.26 ± 0.10		3.0	3.86

a. Spontaneous Raman scattering, 300-600 amagat.

b. Spontaneous Raman scattering, 5-100 amagat.

c. Electric-field-induced measurements, 27-55 amagat.

d. Electric-field-induced measurements, 4.4-35 amagat.

e. High resolution CW stimulated Raman spectroscopy, 0.26-14 amagat.

f. Theory, isotropic scattering due to quadrupolar interaction.

g. Calculation using theory of Van Kranendonk with revised molecular constants.

very wide range of densities (5-600 amagat). These show good agreement except for the Q(3) lines. As noted above, Ref. [22] found the broadening to be linear to 600 amagat. Columns three and four display the linewidths measured by electric field induced dipole transitions over a more restricted density range. Brannon et al. [31] has shown that the theory of Raman line broadening may be applied without modification to electric field induced lines. These values tend to be somewhat higher than those measured by Raman scattering. Column 5 lists a measurement using the high resolution technique of CW stimulated Raman spectroscopy. Columns 6 and 7 give theoretical values obtained using the theory of Van Kranendonk [29]. Hunt et al. [21] has used this theory to recalculate the linewidths utilizing pressure modified effective rotational constants. The disagreement between theory and experiment for the Q(1) line is discussed in Ref. [22].

The pressure broadening coefficients of Allin et al. are adopted for the Q(0) - Q(3) lines in this study. The measured value of Hunt et al. is used for the Q(4) line. Finally it is useful to have a value of A_J for the Q(5) line to obtain temperatures from the ratio of its strengths at higher temperatures. Unfortunately, there is no measured value. Using parameters calculated from Hunt et al., based on Van Kranendonk's theory, a calculated value of 1.08×10^{-3} cm^{-1}/amagat @ 300 K was obtained. This is a particularly risky procedure, however, as the agreement of the modified calculated linewidth with the experimental values becomes poor with higher J numbers [21].

Figure 3 shows a log-log plot of the Q(1) linewidth of H_2 for room temperature and two temperatures that bracket the minimum and maximum temperatures that could be encountered in the SSME preburner. The density range is between 35 amagat (3000 psi, 1700 K) and 150 amagat (6000 psi, 850 K) and the line broadening is well within the pressure broadening regime.

As a final remark, it should be noted that St. Peters [32] has found that when high power lasers are used, the appropriate linewidth for CARS may be larger than the Raman linewidth due to the laser mode structure.
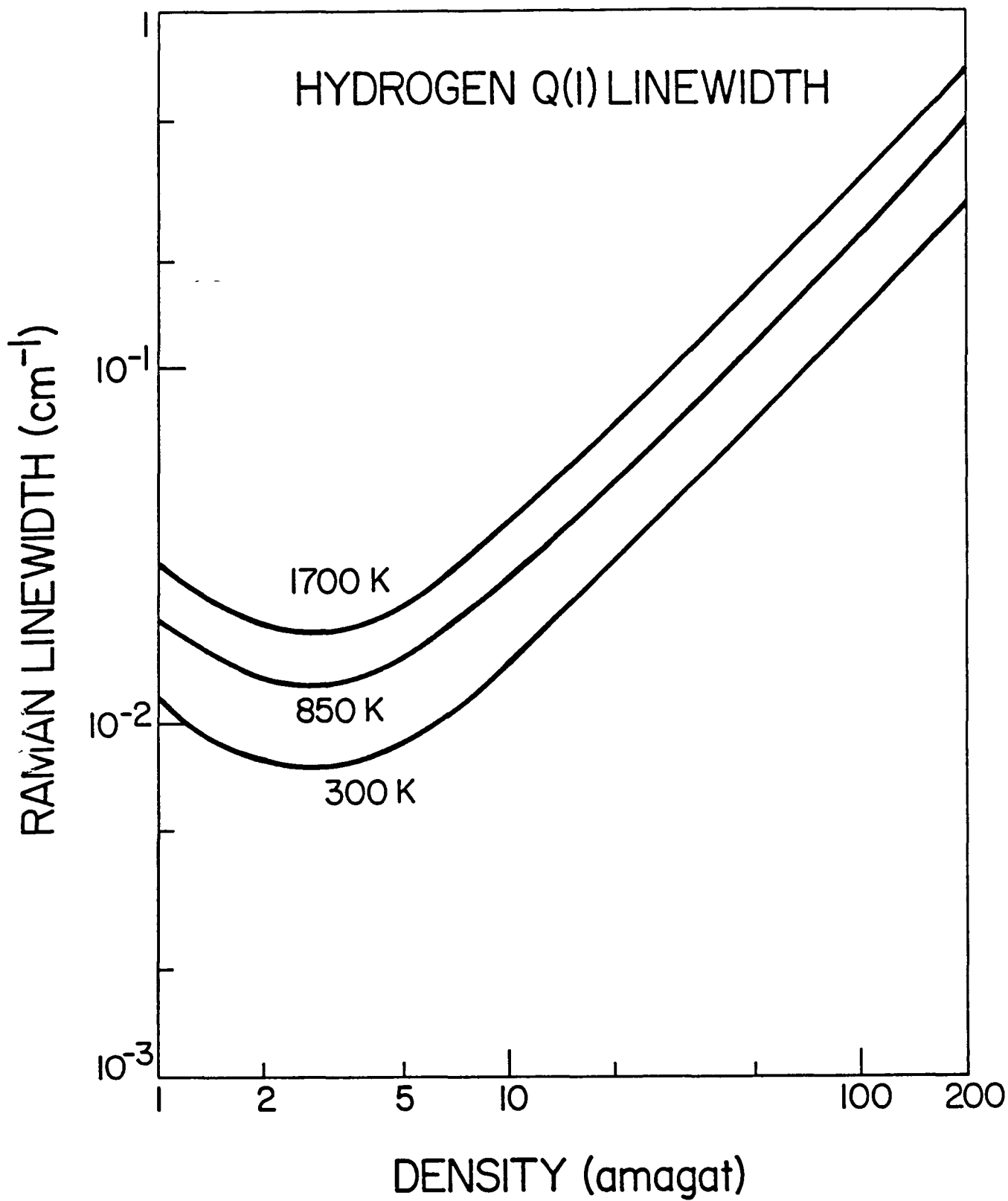
Figure 3. Variation of Hydrogen Q (1) linewidth as a function of
density for several temperatures.

IV. Phasematching

According to Eq. (7) the input laser beams should be phasematched in order to generate appreciable signal levels. The phasematching condition

$$\Delta\vec{k} = 2\vec{k}_1 - \vec{k}_2 - \vec{k}_3 \qquad (22)$$

where $|\vec{k}| = \frac{n\omega}{c}$ is a vector relationship that must be simultaneously satisfied with the energy conservation condition

$$2\omega_1 - \omega_2 - \omega_3 = 0 . \qquad (23)$$

If the medium has little dispersion ($n_1 \simeq n_2 \simeq n_3$) as is the case with gases at moderate pressures, these conditions can be met with all beams parallel to one another (See Figure (4a)). In this geometry the intensity of the CARS signal varies as the sine squared i.e.

$$I \sim \left[\frac{1}{\Delta k} \sin \left(\frac{\Delta k \ell}{2} \right) \right]^2$$

and reaches a maximum in a coherence length L_c where $L_c = \pi/\Delta k$. This length can be calculated by expanding the refractive index of the medium with respect to frequency [35]

$$L_c = \frac{\pi c}{\omega_v^2} \left[2 \frac{\partial n}{\partial \omega} + \omega_1 \frac{\partial^2 n}{\partial \omega^2} \right]^{-1} . \qquad (24)$$

For gases at atmospheric pressure this distance can be tens of centimeters while for liquids it can be fractions of millimeters. Since the CARS intensity is proportional to the square of L_c, the signal levels will be unacceptably small if one works with parallel beams when the medium has appreciable dispersion. Hence, in these media, phasematching is usually achieved by crossing the input beams at a small angle (see Figure 4b). The interaction length in this situation is then limited by beam walkoff.

It is possible to estimate the coherence length of a gas as a function of density by calculating the frequency derivatives of the dispersion equation. The variation of the index of refraction with denstiy can be represented with a high degree of accuracy using the Lorenz-Lorentz relation [36,37]

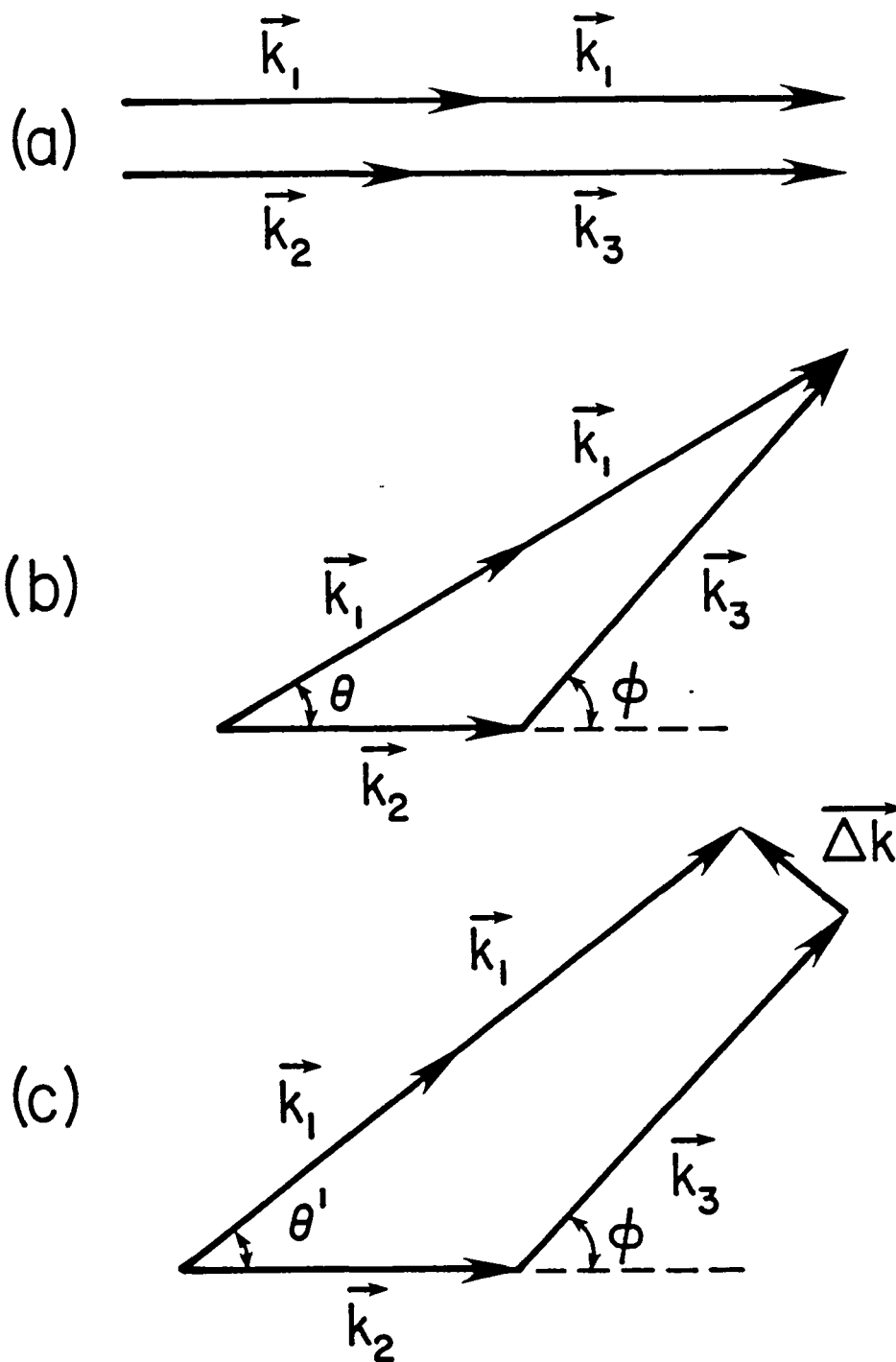$$\frac{n^2-1}{n^2+2} = R(\lambda)\rho \qquad (25)$$

Figure 4. Wavevector diagrams illustrating different phasematching configurations. (a) Collinear phasematching. (b) Crossed beam phasematching necessary for media with appreciable dispersion. (c) Relationship between wavevectors and Δk for phase mismatched beams.

where n is the index of refraction and $R(\lambda)$ is the specific refraction that depends on the polarizability of the species. The dispersion equation for H_2 at a density of one amagat is [38]

$$n_0^2 - 1 = a + \frac{b}{\lambda^2 - \lambda_0^2}$$

(26)

where the empirical constants, a, b and λ_0 have been measured by Koch [39]. Solving Eq. (25)

$$n^2 - 1 = \frac{3R\rho}{1 - R\rho}.$$

Putting $\rho = 1$ in this equation and equating it to the right hand side of Eq. (26) one finds $R = A/(A+3)$ and

$$n^2 - 1 = \frac{3\rho A(\lambda)}{3 - (\rho - 1) A(\lambda)}$$

(27)

where

$$A(\lambda) \equiv (a + \frac{b}{\lambda^2 - \lambda_0^2}),$$

Equation (27) is the density dependent dispersion equation. This equation can be simplified by noting that even at high densities $(\rho - 1)A(\lambda) << 3$ (at 200 amagat $\rho A = 0.056$ at $\lambda = 532$ nm) and

$$n^2 - 1 \simeq \rho A(\lambda)$$

(28)

Table 2 delineates the calculation of L_c for the H_2 Q(1) line assuming a pump laser at 532 nm. This analysis indicates that the dispersion of H_2 scales linearly with density and not with the square root of pressure as stated by Wilke and Schmidt [40] and except for extremely high densities the coherence length varies inversely with density. Figure 5 shows the coherence length as a function of density. At $\rho = 100$ amagat, $L_c \simeq 2$ mm.

TABLE 2

$$L_c = \frac{\pi c}{\omega_V^2 [2n' + \omega_1 n'']}$$

where

$$n = [A\rho + 1]^{\frac{1}{2}}$$

$$n' \equiv \frac{dn}{d\omega} = \frac{A'}{2n}\rho$$

$$n'' = \frac{1}{n}\left[\frac{A''}{2}\rho - \left(\frac{A'\rho}{2n}\right)^2\right]$$

$$A(\omega) = a + b[d/\omega^2 - \lambda_0^2]^{-1}$$

$$A' = \frac{2bd}{\omega^3[\quad]^2}$$

$$A'' = \frac{2bd}{\omega^4}\left\{\frac{4d}{\omega^2[\quad]^3} - \frac{3}{[\quad]^2}\right\}$$

$$[\quad] \equiv d\omega^{-2} - \lambda_0^2$$

$$d = (2\pi c)^2$$

For the Q(1) line of hydrogen at $\lambda = 0.532$ μm

$$a = 2.716\ (10^{-4})$$
$$b = 2.112\ (10^{-6})$$
$$\lambda_0^2 = 7.760\ (10^{-3})\ \text{for } \lambda \text{ in μm [Ref. 39]}$$

and

$$L_c \simeq \frac{1.54}{6.92(10^{-2})\rho + 1.75(10^{-7})\rho^2}\ \ (\text{cm})$$

$$\simeq \frac{22.2}{\rho}\ \text{cm}\qquad \rho \text{ in amagat}$$
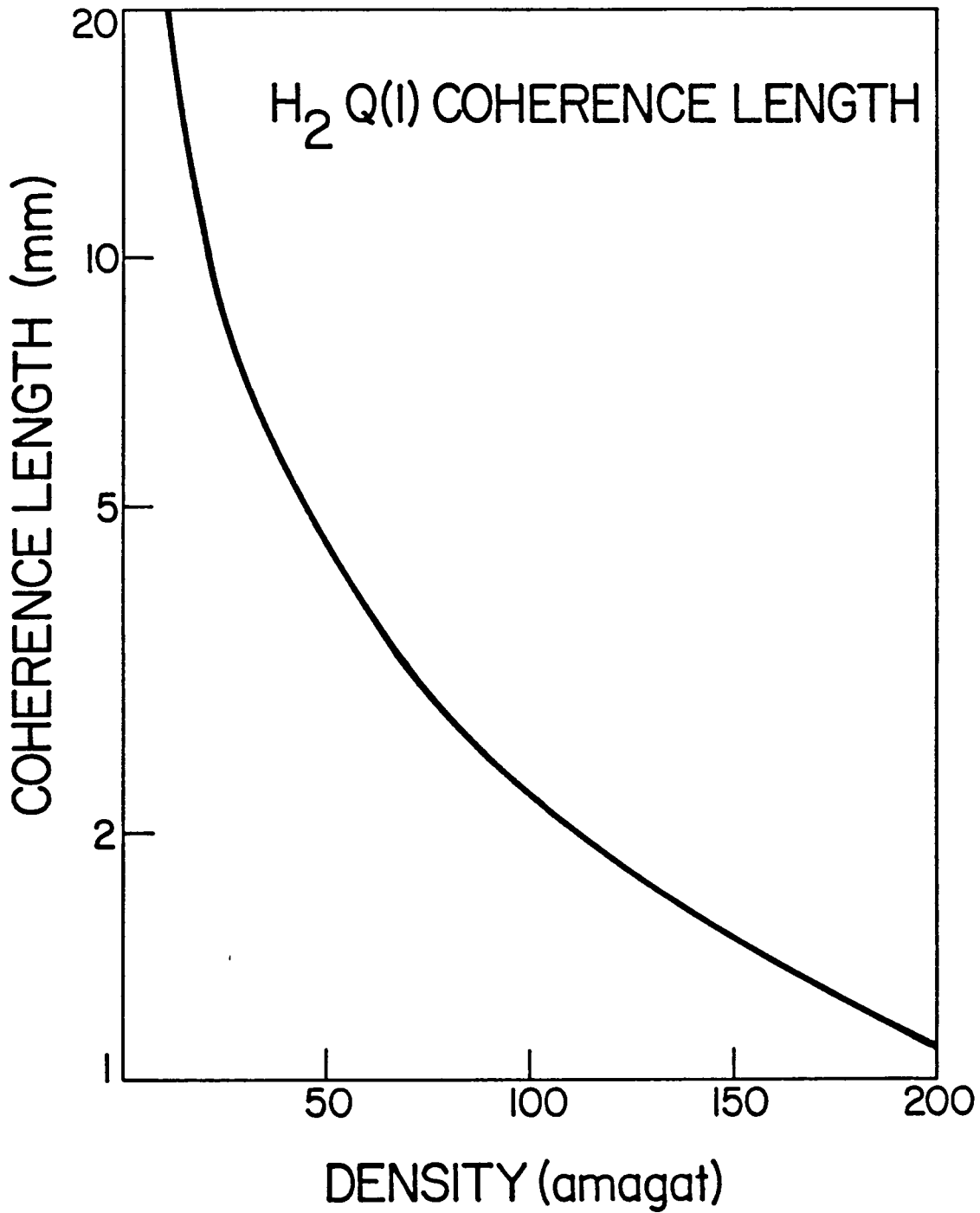
Figure 5. Hydrogen Q(1) coherence length for beams in collinear
phasematching geometry as a function of density.

To predict the behavior of the CARS signal in the medium, this value of coherence length should be compared to the distance, b, near the beam waist over which a focused beam remains essentially parallel. If a beam of divergence half angle $\delta_{1/2}$ is focused by a lens of focal length f, this distance is approximately given by $2\pi f^2 \delta_{1/2}^2/\lambda$. Even for a conservative divergence of $\delta_{1/2} = 0.1$ mrad, b $\simeq$ 12 cm when a beam passes through a 1 m focal length lens. Hence, at a density of 100 amagat, the CARS signal would have a squared sinusoidal variation with a period of $\sim$ 4 mm in this region. (It is interesting to note that when b<<L_c, collinearly phase-matched beams generate only 75% of the CARS signal in a length of $\sim$ 7.5b [35].)

It is clear, at the high densities expected in the preburner, the pump and Stokes laser beams must be crossed at a small angle. Using the linear momentum conservation equations implied by Figure 4b and the energy conservation relationship Eq. (23), an expression for crossing angle θ can be found:

$$\cos\theta = \frac{4\omega_1\omega_2 n_3^2 - 4\omega_1^2(n_3^2 - n_1^2) - \omega_2^2(n_3^2 - n_2^2)}{4\omega_1\omega_2 n_1 n_2} . \tag{29}$$

This crossing angle was calculated for the hydrogen Q(1) line and a pump laser wavelength of 532 nm. The result, shown as a function of density, is given in Figure 6. At a density of 100 amagat the phasematching angle is $\sim$ 0.78°.

It is interesting to calculate the sensitivity of the CARS intensity to a small phase mismatch due to a non-optimum matching angle θ. From Eq. (7) the intensity varies as sinc(x)(=sin(x)/x), where $x = \frac{\Delta k \ell}{2}$, Δk is the magnitude of the wave vector mismatch (see Figure 4c), and ℓ is the interaction length. Holding ϕ constant at the phasematched value, the CARS intensity was calculated as a function of θ for the Q(1), Q(3), and Q(5) lines of H_2. The results are shown in Figure 7 for $\rho = 1$ and $\rho = 100$ amagat density and $\ell = 1$ cm. The FWHM's of the sinc functions are $\sim$ 0.01 mrad ($\sim$ 7 x 10^{-4} degrees) and the intensities for the Q lines overlap for the low density case. However, at 100 amagat the increased dispersion separates the lines in θ-space. This would indicate that separate angles are required for the individual lines. In practice, however, the beam divergence of the laser beam are greater than the
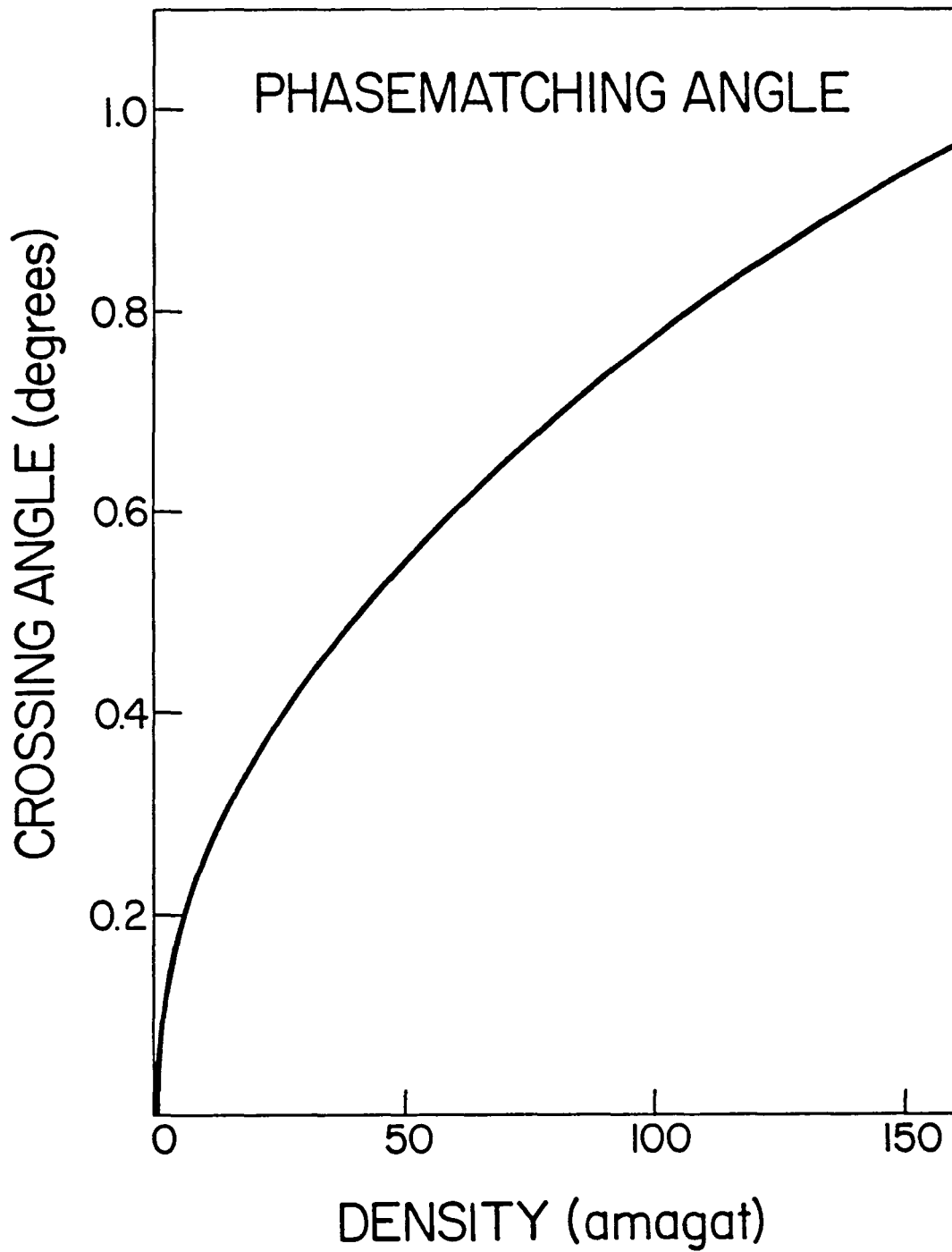
PHASEMATCHING ANGLE

Figure 6. Crossing angle required for Q(1) line phasematched beams as a function of hydrogen density.
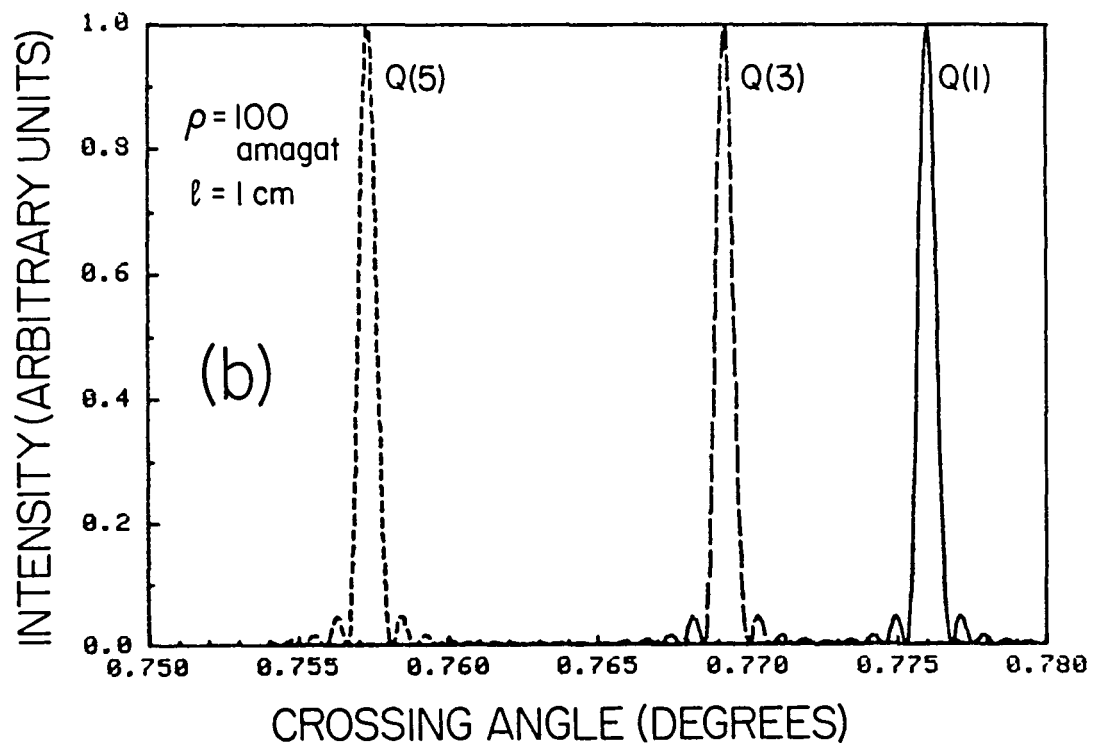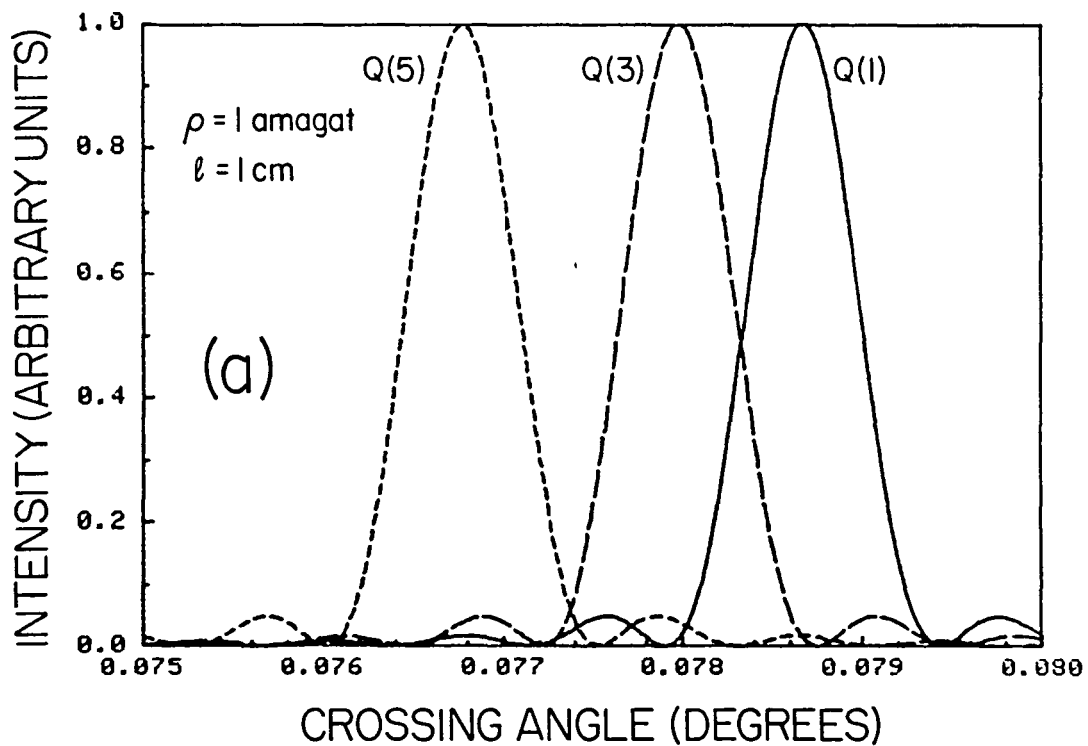
Figure 7. CARS normalized intensity variation for the first three
strong Q branch lines of hydrogen as a function of crossing angle.
(a) 1 amagat density. (b) 100 amagat density.

27

angular separation between the Q(1) and Q(5) lines and signal can be produced for these lines simultaneously - albeit at considerably lower intensities than those calculated for the ideal case of exact phasematching.

The details of the intensity of various lines will depend on the intensity distribution as a function of angle of the laser. By its nature this variation cannot be folded into the signal and error calculations of Section VI. Indeed, ratios of the intensities of the Q lines may depend on the exact angle of crossing and could differ for identical conditions of temperature and pressure. This is an area where experimental investigation is warranted before attempting a measurement.

V. _Laser Intensity Limitations_

There are several effects that will place upper limits on the intensity of the pump beam in the medium. These in turn will limit the CARS signal strength and hence, the accuracy with which temperature measurements can be made. Although these effects generally are not important when performing diagnostics in flames at atmospheric pressure they can become important considerations at higher pressure.

Two of these effects were first discussed by Reginer et al. [41]. The first is most important when using a collinear phasematching geometry and results in an augmentation of the Stokes intensity through the process of stimulated Raman gain. A high intensity laser beam with angular frequency ω_1 travelling through a Raman active medium can induce coherent radiation to propagate parallel to it at frequency ω_2 and intensity I_2. Assuming negligible depletion of the pump beam intensity I_1

$$I_2(\ell) = I_2(0) \, e^{g\ell I_1} \qquad [30]$$

where ℓ is the length that I_1 interacts with the medium, $I_2(0)$ is the Stokes field originally present and g is the Raman gain of the medium given by [see for example, Ref. 42]

$$g = \frac{(4\pi c)^2 N_o \rho \Delta_j}{n^2_s \omega^2_s \hbar \omega_1 \Gamma_j} \left(\frac{d\sigma}{d\Omega}\right)_j \qquad [31]$$

where N_o is the number density at 1 amagat ($2.69 \times 10^{-19} cm^{-3}$) and all other symbols in this expression have been previously defined. Where the linewidth decreases or remains constant as the density increases, the gain increases (Dicke narrowing regime). In the pressure broadening regime, the gain is independent of density. For the Q(1) line at 1200 K and 100 amagat, $g \sim 6 \times 10^{-10}$ cm/watt. If I_1^{max}, the highest allowable pump beam intensity is considered to be that which will induce a 10% growth in the Stokes field ($I_s/I_s(0) = 1.1$) then $I_1^{max} \sim 1.7 \times 10^8$ watts cm^{-2}/ℓ. For an interaction length approximately equal to the Rayleigh length (> 10 cm), this maximum value is quite low and presents a severe constraint that must be avoided if reasonable signal levels are to be attained. This points out another difficulty with performing the measurement using the more geometrically simple collinear phasematching. If the pump and Stokes beams

are crossed, this hazard can be avoided.

It should be noted that the pump beam alone can generate a co-propagating Stokes wave with an appreciable intensity. This could yield spurious temperature measurements even when the pump and Stokes beams are crossed if the CARS signal produced parallel to the pump beam were not separated from the crossed beam CARS signal. In this case, Eqs. (30) and (31) are again used to calculate the power of the stimulated Stokes wave, but in the absence of an external Stokes beam the initial Stokes power is taken as the initial spontaneous Raman noise level, i.e. $P_s(0) \simeq \hbar\omega_2 \Gamma_j$ [42]. For the Q(1) line at 100 amagat density, this is $\sim 2 \times 10^{-9}$ watt. Therefore, for a pump intensity of 10^9 watts/cm^2, a distance of ~ 46 cm would be required to generate the same spectral power density as that available from the Stokes beam (assuming a 1 megawatt pulse and a 100 cm^{-1} spectral width). Since the preburner diameter is ~ 25 cm, the stimulated Stokes power is less than 10^{-5} of this value and no special precautions need be considered.

In reality, both of these calculations will overestimate the power generated by stimulated Raman scattering since it has been found experimentally that saturation of the Stokes intensity in H_2 begins near a density of 10 amagat (at room temperature) and even suffers decreases in intensity [43,44]. This diminution is attributed to a decrease in the gain at higher densities and the fact that the increased optical dispersion at these densities makes the four wave mixing process more difficult.

A second phenomena that can cause measurement inaccuracies if I_1 and I_2 are too intense is a population perturbation between the lower and upper rotational levels. Stimulated Raman coupling between these two levels can affect Δ_j (see Eq. (11)) such that

$$\Delta_j(t) = \Delta_j(0) \exp(-t/\tau_\Delta)$$

where, on resonance, the time constant for this perturbation is given by [41]

$$\tau_\Delta^{-1} = 2g_j \left(\frac{4\pi c}{\hbar\omega_2^2}\right)^2 \left(\frac{d\sigma}{d\Omega}\right)_j \frac{I_1 I_2}{\Gamma_j}$$

where $g_j = 2v_j + 1$ and I_2 is the Stokes intensity within the Raman linewidth. In the density region where the Raman linewidth is homogeneously

30

(pressure) broadened, this time constant varies linearly with density. However for broadband CARS $I_2 = I_2{}^{tot} \left(\frac{\Gamma_j}{\Delta\omega_2}\right)$ where $\Delta\omega_2$ is the spectral width of the Stokes beam the time constant is independent of density. For the Q(1) of H_2 with $\Delta\omega_2 = 2\pi c(100 \text{ cm}^{-1})$, $\tau_\Delta{}^{-1} \simeq (2 \times 10^{-28}) I_1 I_2{}^{tot}$. If $I_1{}^{max}$, the maximum allowable intensity, is defined as that which causes a 10% population perturbation, it is assumed $I_2 = 0.5 I_1$, and the time of the perturbation is taken to be the laser pulse width (10^{-8} sec) then $I_1{}^{max} \simeq 10^{10}$ watt cm^{-2}. This value should not be exceeded.

The third effect that may limit the CARS signal strength is the maximum pump beam power than can be focused into the H_2 without causing an ionization breakdown. The breakdown threshold intensity for most gases exhibits a minimum in the pressure range of 100 - 1000 atm [45]. The variation with pressure of the threshold minima is slower for molecular gases than for atomic gases [46].

Measurements of the breakdown threshold intensity have been taken for various gases (He, N_2, Ar) over a large enough pressure range to determine the minima [47]. However, data for H_2, in the range $0.5 \leq P \leq 100$ atm [48], do not cover sufficiently high pressures to show the breakdown minimum nor to cover the pressure region of interest to this study. The pressure at which the breakdown minimum occurs can be calculated from the classical impact ionization description of breakdown [45]. An approximation to the calculated minimum should give a reasonable approximation for pressures near 400 atmospheres. The electron energy change is a maximum when the momentum-transfer collision frequency ν_m is equal to the incident field frequency. In terms of the reduced pressure (torr), collision probability P_c, and mean energy (eV), the collision frequency is expressed as

$$\nu_m = 5.93(10^7) \, P_c \, \sqrt{\epsilon} \, p_o, \quad (p_o \text{ in torr, } \epsilon \text{ in eV}).$$

From tabulations [49] of P_c vs $\sqrt{\epsilon}$, the mean value of $P_c\sqrt{\epsilon}$ for H_2 can be estimated to be approximately 80. It has been noted [45] that for hydrogen the collision frequency is very weakly dependent on electron energy, so

$$\nu_m \simeq 5.9 \, (10^9) \, p_o \quad (p_o \text{ in Torr}).$$

With these two relations a bound can be placed on the pressure of the minimum for the data presented in Ref. 48. Figure 8a shows the ruby laser H_2 breakdown data (converted to power density using a beam focal diameter of 1.2×10^{-3} cm) as a function of pressure for a wavelength of 594.3 nm ($\omega = 2.71 \times 10^{15}$ sec^{-1}). The curve is an approximate fit extrapolated to the calculated minimum: $600 \le p_o \le 750$ atmospheres.

For this data to be applicable to this study it must be scaled to the expected experimental conditions. The effect of the differences in temperature, beam focal volume, and beam frequency are the most significant. Since the minimum breakdown threshold scales with density (reduced pressure), the data from Fig. 8a should be shown as a function of density (assuming the data was taken at or near room temperature). The dependence of the breakdown field strength on beam focal volume has been shown [45] to vary as $E \propto \Lambda^{-3/4}$ (or $S \propto \Lambda^{-3/2}$ for power density), where Λ is the characteristic diffusion length of the focal volume. For a cylindrical focal volume with diameter d, length L,

$$\Lambda^{-2} = \left\{ \left(\frac{2.4}{d/2} \right)^2 + \left(\frac{\pi}{L} \right)^2 \right\}^{-1}$$

For most beam geometries d<<L so $\Lambda \propto d/4.8$. As the focal spot size increases, the breakdown threshold decreases. For the data of Ref. 48:

$f = 2$ cm, $d \simeq 1.2 \, (10^{-3})$ cm; so $\Lambda \simeq 2.3 \, (10^{-4})$ cm. Possible values for this study include:

$f = 100$ cm, $.01 \le d \le .05$ cm; thus $2.08(10^{-3}) \le \Lambda \le 1.04(10^{-2})$ cm.

The power density focal spot scaling factor, $(\Lambda/\Lambda_o)^{-3/2}$, should be in the range $3.43(10^{-3}) \le (\frac{\Lambda}{\Lambda_o})^{-3/2} \le 3.73(10^{-2})$. The beam frequency dependence of the threshold power density should be $S \propto \omega^2$, since the rate of increase of the electron energy is inversely proportional to the square of the incident field frequency. This naive view is consistent with the behavior of threshold in the frequency range of a ruby laser (used in Ref. 48) and a frequency-doubled Nd:YAG laser (present study) [45] i.e. $2.71(10^{15}) \le \omega \le 3.54(10^{15})$ sec^{-1}. The frequency scaling factor should increase the breakdown threshold by the factor $(\omega/\omega_o)^2 \simeq 1.7$.

Figure 8b shows the possible range of the power density breakdown threshold for the experimental conditions of this study as a function of
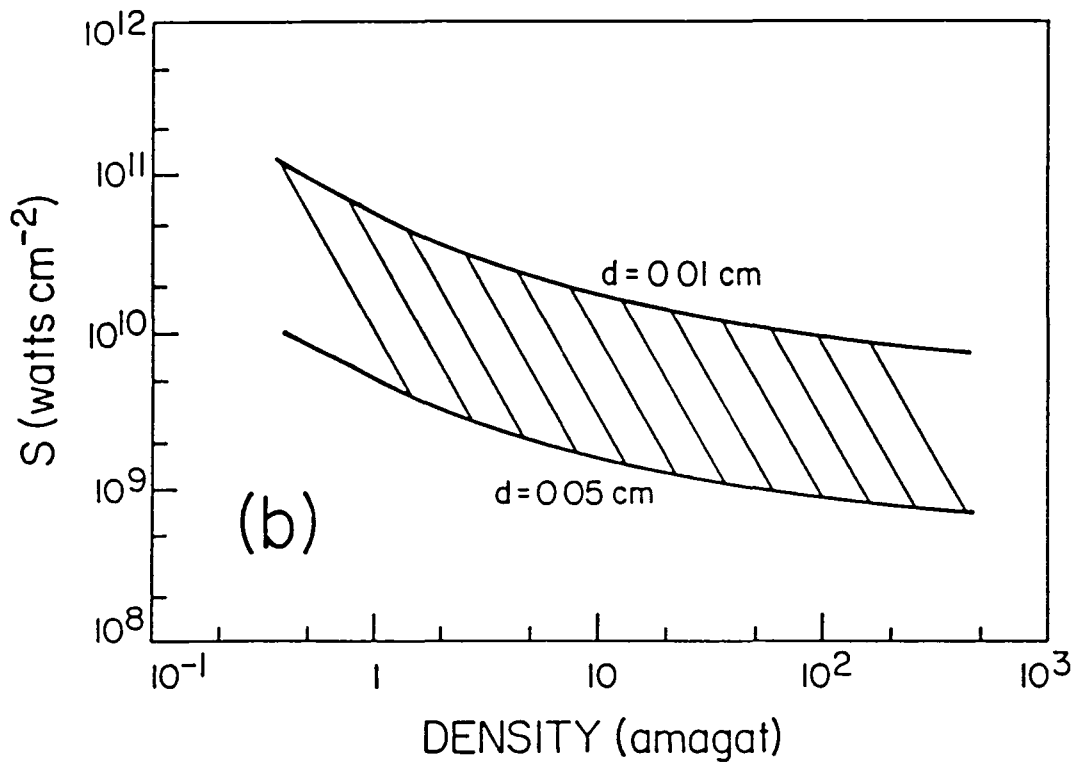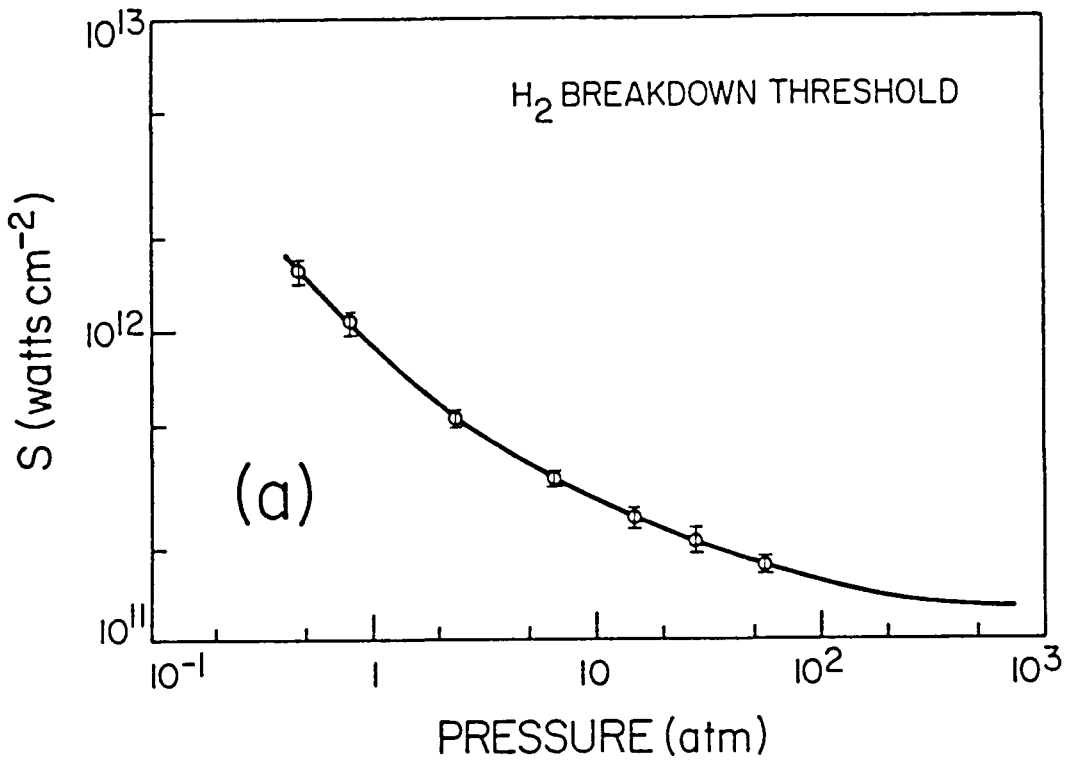
Figure 8. H_2 breakdown threshold power density as a function of
pressure and density (a) Data from reference [48]. Curve is
approximate fit extrapolated to predicted minimum at ∿ 675
atmospheres. (b) Expected range of breakdown power density scaled to
parameters of interest in this study for a range of focal spot diam-
eters. Calculated from data given in (a).

gas density. For the expected number density of 100 amagat, the limiting power density will be $8.5(10^8) \leq S \leq 9.5(10^9)$ watt/cm^2, for the range of focal spot sizes $.05 \geq d \geq .01$ cm. Note that similar predictions of the minimum threshold for single mode lasers have been within a factor of 2 in the power density and pressure [45,47]. If the laser is significantly multi-mode, the threshold will be lower than that calculated [50].

VI. *Signal Strength and Expected Error*

An estimate of the expected signal strength can be made using Eq. (8) which assumes the condition of exact phasematching ($\vec{\Delta k}=0$),

$$ P_3 = \left(\frac{4\pi^2\omega_3}{c^2}\right)^2 |\chi_{CARS}|^2 \; I_1^2 \; P_2 \; \ell^2 $$

where ℓ is the interaction length, it has been noted that $n_1 \simeq n_2 \simeq n_3 \simeq 1$ and powers have been substituted for intensities I_2 and I_3 by assuming that the CARS signal is generated with the same cross-sectional area as the Stokes beam. The CARS susceptibility is given by Eq. (11) which on resonance is

$$ \chi_{CARS} = \frac{2\Delta_j Nc^4}{\hbar\omega_2^4} \left(\frac{d\sigma}{d\Omega}\right)_j \frac{1}{\Gamma_j} $$

where the full width Γ_j has replaced the half width γ_j and it is taken that $\chi_{NR} \simeq 0$. Combining these expressions one may calculate the number of photons generated per laser pulse $\tilde{N}_j$ for a given resonance j in terms of the energy of the Stokes beam E_2,

$$ \tilde{N}_j(T,\rho) = \left[\left(\frac{8\pi^2 c^2}{\hbar}\right) N_o\rho \left(\frac{\omega_3}{\omega_2^4}\right) \frac{\Delta_j}{\Gamma_j} \left(\frac{d\sigma}{d\Omega}\right)_j I_1\ell\right]^2 \frac{E_2}{\hbar\omega_3} \tag{32} $$

where N_o is the number density of 1 amagat (2.69×10^{19} cm^{-3}), ρ is the density in amagat, Δ_j is the fractional population difference between upper and lower states (see Appendix C), and $\left(\frac{d\sigma}{d\Omega}\right)_j$ is the Raman cross section (see Appendix B). E_2 is the Stokes energy within the Raman linewidth which for a broadband beam of spectral width $\Delta\omega_2$ is

$$ E_2 = E_2^{total} \left(\frac{\Gamma_j}{\Delta\omega_2}\right) $$

Hence for broadband CARS, the signal strength is inversely proportional to Γ_j and in the pressure broadened region increases linearly with density. The signal strength varies quadratically with pump laser intensity, an attractive parameter to use to increase measurement accuracy. However, the upper limits to the intensity set by population perturbations, stimulated Raman gain, and laser induced gas breakdown as described in Section V must be observed.

35

For the purposes of this calculation, a pump beam intensity of 10^9 watts cm^{-2} and a Stokes beam energy of 10 mJ in a spectral width of 100 cm^{-1} will be considered. Modern Nd:YAG lasers are capable of producing nearly 100 times this intensity at a wavelength of 532 nm when focused by a 1 m lens. An interaction length of 1 cm is used in accordance with the discussion in Section VII. Figure 9 shows the expected CARS signal strength (photons per laser pulse) calculated from Eq. (32) as a function of temperature for the case of a constant number density of 100 amagat for the first six Q lines of hydrogen. As is evident from these curves, the expected signals are quite large. The odd valued Q lines have greater signal strengths due to the statistical weight factor and hence the analysis will concentrate on these lines.

As discussed in Section VII, there are several methods that can be used to recover and analyse the CARS signal. Two are considered here. The first is to ratio the signals obtained from the individual lines and the second is to ratio the signals obtained from two interference filters. Figure 10a shows calculated ratios of the odd (strong) lines using Eq. (32) as a function of temperature for a constant density of 100 amagat. Figure 10b shows the expected ratios if the CAR spectra is convoluted by 1.0 nm (FWHM) interference filters with triangular spectral profiles (characteristic of two period filters). The filters are centered at 438, 437, and 436 nm respectively (see Figure 19). Note that these two figures have different ordinates.

The Q_5/Q_1 ratio has the greatest slope of the Q ratios and varies more than an order of magnitude for the range of temperatures of interest (800-1600 K). The F_2/F_3 ratio has the greatest ratio among the F ratios, but the slope is considerably less than that of the Q_5/Q_1, its value varying less than a factor of 4 in this same temperature interval.

Error Analysis

It is useful to consider the accuracy with which the temperature can be extracted from these ratios. This can be done in terms of simple error propagation theory [51]. The variance σ_x^2 of a quantity x in terms of the variances of variables u and v is approximately

$$\sigma_x^2 \simeq \sigma_u^2 \left(\frac{\partial x}{\partial u}\right)^2 + \sigma_v^2 \left(\frac{\partial x}{\partial v}\right)^2 + 2\sigma_{uv}^2 \left(\frac{\partial x}{\partial u}\right)\left(\frac{\partial x}{\partial v}\right)$$
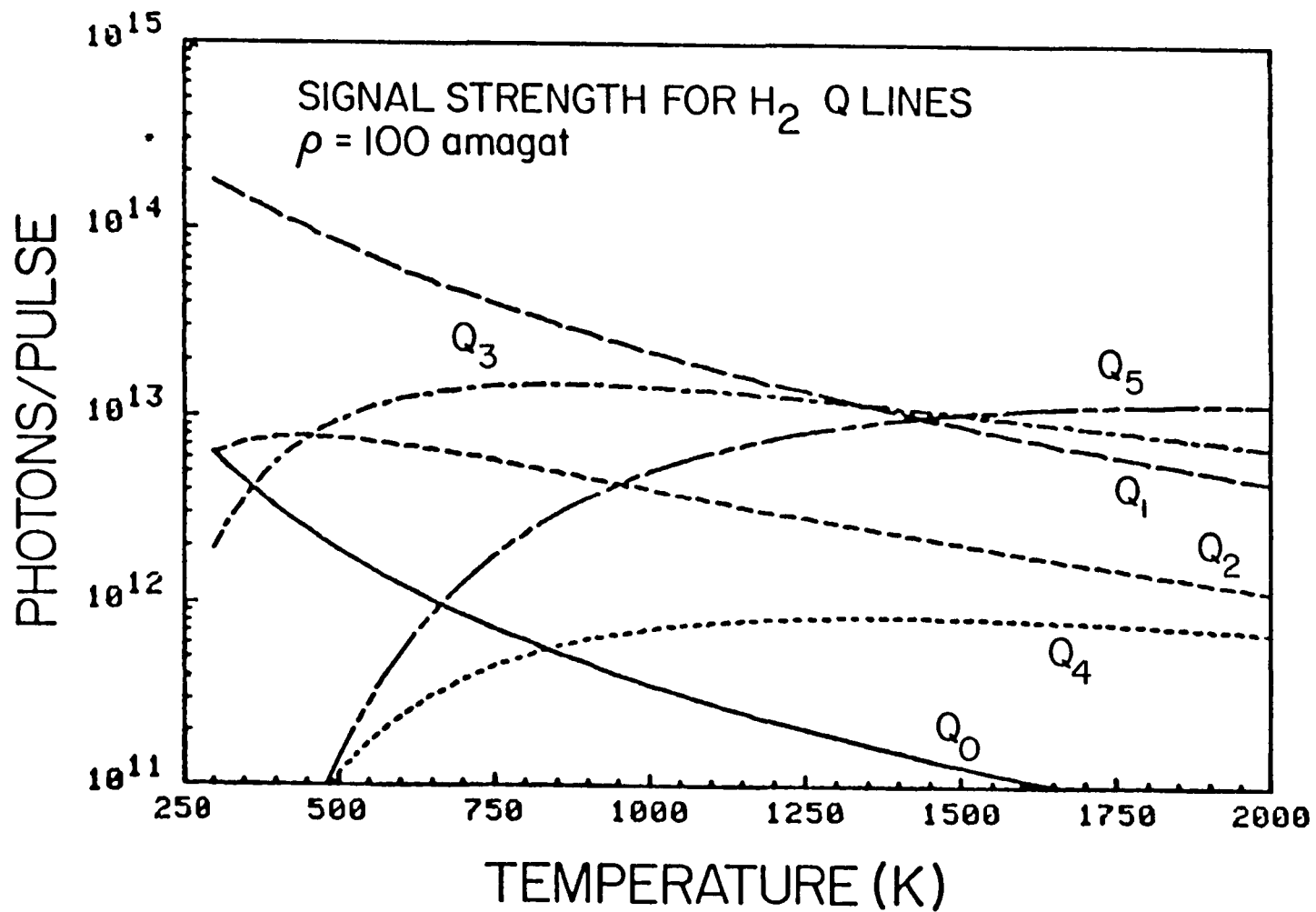
Figure 9. Calculated CARS signal strength for Q branch lines of H_2 at 100 amagat density.
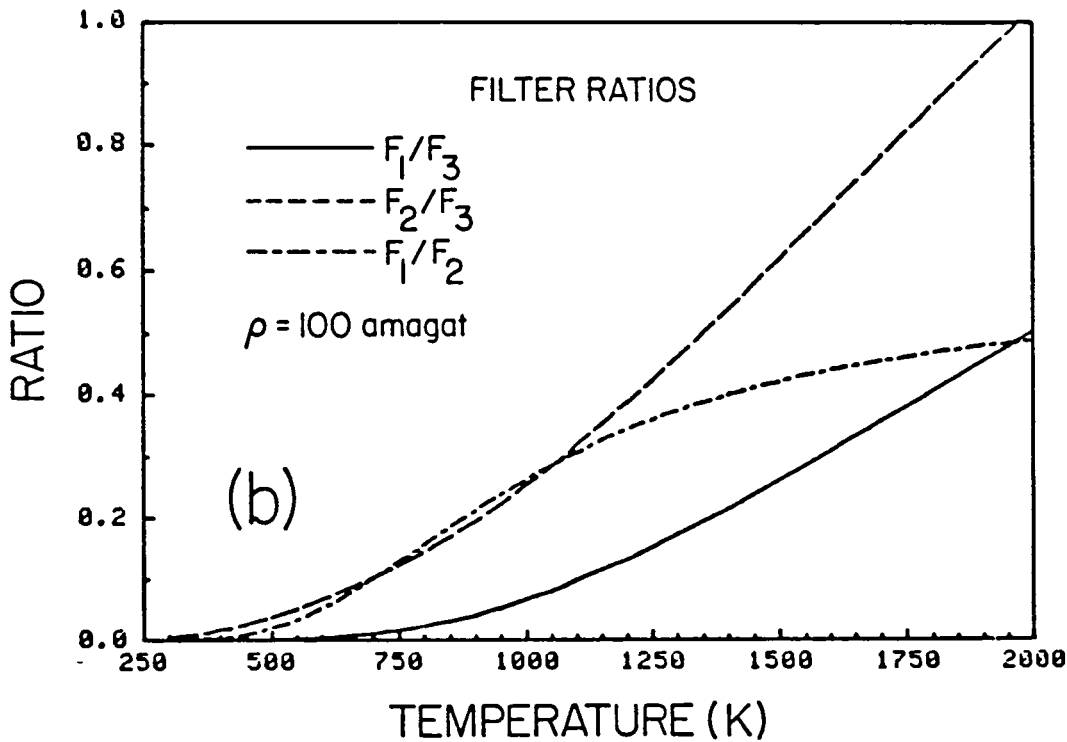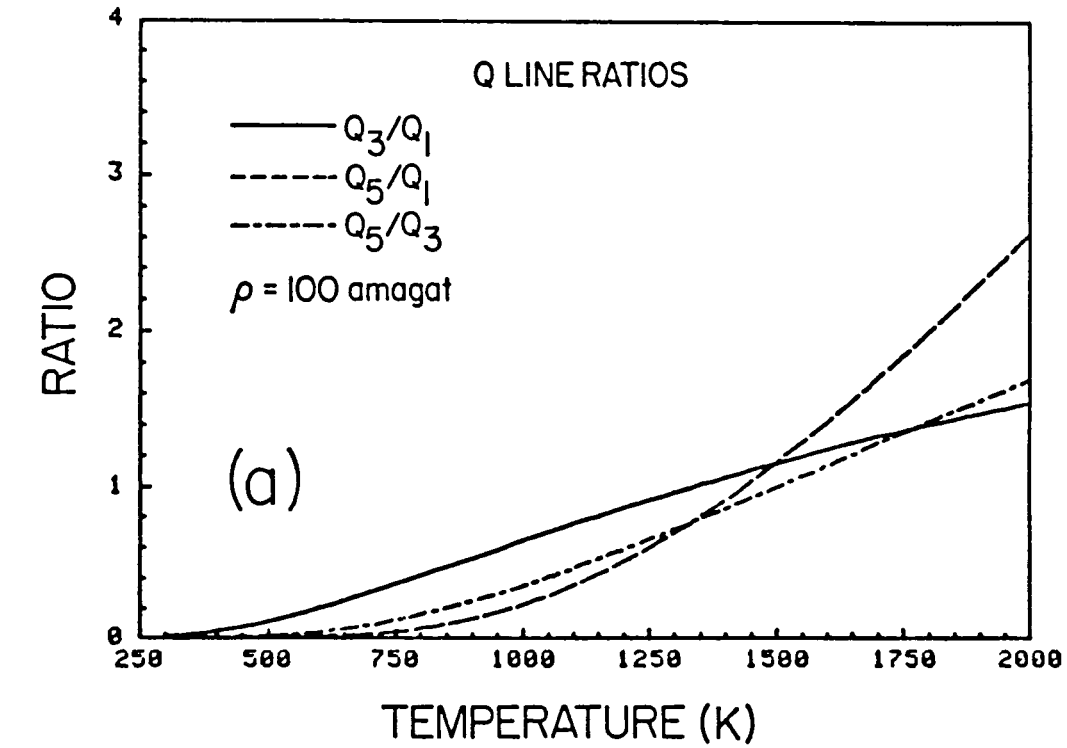
Figure 10. (a) Calculated CARS Q line signal ratios for 100 amagat density. (b) Calculated ratios from CARS H_2 Q line signals taken through the three interference filters displayed in Figure 19.

where the covariance σ^2_{uv} is zero if the fluxuations in u and v are un-correlated. The error in temperature due to error in the ratio of counts R is simply

$$\sigma^2_T = \sigma^2_R \left(\frac{\partial T}{\partial R}\right)^2$$

where $R = N_1/N_2$. The uncertainty in the ratio will consist of the experimental uncertainty with which the ratio can be measured σ^2_{MR} (due to gated integration electronics, ratiometers, A/D etc.) and that due to uncertainty in the number of counts σ_{NR} so

$$\sigma^2_R = \sigma^2_{MR} + \sigma^2_{NR}$$

and

$$\sigma^2_{NR} = \sigma^2_{N_1} \left(\frac{\partial R}{\partial N_1}\right)^2 + \sigma^2_{N_2} \left(\frac{\partial R}{\partial N_2}\right)^2$$

The uncertainty in the number of counts can be ascribed to purely statistical causes σ_{stat} and to the dependence of this number on the linewidth, which itself has appreciable uncertainty. If the measurements are taken using the interference filter configuration, the counts will depend on contributions from several lines so

$$\sigma^2_N = \sigma^2_{stat} + \sum_i \sigma^2_{\Gamma_i} \left(\frac{\partial N}{\partial \Gamma_i}\right)^2$$

Then, noting $\left|\frac{\partial R}{\partial N}\right| = \frac{R}{N}$ and letting $\sigma_{stat} = \sqrt{N}$ the variance in temperature due to these uncertainties can be written

$$\sigma^2_T = \left\{ \sigma^2_{MR} + \left[N_1 + \Sigma\sigma^2_{\Gamma_i} \left(\frac{\partial N_1}{\partial \Gamma_i}\right)^2 \right] \left(\frac{R}{N_1}\right)^2 + \left[N_2 + \Sigma\sigma^2_{\Gamma_i} \left(\frac{\partial N_2}{\partial \Gamma_i}\right)^2 \right] \left(\frac{R}{N_2}\right)^2 \right\} \left(\frac{\partial T}{\partial R}\right)^2 \quad (33)$$

Figures 11 through 16 show the calculated error σ_T for the same conditions used for the signal strength plot (Figure 9). Figures 11 and 12 consider uncertainty in temperature due to statistics, ratio measurement and linewidth uncertainty (two cases) individually. These calculations assume that only 5% of the photons are recovered and impinge on a photomultiplier with a quantum efficiency of 0.2. For these conditions, Figure 11a shows that the projected error in temperature due to statistical uncertainty alone is quite small. Figure 11b displays the uncertainty in T expected
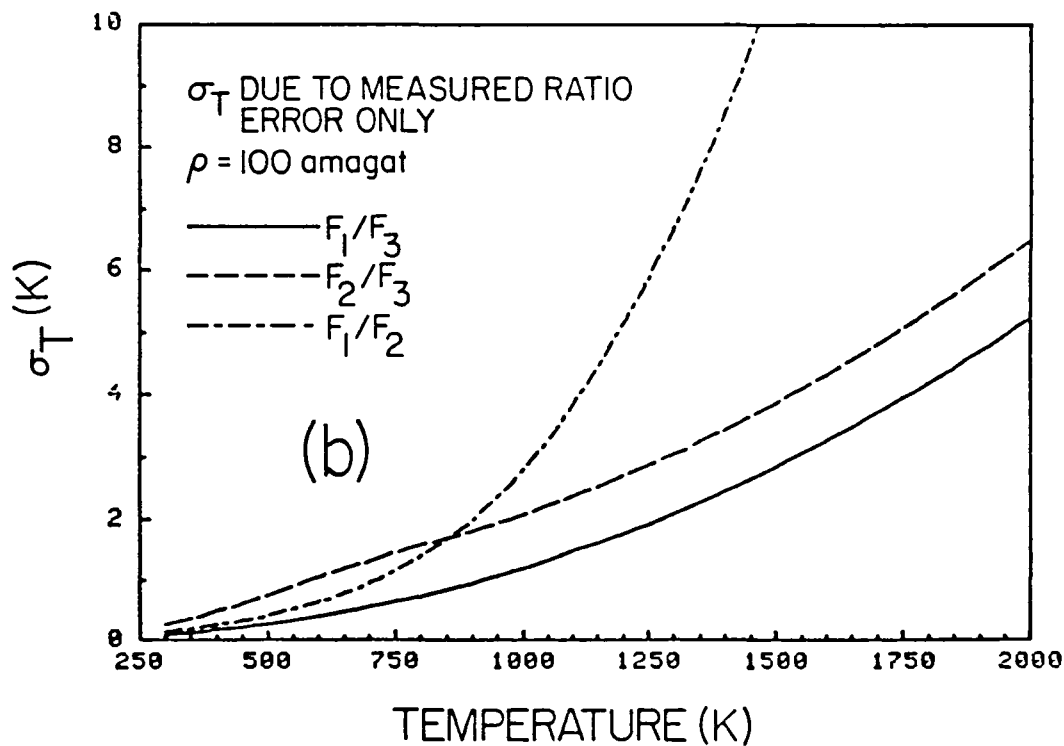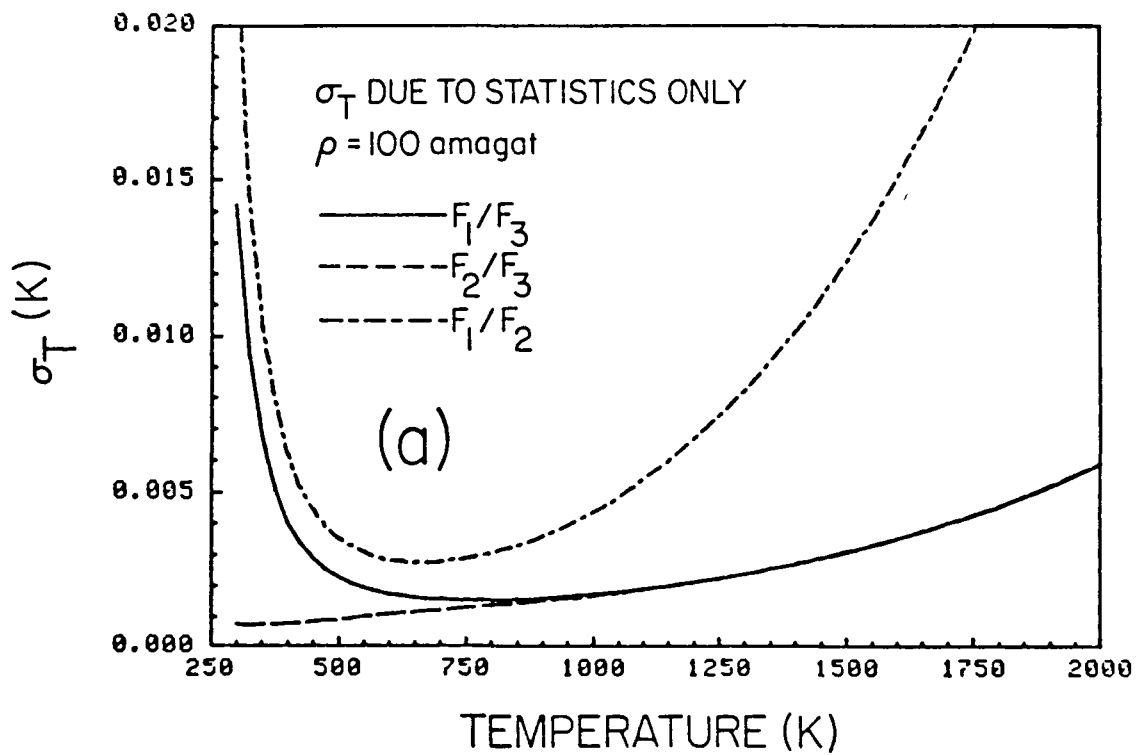
39
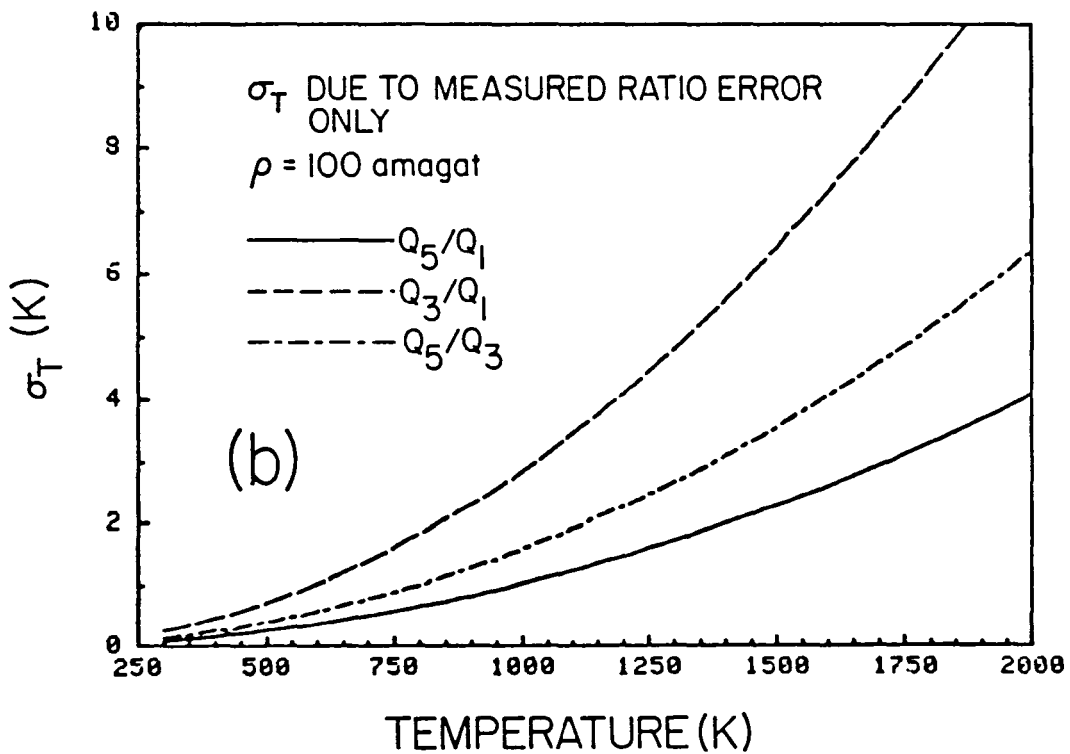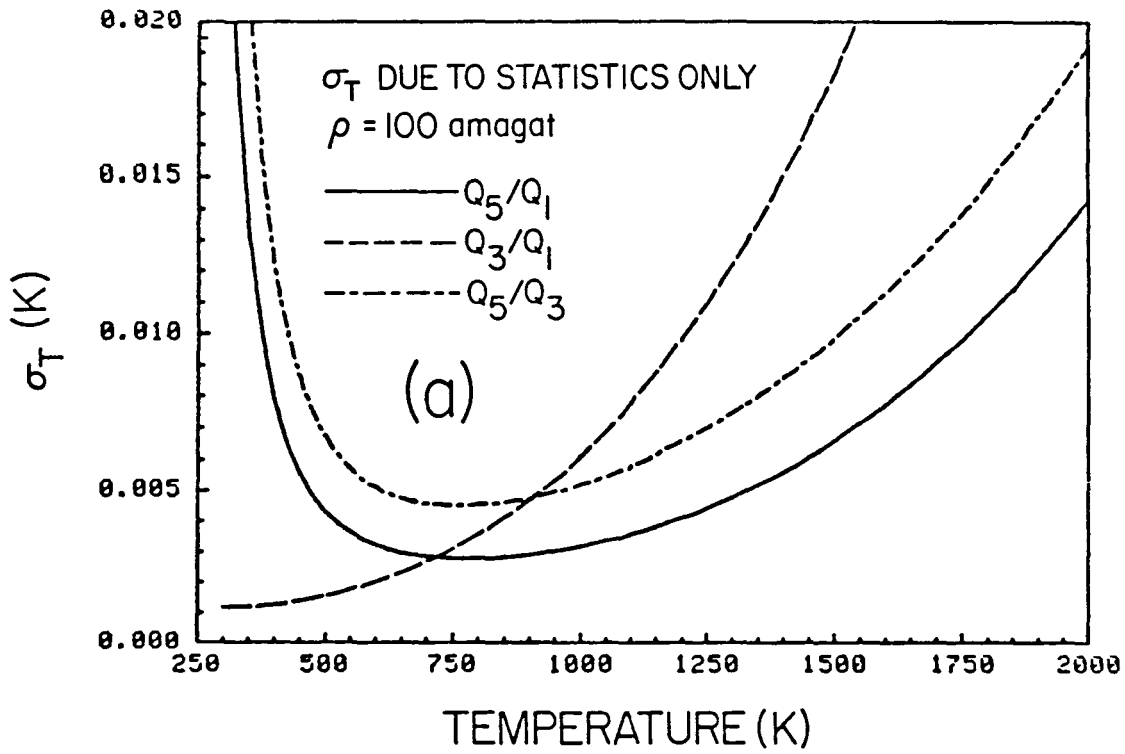
Figure 11. Calculated temperature standard deviation for Q line ratios.
(a) σ_T due to signal statistics only. (b) σ_T due to 0.5% projected error
in measured signal ratio.

due to measurement error in the ratio. These curves were calculated as-
uming a 0.5% relative accuracy ($\sigma_{MR}/R = 0.005$), a reasonable value for
matched detectors when the variation of R is less than two orders of
magnitude.

The uncertainty in the linewidth broadening coefficient can lead to
appreciable error in the temperature at high densities. Figure 12 dis-
plays the error for two cases. If the listed uncertainties of Allin et
al. [22] are used for lines Q(0) - Q(3) (column 1 Table 1) and 0.1×10^{-3}
cm^{-1}/amagat is the assumed error for lines Q(4) and Q(5), the resulting
error in T due to this linewidth uncertainty alone is shown in Figure 12a.
However, the spread among the broadening coefficient values listed in
Table 1 is considerably greater than this error. Figure 12b displays
σ_T due to the uncertainty in Γ_i above if the various broadening coeffi-
cients are assumed to have constant uncertainty of 0.25×10^{-3} cm^{-1}/ama-
gat. Clearly, this uncertainty in the linewidths will contribute sub-
stantially to the uncertainty in the temperature if the published values
in the linewidth are used in the analysis of the data. Using Eq. (31) the
total calculated uncertainty in the temperature can be computed. The re-
sults, using the above parameters and the smaller uncertainties in the
line broadening coefficients, are shown in Figure 13.

It is interesting to note that the ratio that yields the least uncer-
tainty differs for each of the plots. Under the assumptions of Figure 13
the preferred ratio is the Q_3/Q_1 in accordance with the linewidth uncer-
tainties used in Figure 12a. This would not be the case for the more
liberal uncertainties assumed for Figure 12b which indicates the Q_5/Q_1
ratio is the preferred quantity. Near the operating temperature of the
preburner ($\sim$ 1200 K), these calculations indicate a temperature uncertain-
ty of $\sim$ 10-40 K (depending on the linewidth uncertainty assumed) or an
accuracy of 1-3%.

It is possible to extract temperature from the measurements of the
ratios without using the linewidth data by precalibrating the instrument
using a variable temperature high pressure cell. The uncertainty would
then approach that given by Figure 11b. That is, it would be due to the
experimental uncertainty in the ratio. In this case, the Q_5/Q_1 ratio
would be the preferred value to use for temperature extraction consistent
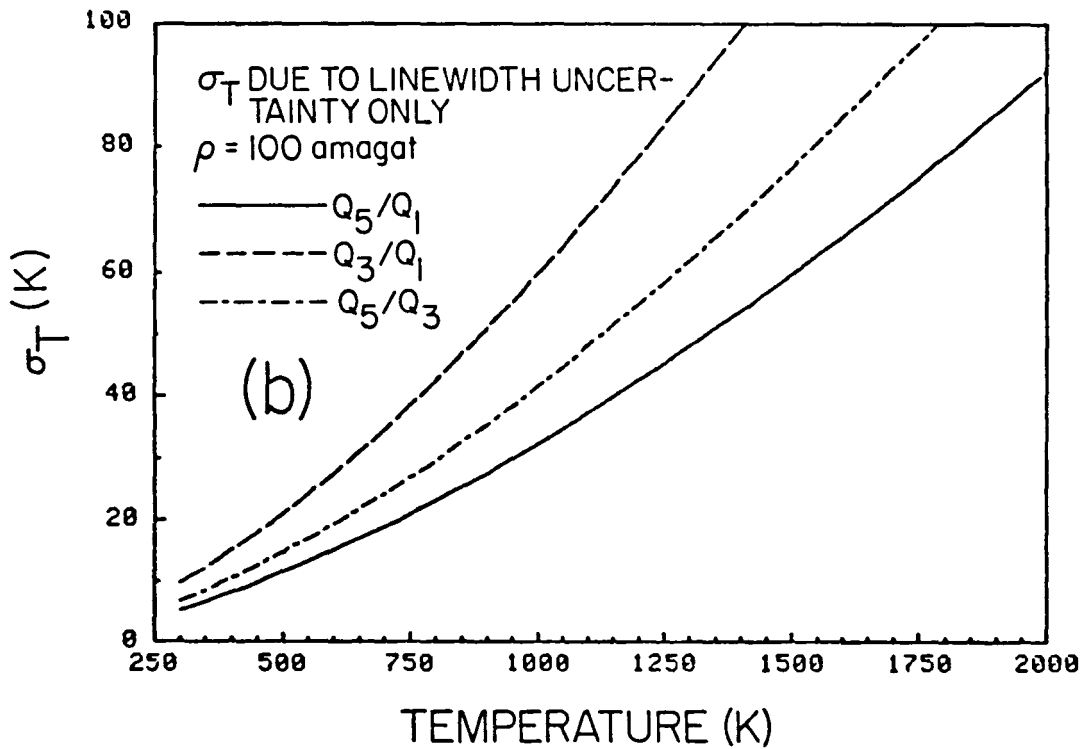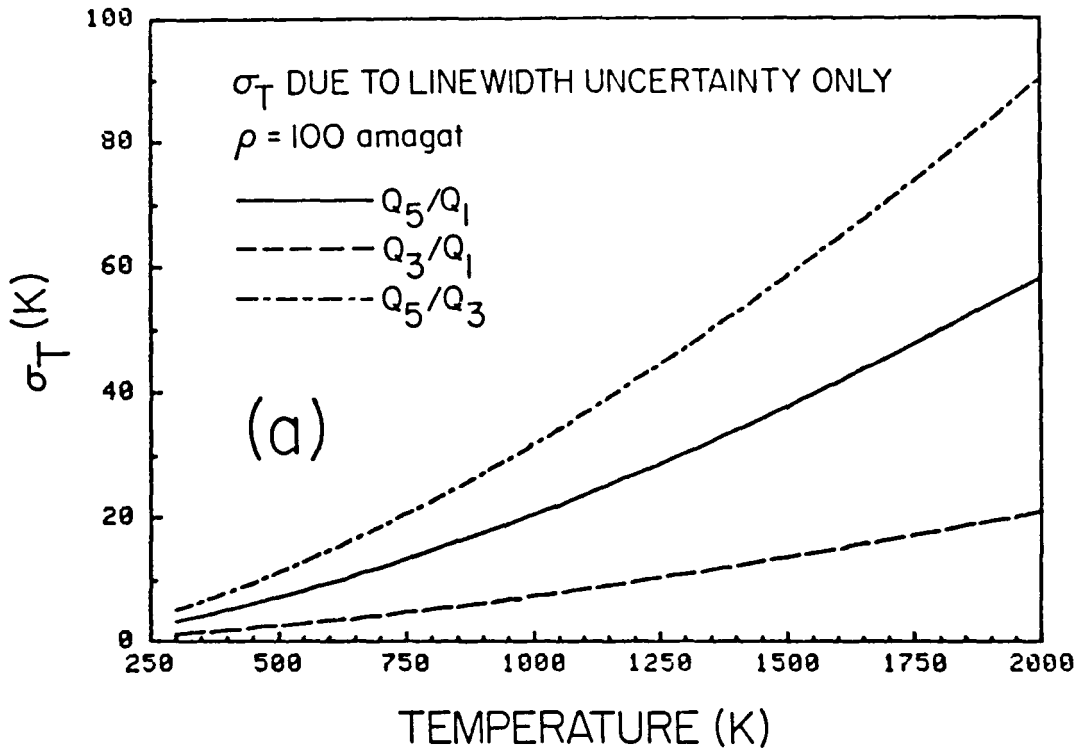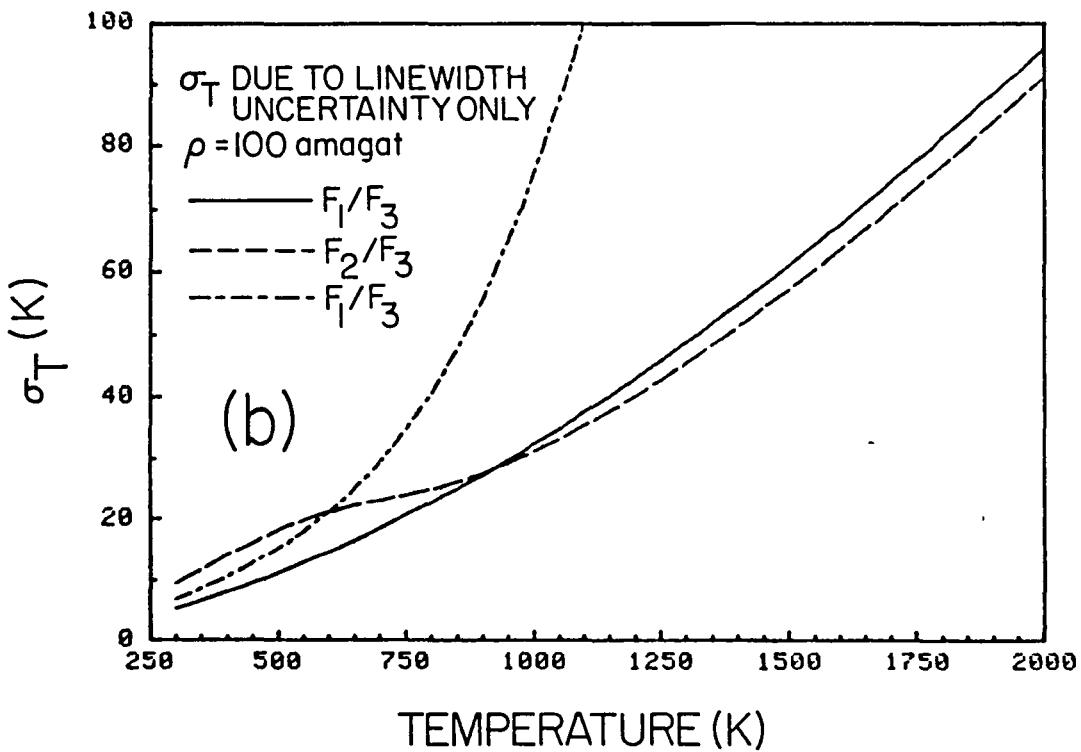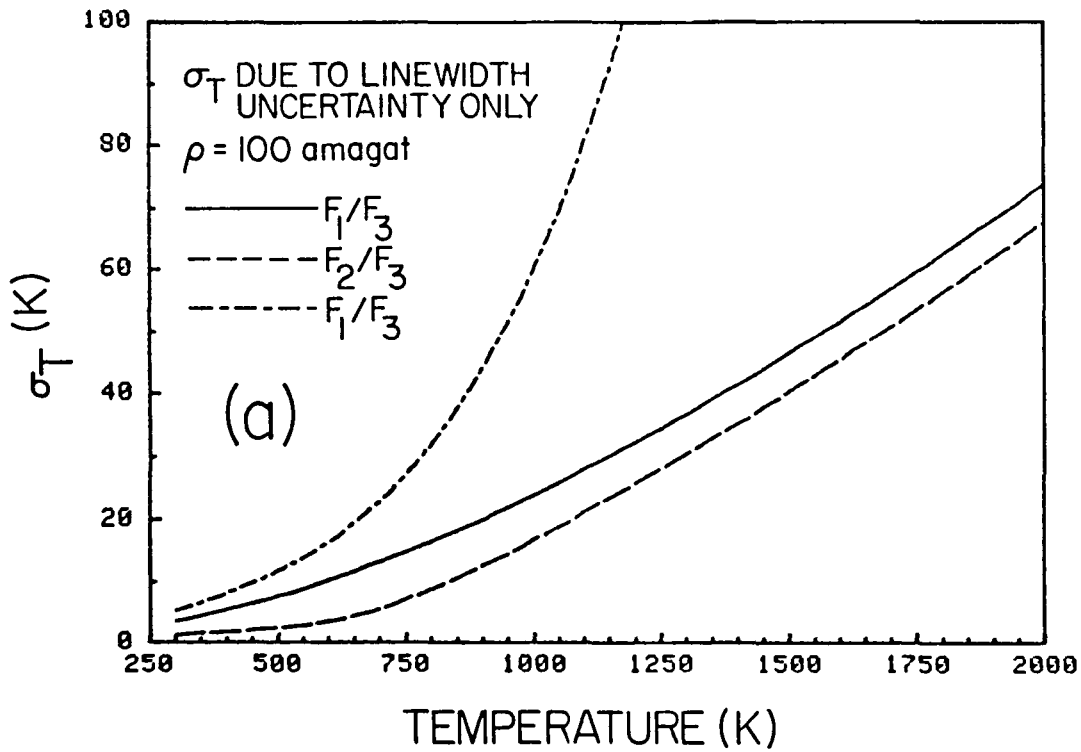
Figure 12. Calculated temperature standard deviation for Q line ratios. (a) σ_T due to linewidth uncertainties of Ref [22]. (b) σ_T due to a constant linewidth uncertainty of $2.5 \times 10^{-4} cm^{-1}$/amagat.
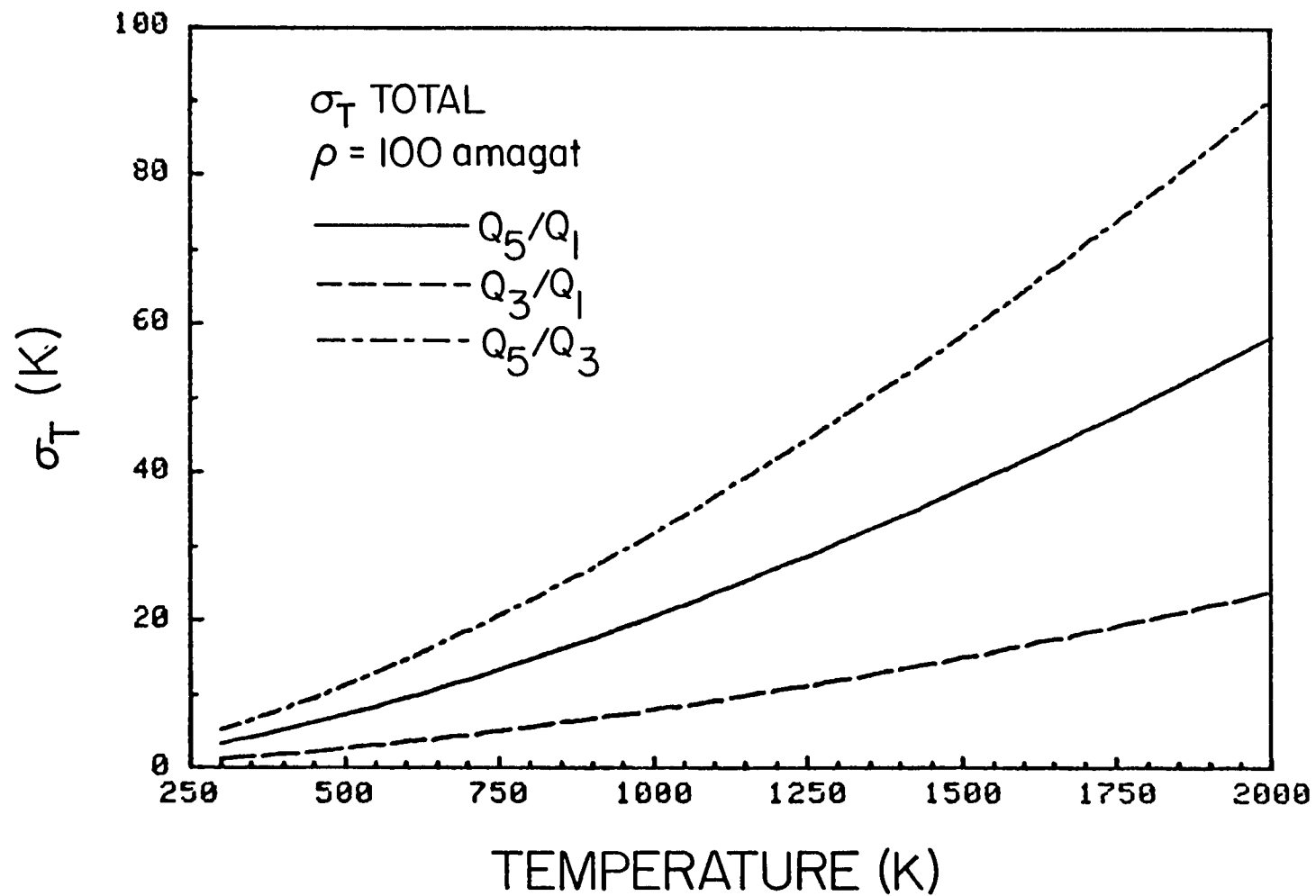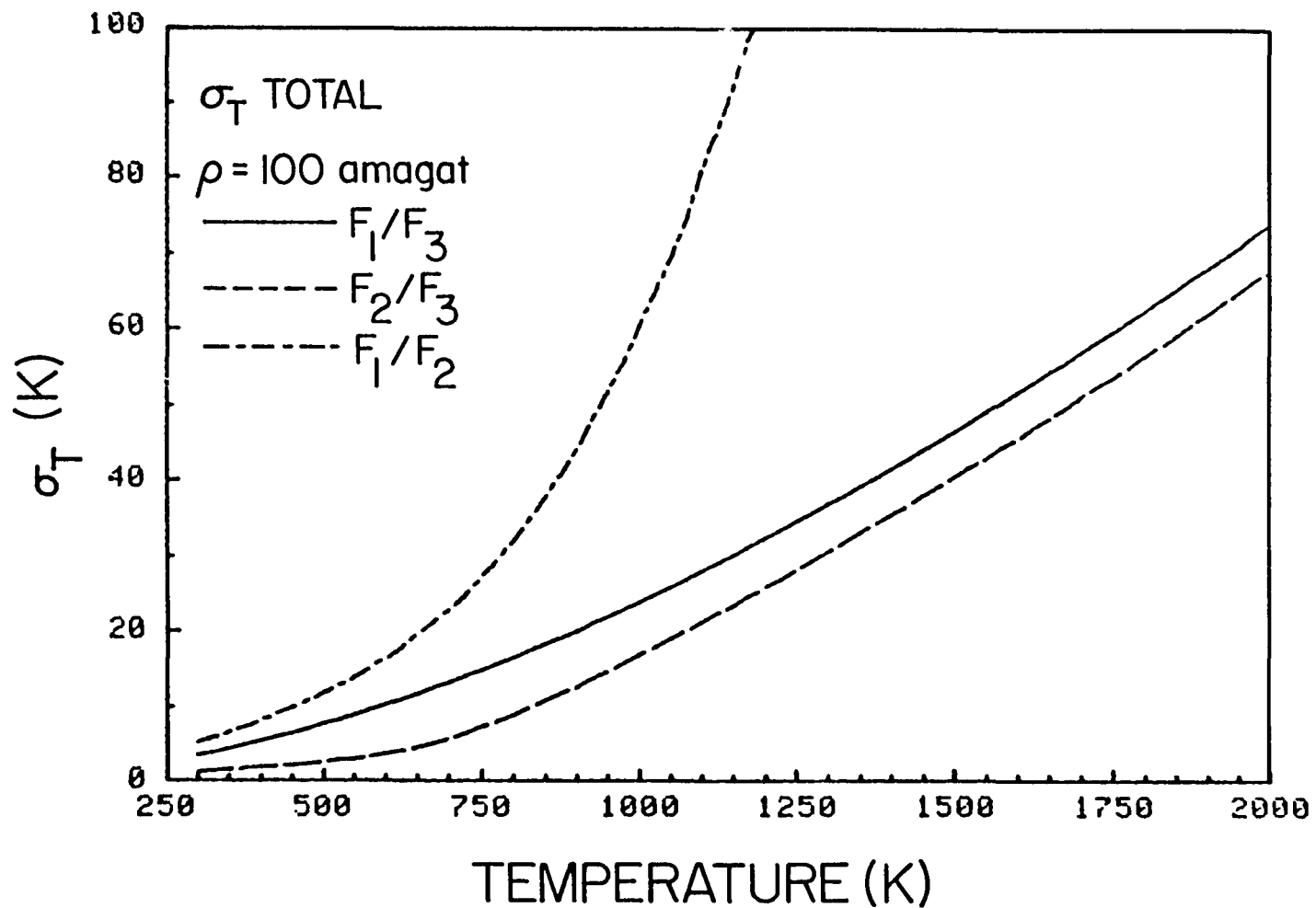
Figure 13. Calculated temperature standard deviation for Q line ratios when the effects of statistics, the linewidth uncertainties of Ref [22], and ratio measurement uncertainty are included.

with the fact it has the steepest slope. Then the temperature uncertainty would be $\sim$ 1.5 (K) at 1200 K corresponding to a 0.1% accuracy.

Figures 14, 15 and 16 show the corresponding error calculations for the filter ratios. Here, the calculation assumes that 40% of the signal is recovered and is divided by a 50% beam splitter, passes through an interference filter with 50% peak transmission and is focused onto a PMT with 0.2 quantum efficiency. The results are similar to those of the Q ratios. Again the uncertainty due to statistics is negligible and somewhat less than those of the Q ratio due to the higher signal throughput and the fact that the filters accept contributions from several lines. The linewidth uncertainties yield somewhat higher temperature uncertainties for the filters because the uncertainties from several lines contribute to the signal from each filter. Using the F_2/F_3 ratio, Figure 16 projects a total uncertainty of $\sim$ 25 K, about 2.5 times greater than that for the Q ratio. Considering the case of a calibrated instrument and using the uncertainty implied by the measured ratio accuracy of Figure 14b, the R_1/R_3 ratio projects only a slightly greater uncertainty in temperature (1.75 K) than the Q_5/Q_1 ratio.

It should be noted that there is another source of error that could not be included in these calculations. A variation of density in the pre-burner due to temperature and/or pressure variations can change the phase-matching angle. Not only will this have the effect of reducing the signal strength, but could also change the relative intensity of the spectral lines in a random fashion as discussed in Section IV. Furthermore, the CARS signal strength used in these error calculations consider the case. of perfect phasematching. This cannot be the accomplished for all the Q lines simultaneously and the signal levels obtained here are surely over-estimates. This would imply greater statistical errors than those shown in Figures 11a and 14a.

Figure 14. Calculated temperature standard deviations for
filter ratios. (a) σ_T due to statistics only. (b) σ_T due
to a 0.5% projected error in measured signal ratio.

45

Figure 15. Calculated temperature standard deviation for
filter ratios. (a) σ_T due to linewidth uncertainties of
Ref [22]. (b) σ_T due to constant linewidth uncertainty of
2.5×10^{-4} cm^{-1}/amagat.

46

Figure 16. Calculated temperature standard deviation for filter ratios when the effects of statistics, linewidth uncertainties of Ref [22], and ratio measurement uncertainty are included.

VII. _Instrument and Facility Considerations_

In this section, the experimental layout of a CARS system is briefly discussed. This system would be capable of producing laser beams and CARS signals with the characteristics discussed in previous sections.

Generally, a CARS system can be divided into three parts: a source of high intensity radiation, beam transfer and focusing optics, and signal recovery and processing assembly. The beam transfer optics are necessarily dependent on the physical design of the test facility and will be discussed last. Due to signal strength considerations the choice of laser for the pump radiation ω_1 is limited to high intensity pulsed lasers for most practical purposes. Of those that are readily available, ruby and Nd:YAG lasers offer the highest intensity. The latter is the first choice since its doubled output can pump visible dyes useful for creating the Stokes laser radiation and has the advantage of offering higher pulse rates resulting in a higher data acquisition rate.

Figure 17 displays the optical design of the front end of a CARS system built around a Nd:YAG laser which is suitable for H_2 temperature measurements. A portion of the second harmonic of the Nd:YAG laser serves to pump a broadband dye laser oscillator-amplifier system. After passing through telescopes that modify the beam diameters and divergences, the pump and Stokes radiation are rendered parallel and relayed to the measurement point. The characteristics of this and similar systems have been discussed previously [52, 53]. Shirley et al. [7] have done single pulsed CARS thermometry of H_2 in laboratory burners using a similar set-up. They find a dye mixture of cresyl violet perchlorate and oxazine 725 satisfactory to efficiently produce the Stokes radiation at 681.5 nm with an acceptable bandwidth when pumped by the second harmonic of a Nd:YAG laser (2xNd). This set-up is sensitive to misalignment and must be placed in a mechanically and thermally stable environment.

There are several methods to process the recovered CARS signal. The three considered in this study are shown schematically in Figure 18 in order of decreasing complexity. The first two require monochrometers while the last needs only narrow band interference filters. The first method will yield the greatest information. Here all the lines of a CAR
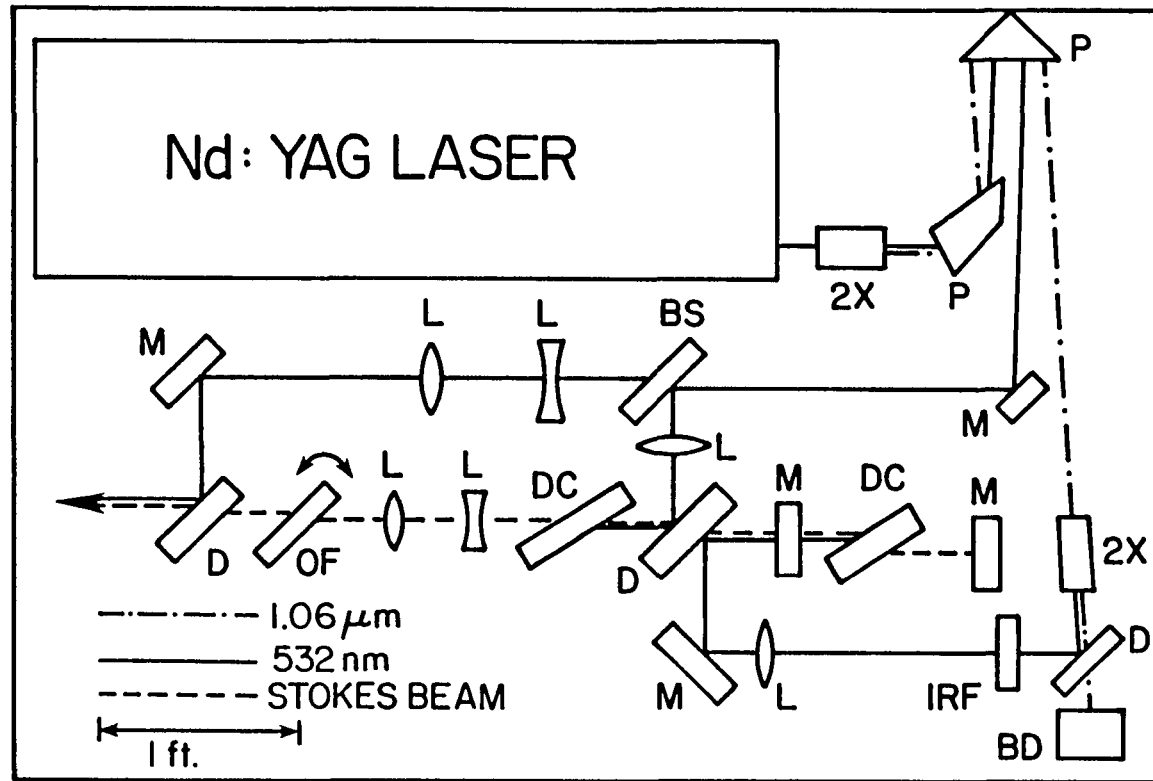
Figure 17. A suitable design for the front end, or laser sources, of a
CARS system. Code: P, prism; 2X, KDP doubler; M, mirror; D, dichroic,
BD, beam dump; IRF, infrared filter; DC, dye cell; L, lens; BS, beamsplitter;
OF, optical flat.
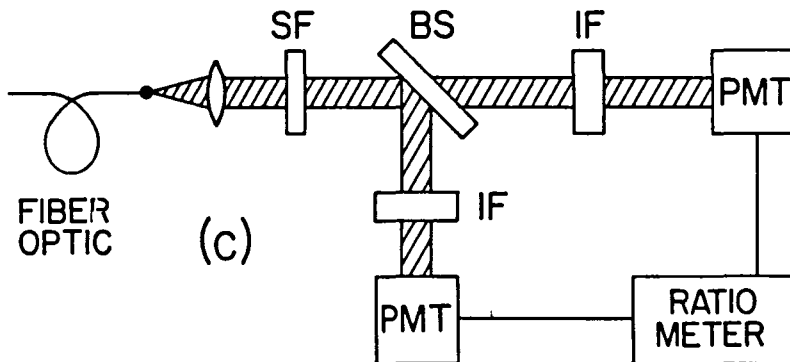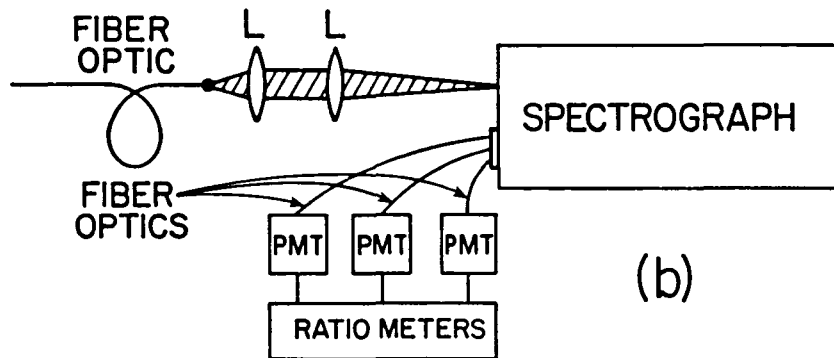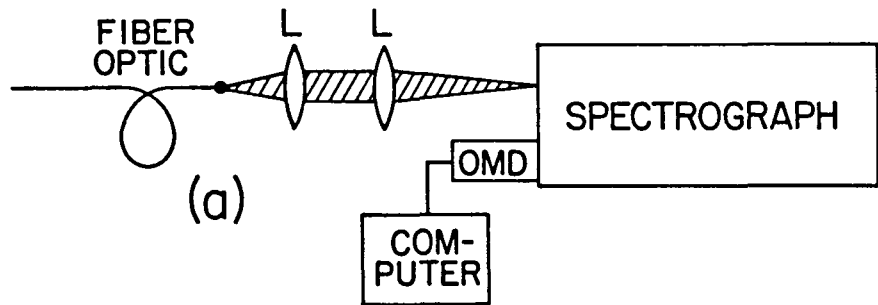
Figure 18. Three variations of detecting and processing H_2 CAR
spectra. (a) Viewing complete spectra using optical multichannel
detector (OMD). (b) Viewing individual odd numbered Q branch
lines. (c) Viewing portion of spectra through interference
filters.

spectrum within an interval defined by the spectral width of the broad-band Stokes laser are viewed using an optical multichannel detector (OMD). This is the most common arrangement used for N_2 CARS thermometry. However, the OMD is expensive and very sensitive to mechanical vibration.

The second technique elimates the OMD and collects the signals from individual Q branch lines using fiber optics and transfers these to photomultiplier tubes. A one meter spectrograph using a 2400 ℓ/mm grating can produce a dispersion of $\sim$ .3 mm/$\mathring{A}$ at the anti-Stokes wavelength. This results in a spatial separation of $\sim$ 1.8 mm between Q(1) and Q(3) lines and $\sim$ 3.3 mm between Q(3) and Q(5) lines - a sufficient distance to allow the placement of optical fibers. The electronic signals are then processed and ratioed.

The last method considered eliminates the spectrograph and uses two interference filters. Interference filters with bandpasses of 10 $\mathring{A}$ are commercially available. Figure 19 shows the spectral position of filters with triangular passbands (somewhat characteristic of two period filters) used in the calculations of Section VI with the positions of several of the Q branch lines indicated. As noted in that section, this technique is somewhat less sensitive to temperature changes than taking ratios of the signals from individual lines. However, due to its simplicity, mechanical stability and insensitivity to signal beam position, it is experimentally the method of choice. This technique is only marginally less accurate than system (b) of Figure 18 when using a ratio calibrated CARS system.

The Fuel Preburner and Test Facility at NSTL

Figure 20 shows vertical and horizontal cross sections of the SSME fuel preburner. A photograph of the interior of the fuel preburner is shown in Figure 21a. The interior diameter of the main wall is 10.89 inches and surrounds a thin (0.05") liner with a 10.43" interior diameter. On some versions, there are two ports of $\sim$ 0.4" diameter located $^-$60° and $^+$165 from the 0° degree line pointed toward the preburner vertical axis (see Figure 21b). These ports may or may not have access to the interior gas flow through the liner. Three vertical baffle plates extend down from the injector head to the centerline of ports at 120° intervals.
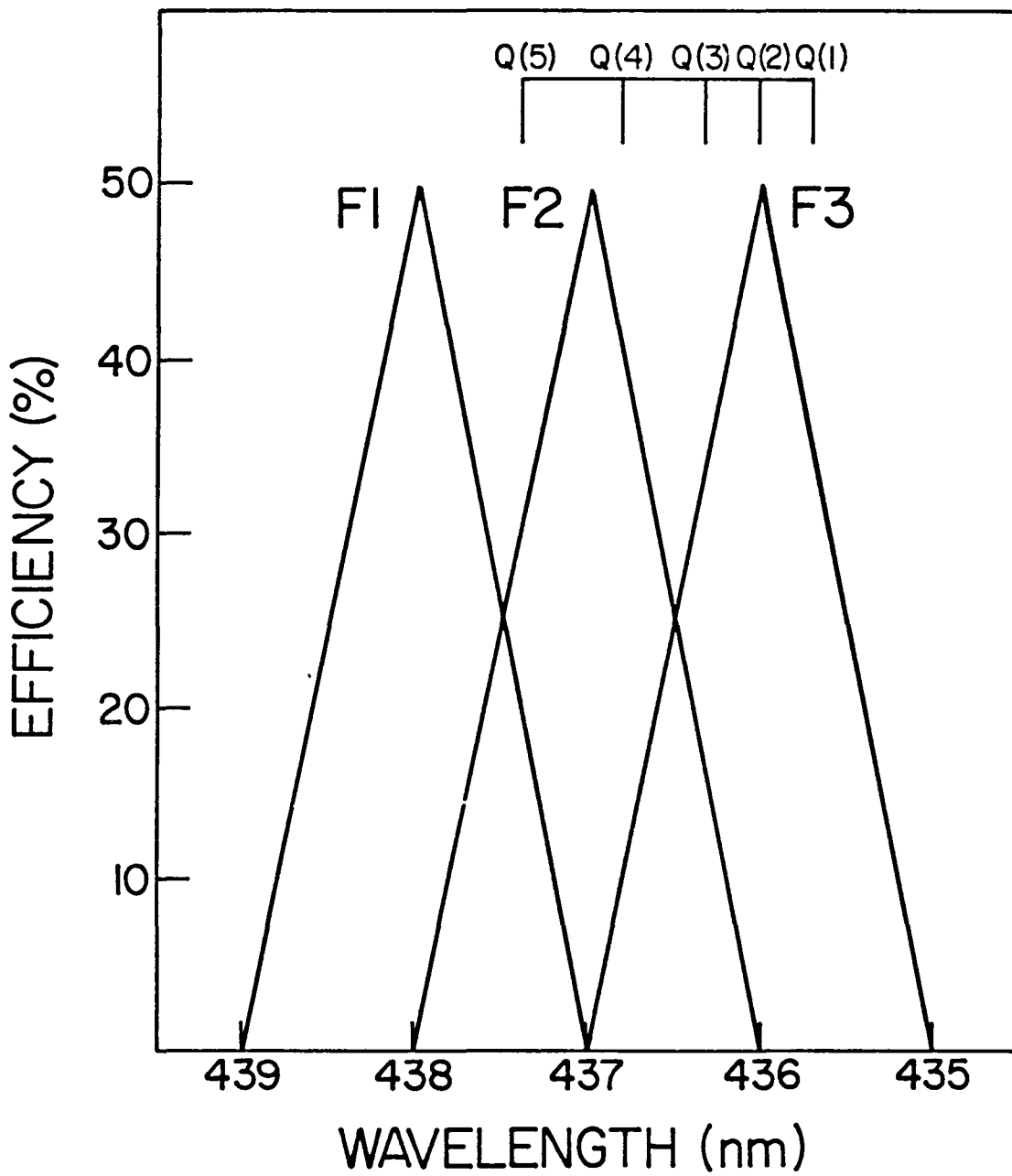
Figure 19. Bandpasses of filters used in calculations of
Section VI. Position of Q branch lines are indicated.
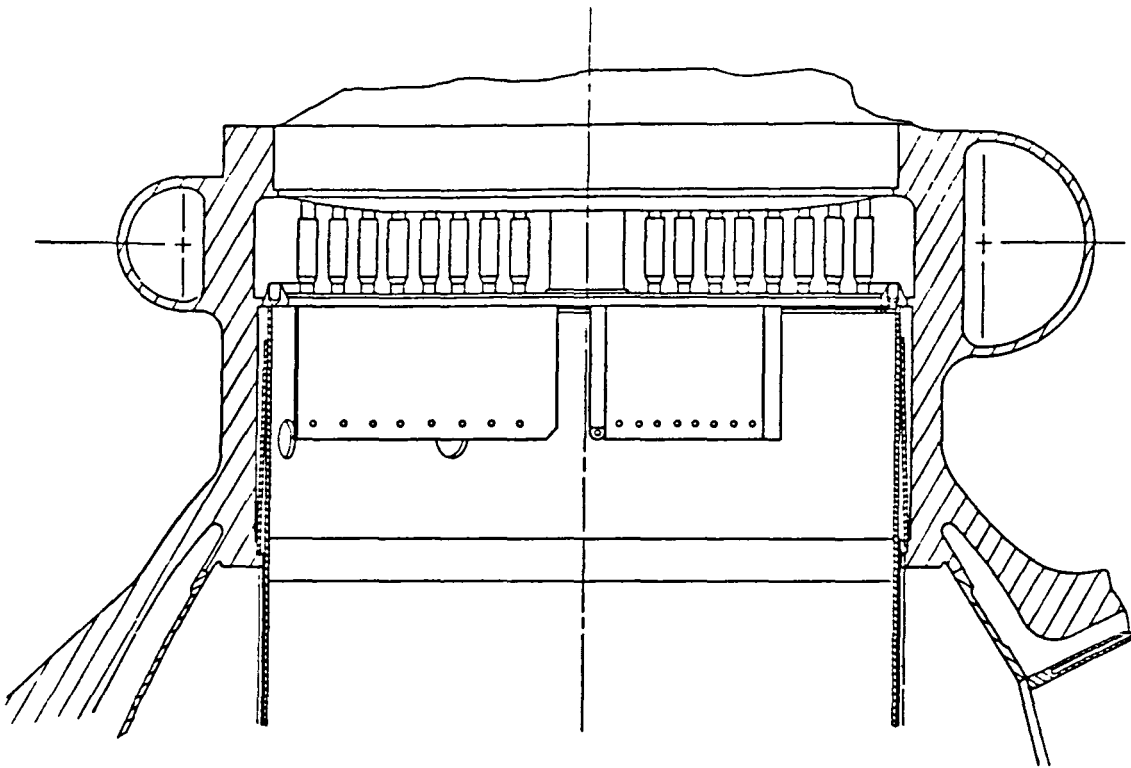
(a)
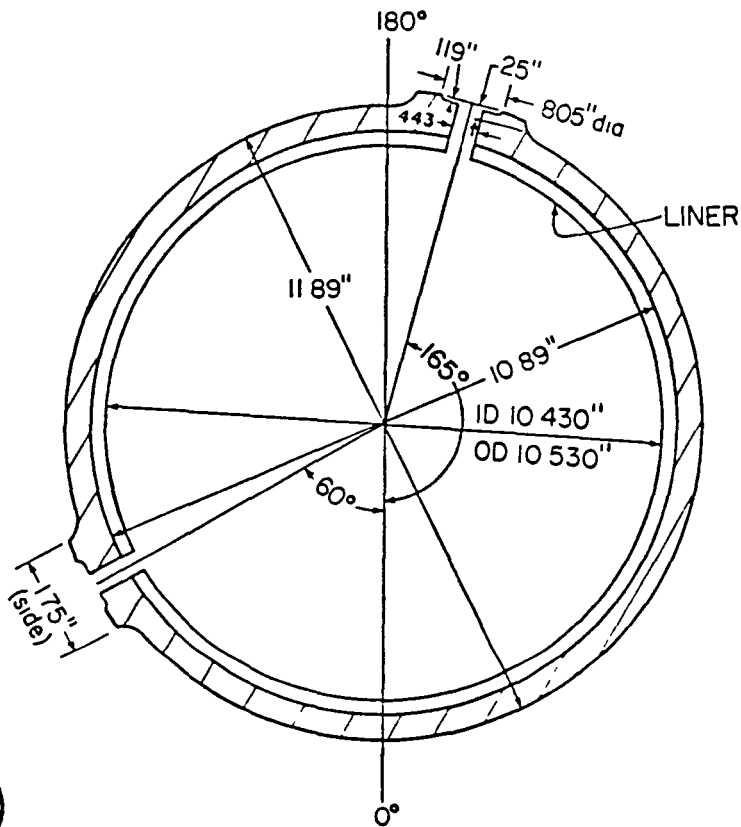
(b)

Figure 20. Two views of the SSME fuel preburner. (a) Three
baffles extend from injector head to center line of ports.
(b) Cross-section showing dimensions and positions of ports and
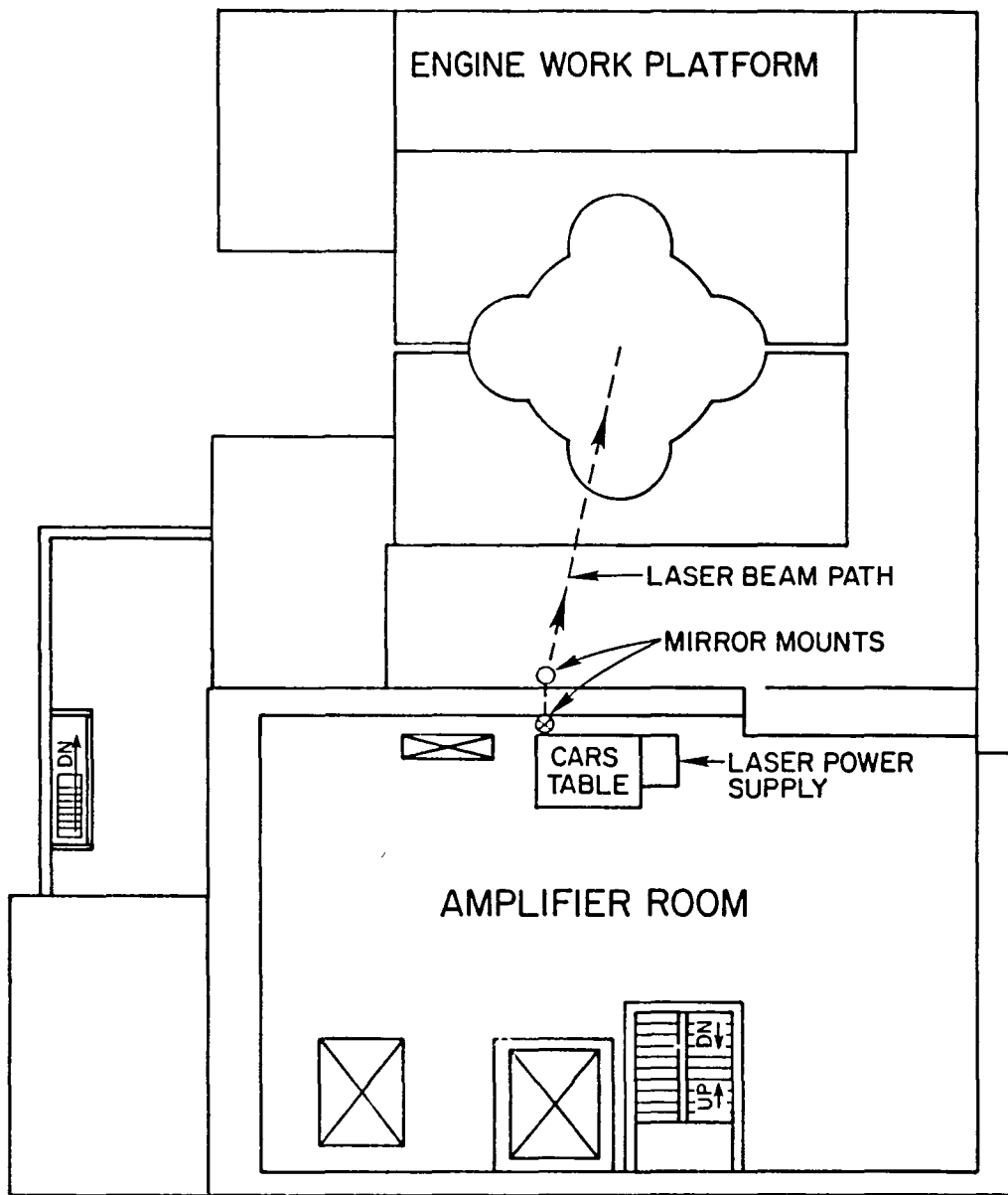liner.
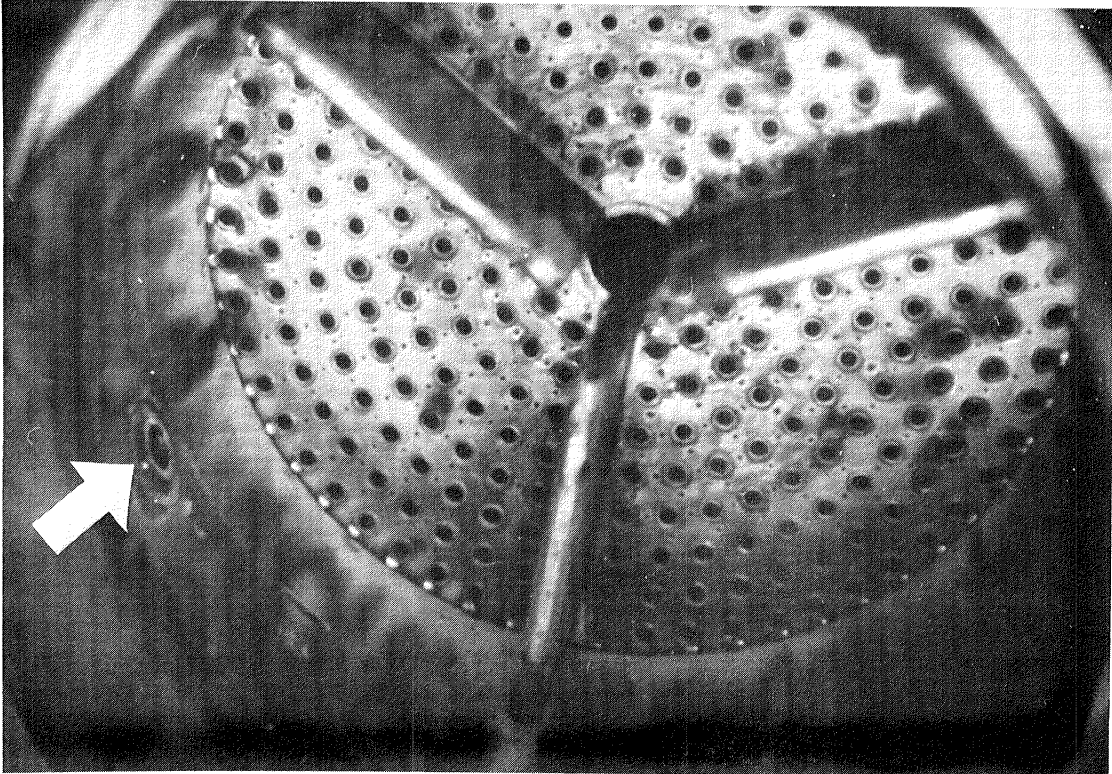
(a)
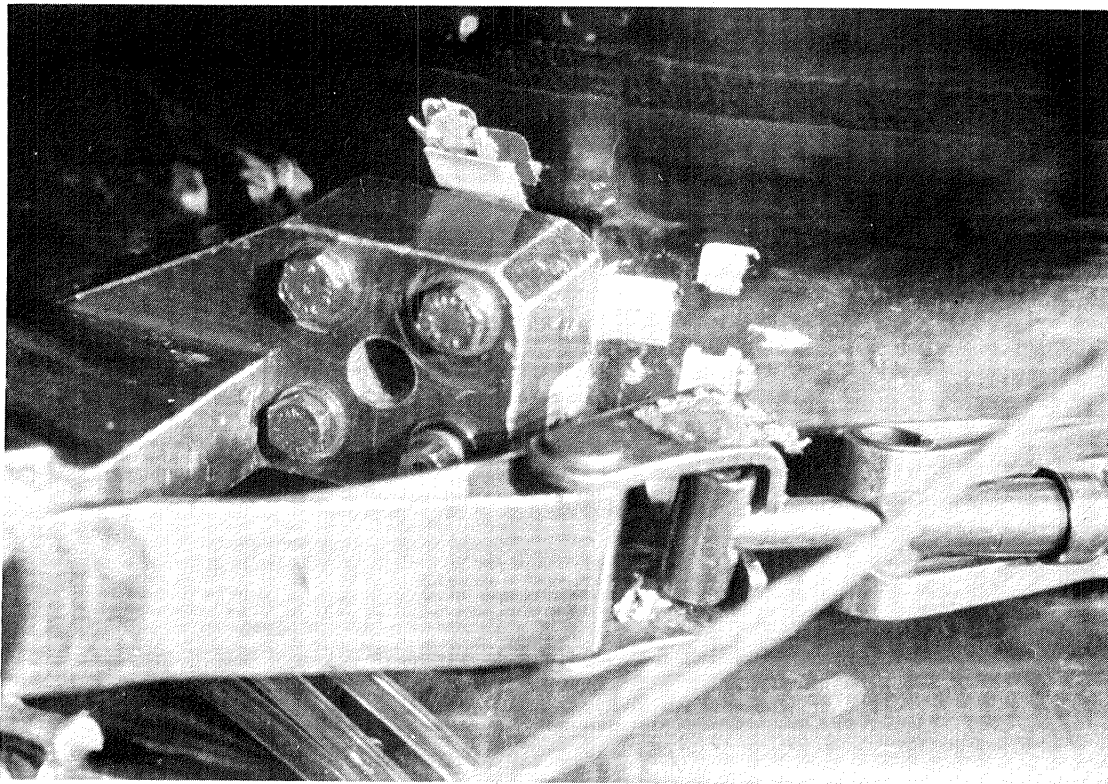
(b)

Figure 21. Two views of SSME fuel preburner. (a) Interior view looking towards injector head. (b) Exterior view of ∿1.0 cm diameter port.

At NSTL the preburner is located on the 4th floor of the test stand building. During assembly the SSME is surrounded by temporary metal flooring which allows access to the engine components. During a test, these grates are removed and the remaining flooring is ∿ 15 feet from the SSME. This permanent deck, mounted on a ∿ 2½ feet thick concrete wall, is one level below a room that houses the electronics for processing the data received from the sensors placed on the test engine. This amplifier room is a vibration-free, thermally stable environment.

A possible physical configuration for the location of the laser system and beam transfer optics is shown in Figure 22. The CARS system shown in Figure 17 could be placed in the amplifier room·near the concrete wall. The parallel pump and Stokes beams would pass through the floor of this room, be rendered horizontal by a prism secured to the concrete wall, pass through the wall and be transfered to a mirror mounted directly to the preburner by another mirror mounted directly to the other side of the concrete wall. Because of the severe vibration, no optics could be mounted on any other surrounding structures.

Figure 23 shows a mechanism that could accept the transferred beams. Here a lens that rides on a travelling nut of a lead screw assembly serves to focus and cross the incoming beams. The crossing point of the beams defines the region where the measurement is taken and this point is transferred across the preburner by the movement of the lens. The CARS signal thus created passes through a spectral filter and is focused by a short focal length lens onto an optical fiber. This fiber transfers the signal back to the amplifier room for processing. The focal length of this lens and the diameter of the fiber are chosen such that maximum diameter of the focused signal beam does not extend beyond the diameter of the fiber optic. The ports are shown in the same position as those that currently exist on the fuel preburner. The 12" to 14" clearance necessary for the travelling lens assembly is available in the current setup. Only ∿ 3 inches of clearance is available outside the other port and hence the need for a compact recovery arm. With ports placed at these positions, a temperature profile would be taken across a chord instead of the diameter of the pre-burner. This is a desirable situation from an experimental point of view as the gas streamlines are expected to be static in this region while the

ENGINE WORK PLATFORM

LASER BEAM PATH

MIRROR MOUNTS

CARS TABLE

LASER POWER SUPPLY

AMPLIFIER ROOM

DN

IN

UP

FIFTH FLOOR PLAN EL 97'0"
SCALE 1/8"= 1'0"

Figure 22. Fifth floor plan of test stand facility at NSTL. The possible location of a CARS system is shown in the amplifier room which is one level above the fuel preburner. Positions of mirror mounts attached to the concrete wall are indicated.
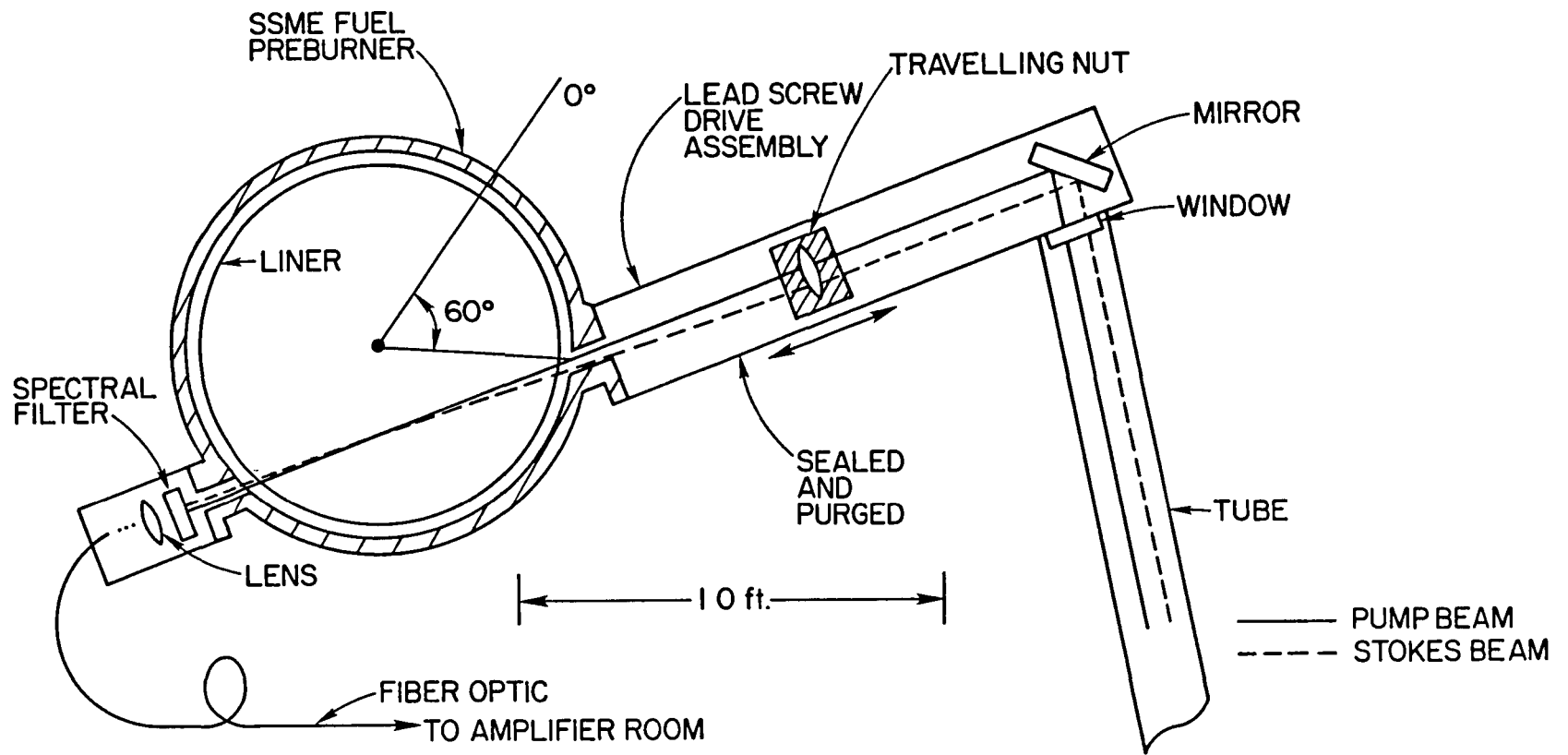
Figure 23. Hypothetical beam receiving arm attached to fuel preburner. All optics and beam paths are hermetically sealed.

center is believed to be subject to turbulence. The windows of the ports could be made of crystaline sapphire as it has excellent mechanical strength, high temperature stability, chemical inertness, and good optical transmission (its melting point is above 2300 K and a 0.5 inch diameter, 0.2 inch thick window has a hydrostatic burst point of 9600 psi with a built-in safety factor of 3 [54]). Because of the cryogenic fuel flowing through the rocket system, all fixtures attached to the preburner must be purged to avoid frozen condensate. Furthermore, all beams must be transferred in hermetically sealed tubes as the air adjacent to the SSME becomes clouded during tests.

It is useful to consider a few numbers in light of the geometry of the fuel preburner and test facility. As discussed in Section IV, hydrogen has considerable optical dispersion at high densities requiring a simple two beam phasematching geometry. At a density of 100 amagat the crossing angle Θ is $\sim 0.8°$. Using simple geometry, two beams of width d can overlap over a length of no more than $\ell = d/\sin(\Theta/2)$. The diameter of a laser beam with a Gaussian intensity profile focused by a lens of focal length f is $\sim 2f\delta_{1/2}$ where $\delta_{1/2}$ is the half angle divergence of beam. As indicated in Figure 23 a lens with a 36 cm focal length would allow measurements to be made across a chord of the preburner. Taking $\delta_{1/2} \simeq 0.25$ mrad (factory specification of a Quanta Ray Nd:YAG laser) one finds $\ell \sim 2$ cm. This crossing angle and lens also result in a pump and Stokes beam separation of ~ 0.5 cm at the lens. If both beams have a 0.5 cm diameter, then the ports in the preburner should have approximately 1 cm diameter (or somewhat larger to facilitate alignment). In accordance with the discussion in Section IV, the angle between the Stokes and pump beams must be maintained to an accuracy better than the individual beam divergences. This indicates that beam separation tolerance of less than 8.75×10^{-3} cm over the path length of the relay system (~ 25 meters). Our experience is that this can be achieved if single optical components are used to relay both beams. However, these components must not be stressed and the vibration of these pieces must be less that required to cause the focused CARS signal to wander from the end of the fiber optic (~ 1 mm for a macrofiber). Furthermore, it is likely that once set up the system will require an initial alignment under operating density to maximize the

58

signal.

In order for this design to be implemented, the following conditions must be met. Two facing ports with at least 1 cm diameters and an unobstructed line of sight view of each other must be available in the preburner. In current preburners, the ports have marginally adequate diameters, but do not face each other and offer no through-beam access. Furthermore, half the area of the current ports are obstructed by the baffles extending from the injector head. Line of sight access must exist from the main concrete wall to the preburner, through the concrete wall, and from the outside of the concrete wall to the amplifier room. It is believed that this access could be made available, albeit with some modifications to the test facility. Mirror mounts and housings must be anchored directly to the concrete wall and not to surrounding structures.

VIII. _Conclusions and Recommendations_

The theoretical analysis in this report indicates that temperature measurements can be made using CAR spectra of hydrogen with the spatial and temperature precision indicated in NASA RFP No. 8-1-2-EC-25732 (0.25 to 0.5 in^2 and 10 °R). The temperature resolution for a calibrated instrument will be limited by the precision with which the ratio of signals from individual rotational lines can be measured. Spatial resolution can approach $\sim$ 2 cm in the longitudinal direction (with respect to beam direction) and $\sim$ 0.01 cm in a tranverse direction. The time resolution would be limited by the pulse width of the laser ($\sim 10^{-8}$ sec) with a data acquisition rate limited by the pulse rate available from high power Nd:YAG lasers (currently $\sim$ 30 Hz).

A study of the physical environment of the test facility and access to the currently configured fuel preburner does not present such a sanguine picture. As presently configured, there is no acceptable optical access to the preburner. CARS requires two line of sight optical ports with clear access diameters of $\sim$ 0.5 in. and modifications to the preburner would have to be made. Furthermore, the area adjacent to the SSME is subject to extreme vibration during a test and is unsuitable for the placement of spectroscopic equipment. This requires a system of relay optics over which critical alignment must be maintained.

Because there are unknowns in the physical environment during a test firing, several on site tests are recommended before proceeding with a CARS temperature measurement. The amount of physical motion experienced by optical mounts anchored to the main concrete support wall and an arm attached to the preburner port must be measured. The observation of beam wander over the projected light path during a test firing measured using a HeNe laser and a reticon detector would be a simple and useful test. In addition, the amount of deviation experienced by a laser beam passing through the preburner during a firing also should be measured. Significant deviations caused by turbulence-induced index of refraction gradients could cause significant dephasing of the pump and Stokes beams.

Since there are several untested aspects of the CARS technique in this environment it is also advisable to undertake a number of

laboratory measurements using a variable temperature high pressure cell.
CARS generated in high pressure hydrogen would allow a system to be cali-
brated taking note of the sensitivity of the variation of line intensities
as a function of the phasematching angle. These studies could also be
used to eliminate many of the uncertainties associated with the linewidth
pressure broadening coefficients considering the paucity of data avail-
able on their variation as a function of temperature. In addition, this
work could set experimental limits on the effects of stimulated Raman
gain and laser induced gas breakdown for hydrogen. Finally, more real-
istic limits on the absolute signal strength could be obtained since
the theoretical limits are seldom realized even under the most ideal
experimental conditions.

Appendix A
Density to Pressure Conversion

The conversion from pressure to density for a given temperature is readily accomplished using the equation of state. Using Van der Waal's equation for H_2 [55]

$$\left(P + \frac{n^2 a}{V^2}\right)\left(V - nb\right) = nRT$$

where   n = number of moles of gas

R = 0.08206 liter atm mole^{-1} K^{-1}

P = pressure in atmospheres

V = volume in liters

and for H_2

a = 0.2444 (liters)^2 atm/mole

b = 0.02661 liters/mole

If $\eta \equiv n/V$ (molar number density), then the above equation can be written

$$ab\eta^3 - a\eta^2 + (bP + RT)\eta = P$$

and η/η_0 is the density in amagat where η_0 is the molar number density at T = 273.15 K and P = 1 atm. Figures A1 and A2 show pressure verses density for the temperatures, pressures and densities important to this study.

.
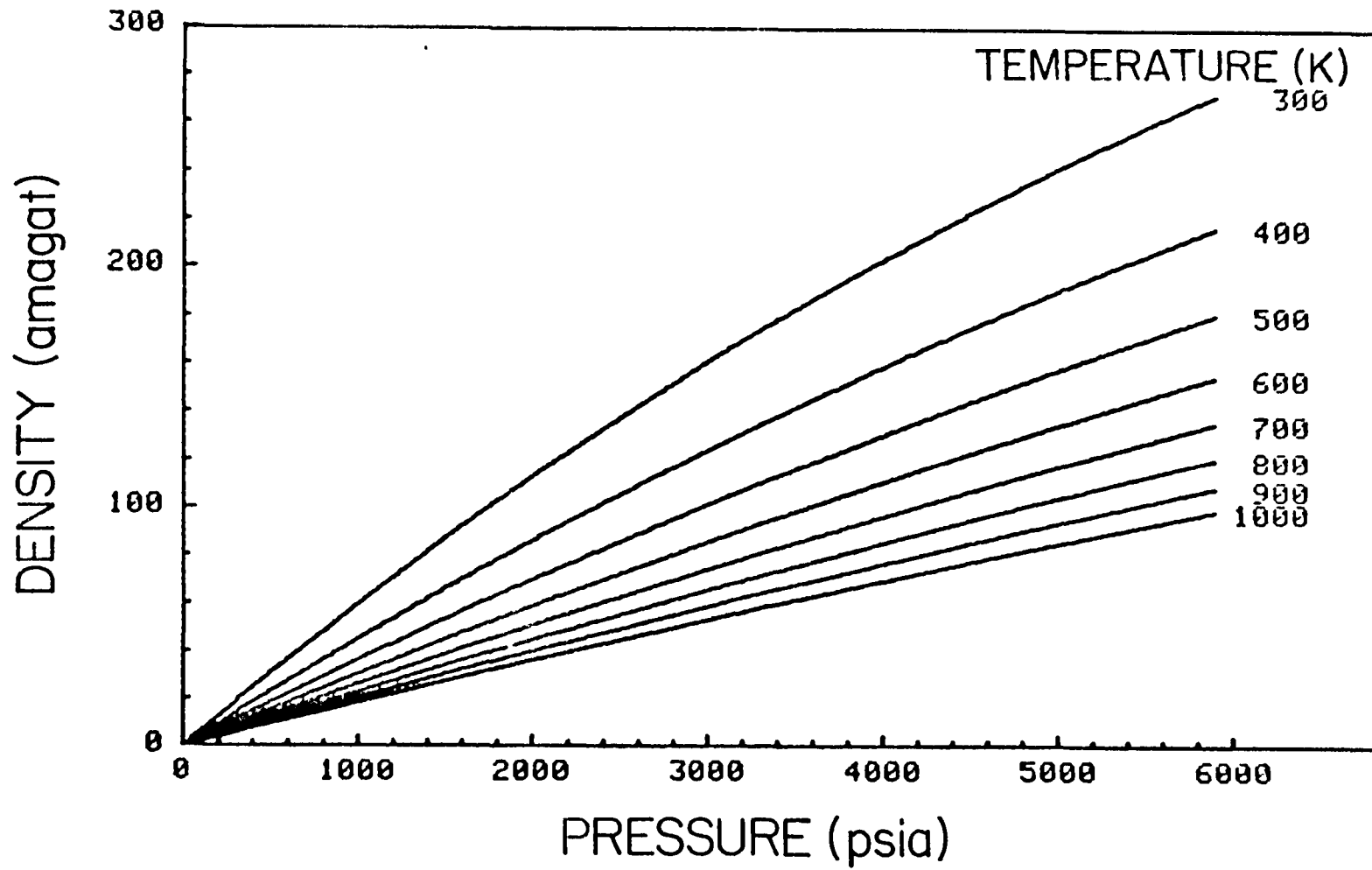
Figure A1. H_2 pressure-density curves, $300 \leq T \leq 1000$ K.
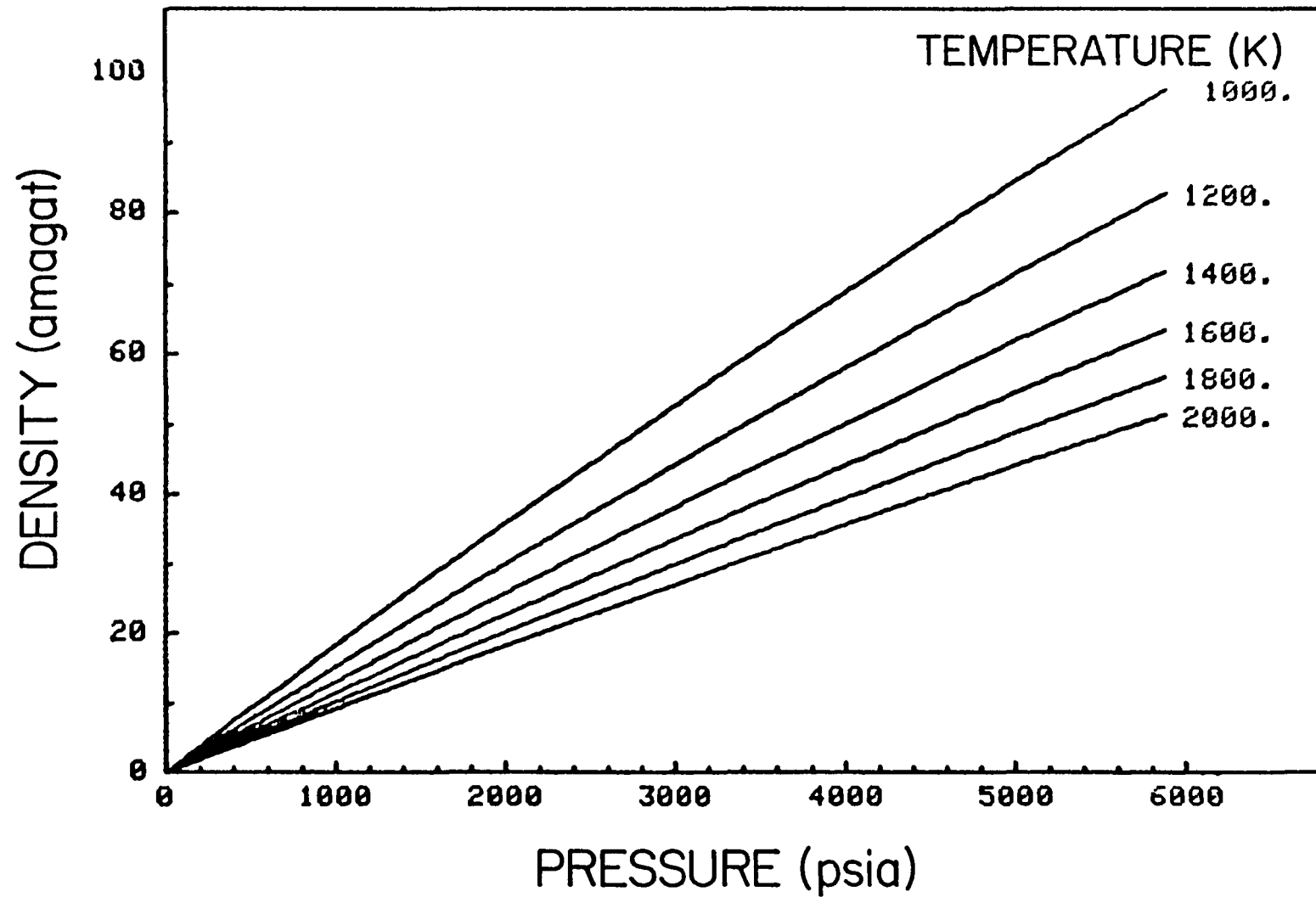
Figure A2.   H$_2$ pressure-density curves, 1000 ≤ T ≤ 1000 K.

Appendix B
Raman Cross Section

The Raman cross section for forward scattering as a function of rotational quantum number is [14]

$$\frac{d\sigma}{d\Omega}\bigg|_Q = \left(\frac{\omega_2}{c}\right)^4 \frac{\hbar}{2\omega_o} \left[\frac{\alpha^2}{M} + \frac{7}{45}\left(\frac{\gamma^2}{M}\right) b_J^J\right] (v + 1) \qquad (B1)$$

$$\frac{d\sigma}{d\Omega}\bigg|_{0,S} = \left(\frac{\omega_2}{c}\right)^4 \frac{\hbar}{2\omega_o} \frac{7}{45} \left(\frac{\gamma^2}{M}\right) b_{J\pm2}^J (v + 1)$$

It is often useful to be able to calculate α and γ from the Raman scattering cross section σ_{zz} (the cross section for scattering an incident beam travelling along the x-axis with polarization in the z-direction into the x-y plane with polarization in the z-direction) and the depolarization ρ (the ratio of light intensity scattered in the y-direction polarized in the x-direction to that polarized in the z-direction for an incident beam travelling in the x-direction polarized in the z-direction).

$$\frac{\alpha^2}{M} = \frac{2\omega_o}{3\hbar g_v}\left(\frac{c}{\omega_2}\right)^4 \frac{(3 - 4\rho)}{1 + \rho}\sigma_{zz} \quad ; \quad \frac{\gamma^2}{M} = \frac{30\omega_o}{\hbar g_v}\left(\frac{c}{\omega_2}\right)^4 \frac{\rho}{1 + \rho}\sigma_{zz}$$

Taken from

$$\rho = \frac{3\gamma^2}{45\alpha^2 + 4\gamma^2} \quad ; \quad \sigma_{zz} = \frac{\hbar}{90M\omega_o}\left(\frac{c}{\omega_2}\right)^4 g_v (45\alpha^2 + 7\gamma^2)$$

See Ref. (56, 57, 58).

The Placzek-Teller coefficients are available from several references (59, 60, 61). For a diatomic molecule

$$b_J^J = \frac{J(J + 1)}{(2J-1)(2J+3)}$$

$$b_{J+2}^J = \frac{3}{2}\frac{(J+1)(J+2)}{(2J+1)(2J+3)}$$

$$b_{J-2}^J = \frac{3}{2}\frac{J(J-1)}{(2J+1)(2J-1)}$$

$g_v = v + 1$ is contributed by the vibrational matrix element.

Application to Hydrogen

$$\omega_2 = 2.714 \times 10^{15} \text{ rad/sec} \quad (14396 \text{ cm}^{-1})$$

$$\omega_o = 7.832 \times 10^{14} \text{ rad/sec} \quad (4155 \text{ cm}^{-1})$$

$$\rho = 0.07$$

$$\left.\begin{array}{l}\dfrac{\alpha^2}{M} = 1.8 \times 10^{-8} \text{ cm}^4 \text{ gm}^{-1} \\[2em] \dfrac{\gamma^2}{M} = 1.08 \times 10^{-8} \text{ cm}^4 \text{ gm}^{-1}\end{array}\right\} \text{Ref [10]}$$

and

$$\chi_{NR} = 9.75 \times 10^{-18} \text{ cm}^3 \text{ erg}^{-1} \text{ [17]}$$

Analysis shows [62] that for very light molecules the Q branch matrix element is subject to a J-dependent correction factor i.e. Eq.(B1) must be multiplied by (see [63])

$$\left[1 + \frac{3}{4} \left(\frac{2B_e}{\omega_e}\right)^2 (|a_1| - 1) \; J(J + 1) \right]$$

where a_1 is the first Dunham anharmonic coefficient [64]. Using Eq.(19) of Ref [65] a_1 can be written

$$a_1 = \frac{H_e \omega_e^4}{16 B_e^5} - 3$$

$$= -1.62293 \text{ cm}^{-1}$$

where the remaining constants are defined in Appendix D.

Appendix C
Population Difference Between Initial and Final States Δ_j

The fractional population difference between upper and lower rota-
tional-vibrational energy levels is

$$\Delta_j = f_{v'J'} - f_{vJ}$$

where f_{vJ} is the fraction of molecules in the energy level designated by
v and J.

In thermal equilibrium, the fraction of molecules in a quantum mech-
anically allowed eigenstate is equal to the Boltzman factor divided by
the partition function Q [66]

$$f_i = \frac{\exp(-E_i/kT)}{Q}$$

If there are degenerate states, the fraction of molecules in a given energy
level is weighted by the degree of degeneracy or the statistical weight g_k

$$f_k = \frac{g_k \exp(-E_k/kT)}{Q}$$

where the partition function is given by

$$Q = \sum_{\substack{\text{all} \\ \text{states}}} \exp(-E_i/kT) = \sum_{\substack{\text{all} \\ \text{levels}}} g_k \exp(-E_k/kT)$$

Considering all degrees of freedom (electronic motion and spin, nuclear
motion and spin) but considering Λ-doubling to be zero and all electron
and nuclear spin levels to be degenerate, f_{vJ} can be written as

$$f_{vJ} = \frac{(2 - \delta_{0\Lambda})(2S + 1)\ (2J + 1)[\Sigma(2T + 1)]}{Q} \exp(-E_{vJ}/kT)$$

where $(2 - \delta_{ov})$ accounts for Λ-doubling
  $(2S + 1)$ is the electronic spin statistical weight
  $(2J + 1)$ is the statistical weight of a given rotational level
       excluding nuclear spin
  $\Sigma(2T + 1)$ is the sum over all allowed nuclear levels weighted by the
       number of their magnetic sublevels.

The values of T are taken from the individual nuclear spins of the atoms (I_1, I_2), i.e.

$$T = |I_1 + I_2|, |I_1 + I_2 - 1|, \ldots |I_1 - I_2|$$

However, for homonuclear molecules, the symmetry of the total wavefunction is preserved by allowing only even values of T for symmetric wavefunctions and only odd values of T for antisymmetric wavefunctions.

If the various degrees of freedom are considered to be completely decoupled (which is not always the case, as indicated below) then the partition function can be approximated by

$$Q \simeq Q_{el} \, Q_v \, Q_{rot} \, Q_{es} \, Q_{ns}$$

For all temperatures important to combustion, only the ground electronic state will contribute appreciably to the sum (ignoring Λ-doubling).

$$E_{el} \equiv 0 \quad \text{so} \quad Q_{el} = 1.$$

The vibrational term energy can be written

$$G(v) = \omega_e(v + \tfrac{1}{2}) - \omega_e x_e(v + \tfrac{1}{2})^2 + \ldots$$

Defining the zero point energy $(\omega_e/2)$ to be at $E = 0$

$$\bar{G}(v) = v(\omega_e - \omega_e x_e v + \omega_e y_e v^2 + \omega_e z_e v^3 + \ldots)$$

$$v = 0, 1, 2, \ldots$$

$$Q_v \simeq 1 + \exp(-hc\omega_e/kT) + \exp(-2hc\omega_e/kT) + \ldots$$

The rotational energy can be approximated by

$$F(J) = BJ(J+1) - DJ^2(J+1)^2$$

$$J = 0, 1, 2, \ldots$$

$$Q_{rot} = \sum_{\substack{all \\ states}} \exp(-E_J/kT) = \sum_{\substack{all \\ levels}} (2J+1)\exp(-F(J)/kT)$$

$$\simeq (1 + 3\exp(-2hcB/kT) + 5\exp(-6hcB/kT) + \ldots)$$

For sufficiently large T or small B (see Ref. 67):

$$Q_{rot} \simeq \int_o^\infty (2J+1) \exp[-hcBJ(J+1)/kT]dJ = \frac{kT}{hcB}$$

$$Q_{es} = \sum_{\substack{all \\ states}} \exp(-E_{es}/kT)$$

$$= (2S + 1) \text{ for degenerate electron spin states.}$$

$$Q_{ns} = \sum_{\substack{all \\ states}} \exp(-E_{ns}/kT) = \sum_{\substack{all \\ levels}} (2T + 1) \exp(-E_{ns}/kT)$$

$$= \sum_T (2T + 1) \text{ for degenerate states.}$$

The Boltzman factor is given by

$$f_{BOLTZ} = \exp[-E_{TOTAL}/kT]$$

$$E_{TOTAL} = hc\left(T_e + \bar{G}(v) + F(J)\right)$$

$T_e = 0$ for ground electronic state (cm^{-1})

$$\bar{G}(v) = G(v) - G(0)$$

$$= G(v) - \frac{1}{2}\left(\omega_e - \frac{\omega_e x_e}{2} + \frac{\omega_e y_e}{4} + \frac{\omega_e z_e}{8}\right) \ (cm^{-1})$$

(= 0 for lowest vibrational level)

$$F(J) = BJ(J+1) - DJ^2(J+1)^2$$

Application to Molecular Hydrogen

Consider the ground state of H_2

$X^1\Sigma_g^+$
      $s = 0$

      $\Lambda = 0$

      $I = 1/2 \rightarrow T = 1, 0$

      even $J \rightarrow +$, s (symmetric under electron and nuclear
                              coordinate inversion)

      odd $J \rightarrow -$, a

Then

$$Q \simeq (1) [1 + \exp(-hc\omega_e/kT)](2s + 1) \ Q_{RN}$$

where the rotational-vibrational part of the homonuclear molecule cannot

be decoupled because of symmetry considerations, i.e.

$$Q_{RN} = \sum_{\substack{\text{all allowed} \\ \text{states}}} \exp(-E/kT) = \sum_{\text{allowed } T,J} (2T + 1)(2J + 1) \exp(-E_J/kT)$$

$$= \sum_{\text{even } J} (2J + 1) \exp(-hcF_J/kT) + 3 \sum_{\text{odd } J} (2J + 1) \exp(-hcF_J/kT)$$

$$= \sum_{J} (2J + 1) \exp(-hcF_J/kT) + 2 \sum_{\text{even } J} (2J + 1) \exp(-hcF_J/kT)$$

since only even T values are allowed for even J states. The above series can be truncated when the exponentials become sufficiently small. Then

$$Q(T) \simeq \left[1 + \exp\left(\frac{-6331}{T}\right)\right] Q_{RN}(T)$$

and

$$f_{vJ} = \frac{g_I(2J + 1)}{Q(T)} \exp\left[\frac{-hc}{kT} (T_e + \bar{G}(v) + F(J))\right]$$

$$= \frac{g_I(2J + 1)}{Q(T)} \exp\left[\frac{2170 - G(v) - F(J)}{.695T}\right]$$

where
$$g_I = 1 \text{ for even } J$$
$$= 3 \text{ for odd } J$$

Appendix D
Energy Differences Ω_J and Line Positions

The difference in energy between upper and lower energy levels participating in transitions Ω_{vJ} is

$$\Omega_{vJ} = E_{v'J'} - E_{v''J''}$$

where

$$E_{vJ} = hc(T_e + G(v) + F_s(J))$$

T_e = electronic energy (cm^{-1})
= 0 for ground state

$$G(v) = \omega_e(v + \tfrac{1}{2}) - \omega_e x_e(v + \tfrac{1}{2})^2 + \omega_e y_e(v + \tfrac{1}{2})^3 + \omega_e z_e(v + \tfrac{1}{2})^4 + \ldots$$

$$F_s(J) = B_v J(J + 1) - D_v J^2(J + 1)^2 + H_v J^3(J + 1)^3$$

$$B_v = B_e - \alpha_e(v + \tfrac{1}{2}) + \gamma_e(v + \tfrac{1}{2})^2$$

$$D_v = D_e + \beta_e(v + \tfrac{1}{2})$$

The subscript s differentiates electron spin components. For multiplet states there is an expression for each spin component characterized by a spin splitting constant. The form of the expression depends upon the angular momentum coupling employed.

For H_2 (all values in cm^{-1}, Ref 34)

ω_e = 4401.213*
$\omega_e x_e$ = 121.336*
$\omega_e y_e$ = 0.8129 *
$\omega_e z_e$ = 0.0

B_e = 60.8530
α_e = 3.0622 + 0.0577 $(v + \tfrac{1}{2})$ + 0.0051 $(v + \tfrac{1}{2})^2$
D_v = 0.0471 - 0.00274 $(v + \tfrac{1}{2})$ + 0.00040 $(v + \tfrac{1}{2})^2$
H_v = [4.9 - 0.5 $(v + \tfrac{1}{2})$]10^{-5}

* accurate for v = 0, 1, 2, 3.

In addition, each of the line positions is pressure shifted. To good approximation this shift can be written for the Q branch lines as

$$Q(J) = a_J\rho + b_J\rho^2$$

where ρ is the density and b_J is small and will be taken to be zero here. a_J is related to the relative population of the initial J^{th} level n_J/n [68]

$$a_J = a_o + a_c \frac{n_J}{n}.$$

For H_2, $a_o = -(2.0 \pm 0.2) \times 10^{-3}$, $a_c = -(1.7 \pm 0.4) \times 10^{-3}$ cm^{-1}/amagat at 300 K.

Appendix E
Analytical Form of Anti-Stokes Spectrum

The formula for the general case of a broadband Stokes laser of Gaussian profile and narrow, but finite band pump laser beams is given by Eq. (55) of Yuratich [12]:

$$S_{as}(\omega_{as}) = [\exp(-\delta_{as}/\tilde{\gamma}_{2d}^2)/(\pi\tilde{\gamma}_{2d})]$$

$$\times \left\{ \chi_{NR}^2 - \frac{2\sqrt{\pi}\ \tilde{\gamma}_{2d}}{\tilde{\gamma}_2\ \tilde{\gamma}_d} \sum_j \chi_{NR}\ a_j \mathrm{Im}(\bar{w}_j) - \frac{\sqrt{\pi}\ \tilde{\gamma}_{2d}}{\tilde{\gamma}_2\tilde{\gamma}_d} \sum_{j,k} a_j a_k \mathrm{Im}\left(\frac{\bar{w}_j + \bar{w}_k^*}{\Delta_{kj} + i(\tilde{\gamma}_k + \tilde{\gamma}_j)} \right) \right\}$$

where $\bar{w}_j = w\left(\dfrac{n_{2d}\delta_{as} - \Delta_j + i\gamma_j}{\tilde{\gamma}_2\tilde{\gamma}_d/\tilde{\gamma}_{2d}} \right)$

and $w(z)$ is the complex error function given by

$$w(z) = \exp(-z^2) \left[1 + \frac{2i}{\sqrt{\pi}} \int_0^z \exp(t^2)dt \right]$$

$$= \frac{i}{\pi} \int_{-\infty}^{\infty} \frac{\exp(-t^2)}{z-t} dt, \quad \mathrm{Im} z > 0.$$

$$a_j = \frac{Nn_1 c^4}{\hbar n_2 \omega_2^4} \Delta_j \left. \frac{d\sigma}{d\Omega} \right|_j$$

$\delta_{as} = \omega_{as} - \omega_{as}^o$;
$\qquad\qquad\qquad$ $\gamma_d = (\gamma_1^2 + \gamma^2)^{\frac{1}{2}}$

$\gamma_{2d} = (\gamma_2^2 + \gamma_d^2)^{\frac{1}{2}}$;
$\qquad\qquad\qquad$ $n_{2d} = (1 + \gamma_2^2/\gamma_d^2)^{-1} = (\gamma_d/\gamma_{2d})^2$

$\Delta_{kj} = \bar{\Delta}_k - \bar{\Delta}_j$;
$\qquad\qquad\qquad$ $\bar{\Delta}_j = \Omega_j - (\omega_1^o - \omega_s^o)$

$\tilde{\gamma} = \gamma/\sqrt{\ell n2}$

ω_{as}^o, ω_s^o, ω_1^o = the anti-Stokes, Stokes, and pump center angular
$\qquad\qquad\qquad$ frequencies, respectively.

γ_1, γ_2, γ_s, γ_j = the pump #1, pump #2, Stokes, and Raman
$\qquad\qquad\qquad$ linewidths (HWHM), respectively

Ω_j = Raman resonance angular frequency (calculated in Appendix D).

73

Appendix F
Computed H_2 CAR Spectra

The following figures show calculated H_2 CAR spectra for a range of temperatures: $800 \leq T \leq 1800$ K, $\Delta T = 100$ K. Each figure consists of four spectra at the same temperature but computed with differing number density and Stokes beam width: $\rho = 1$ and 100 amagat; $\Gamma_s = 100$ and 250 cm^{-1}. The other fixed parameters assumed for the computation are:

Stokes beam center	14679 cm^{-1} (5812 Å)
pump beam center	18797 cm^{-1} (5320 Å)
pump beam width (FWHM)	.8 cm^{-1}

Each spectrum is normalized to the maximum peak intensity of that spectrum. Instrument profile convolution is not included.
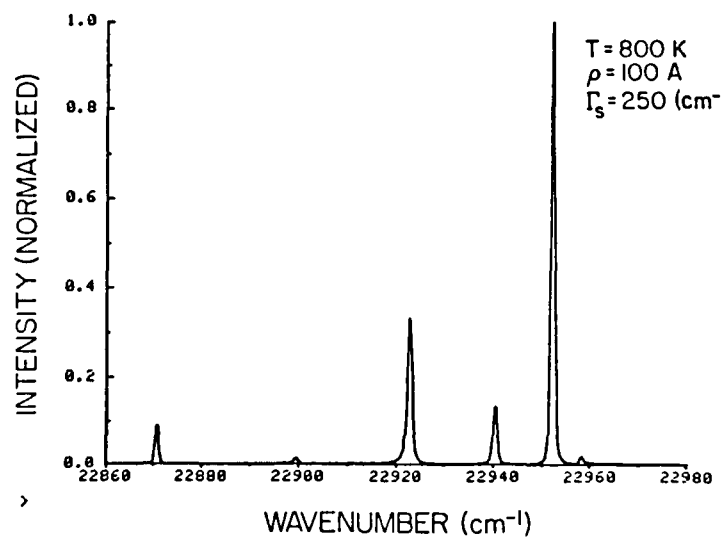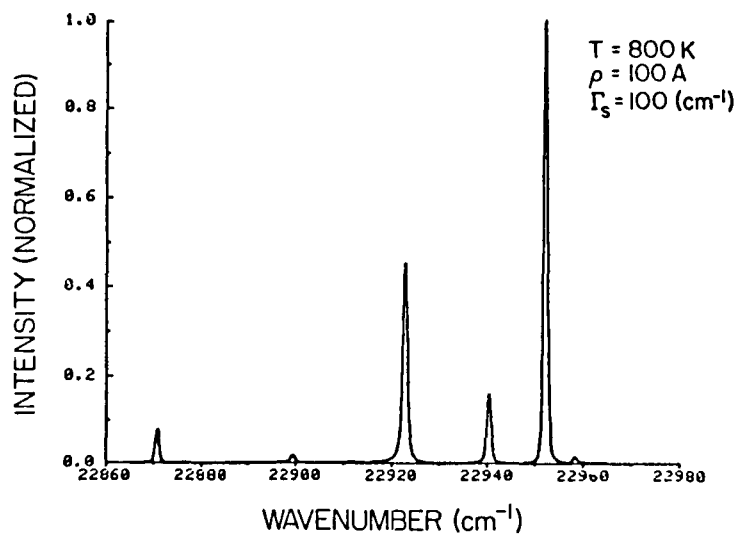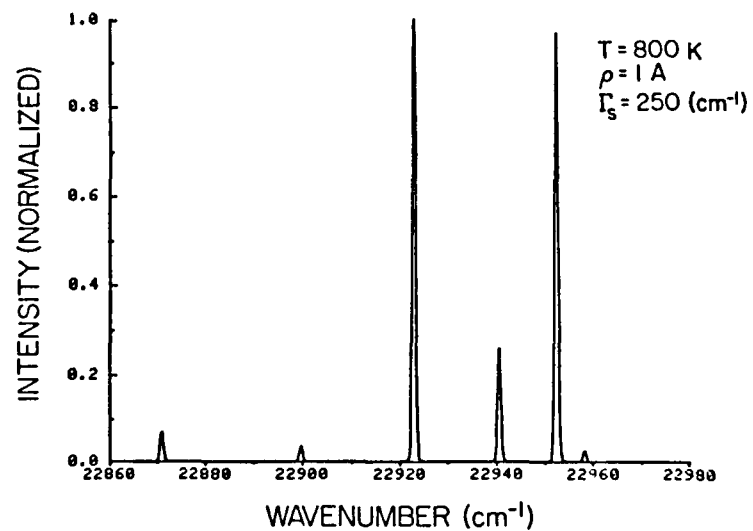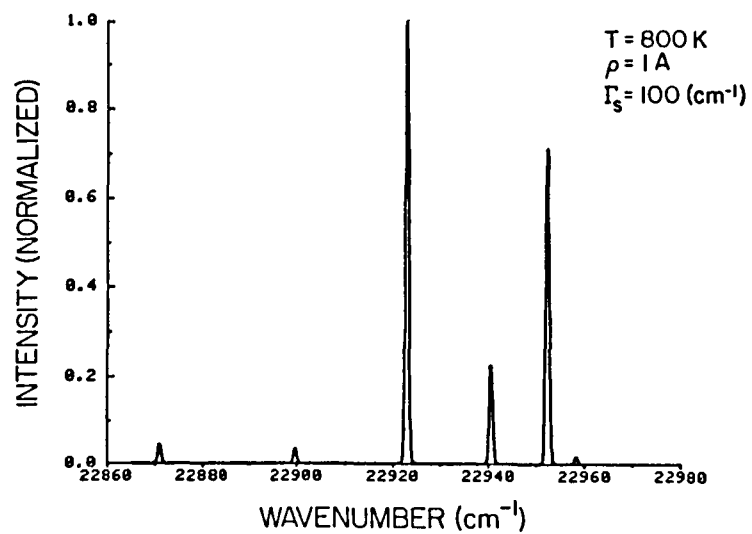
F. 1. Computed H_2 CAR Spectra at T = 800 K.
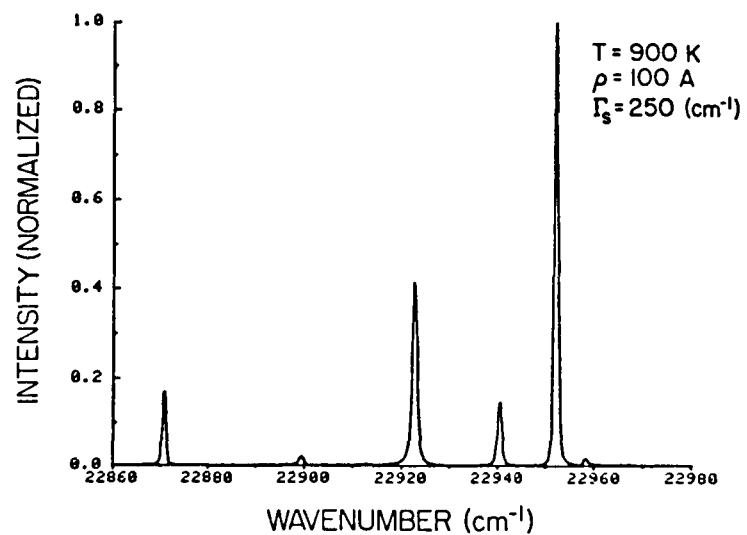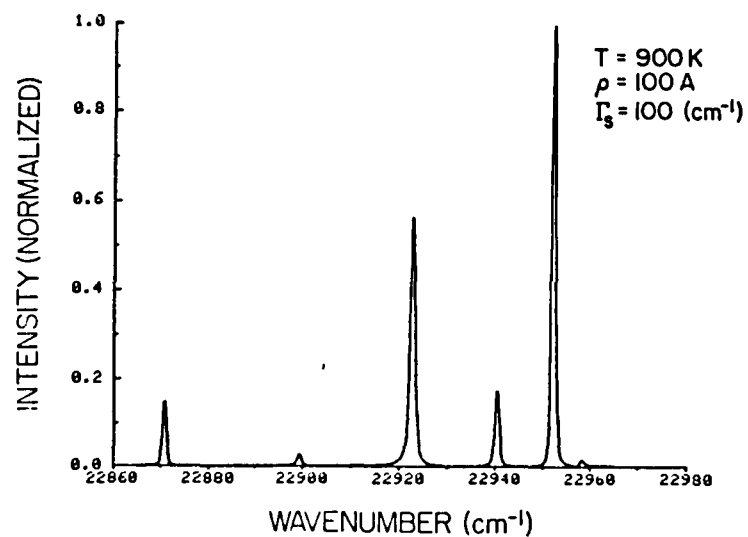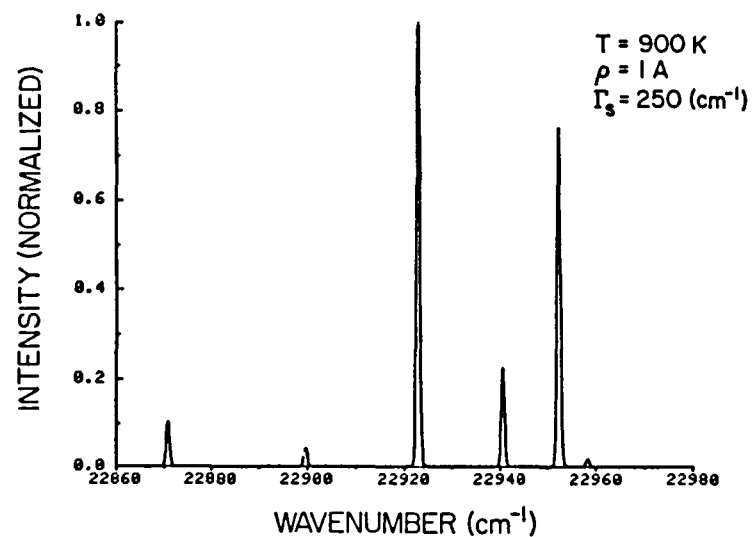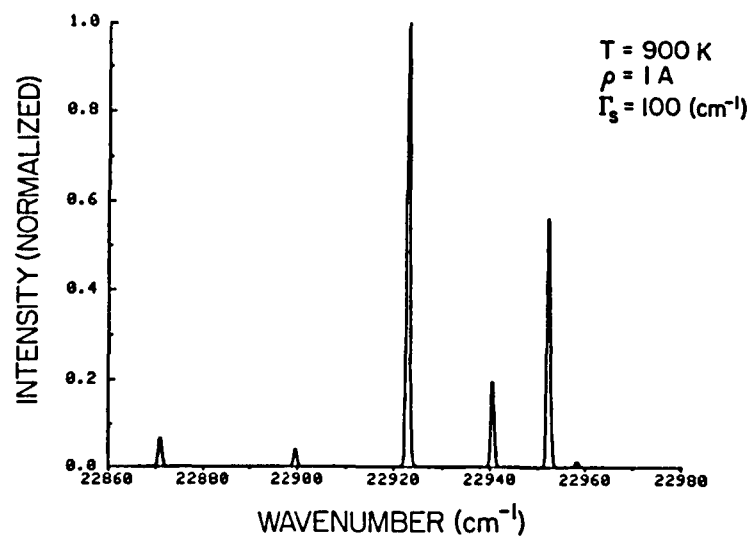
F. 2. Computed H_2 CAR Spectra at T = 900 K.
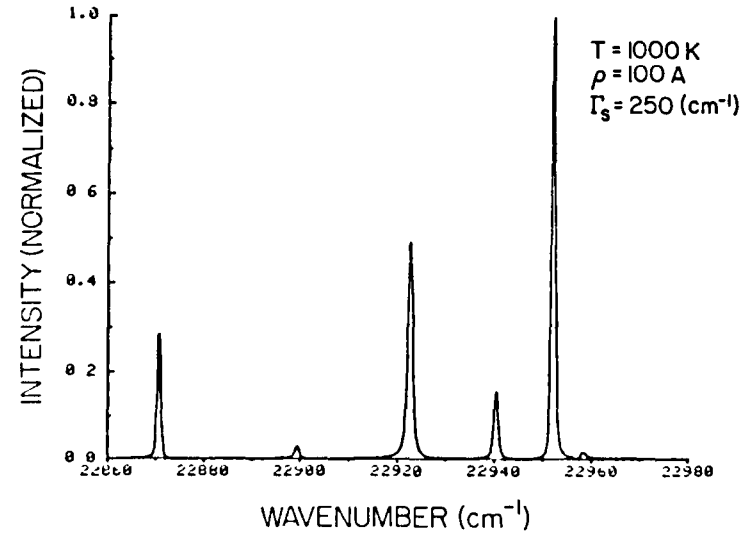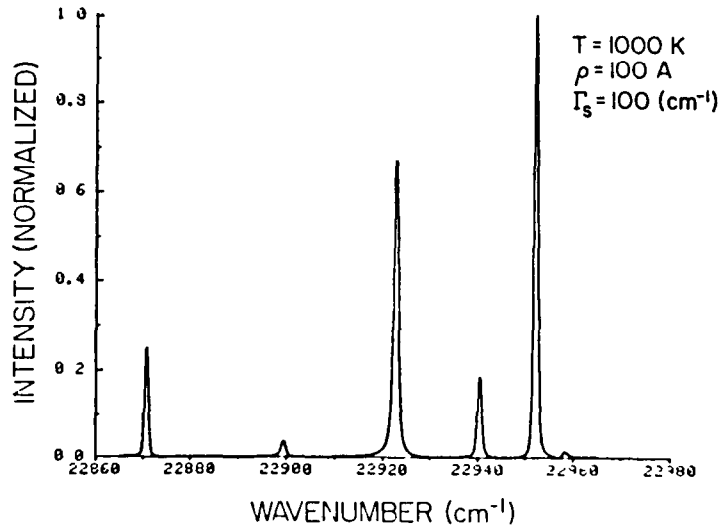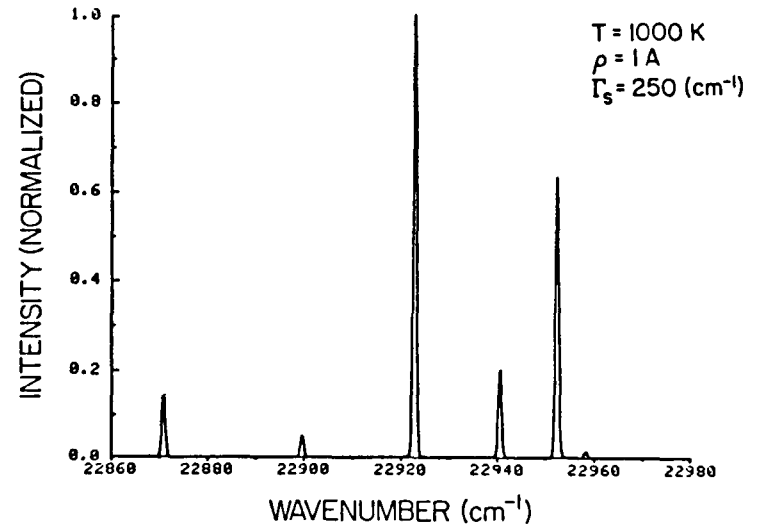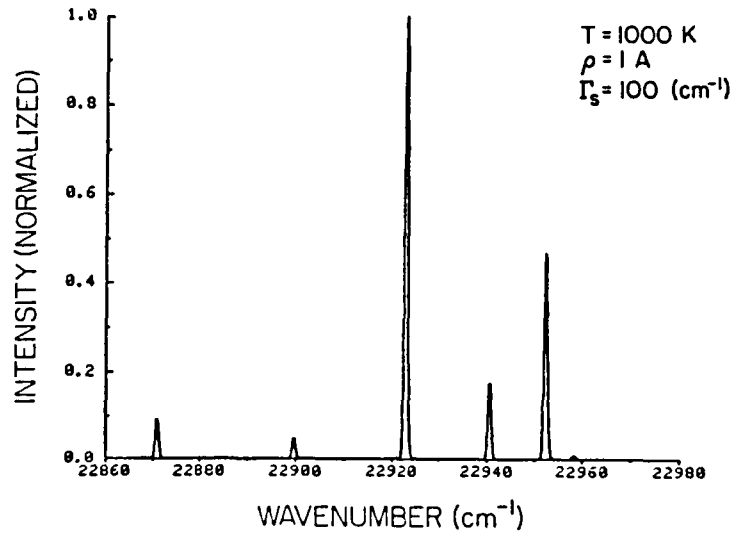
F. 3. Computed H_2 CAR Spectra at T = 1000 K.
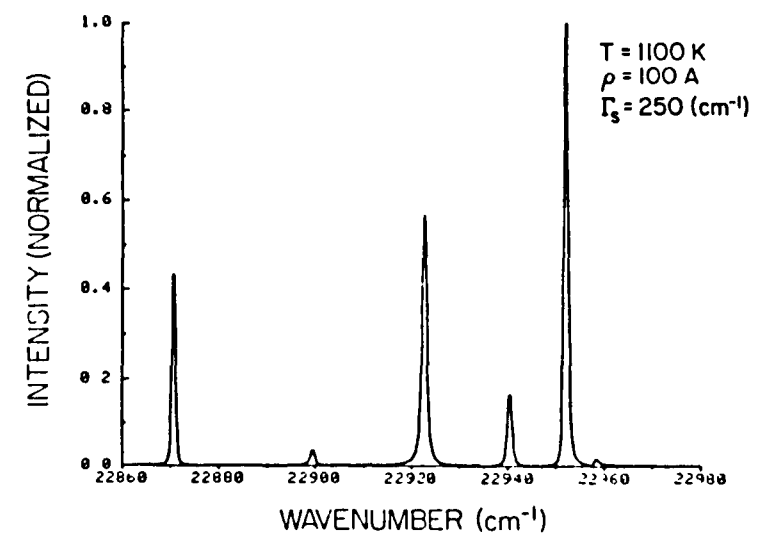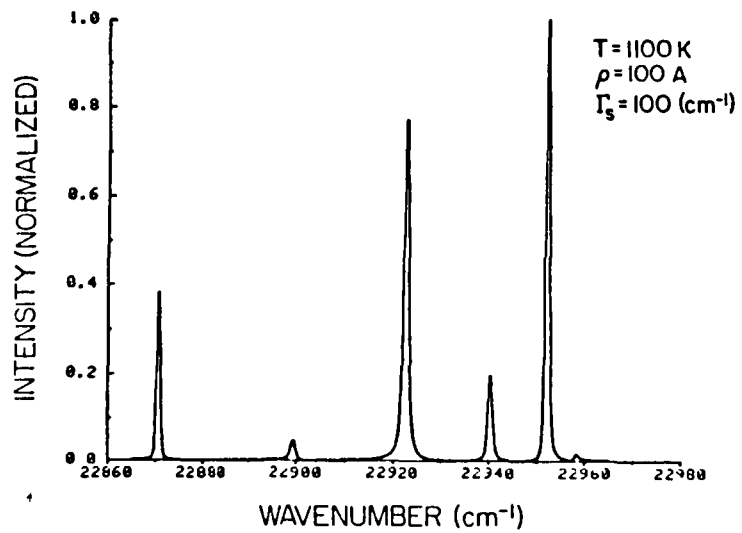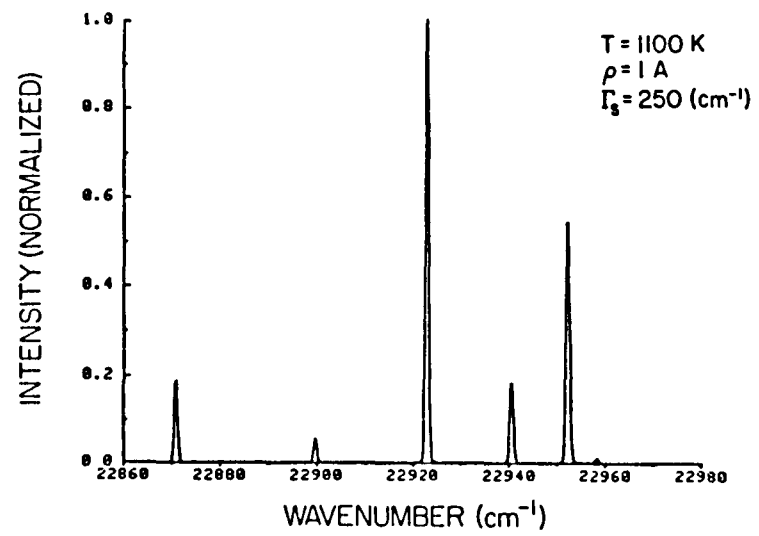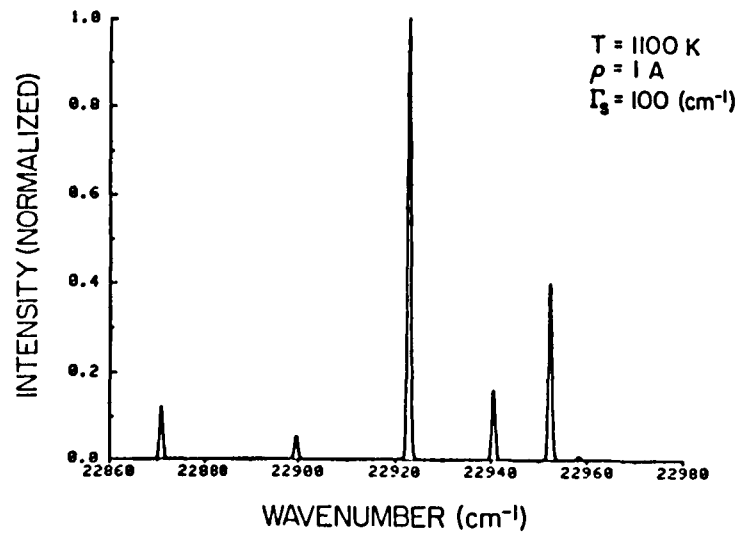
F. 4. Computed H_2 CAR Spectra at T = 1100 K.
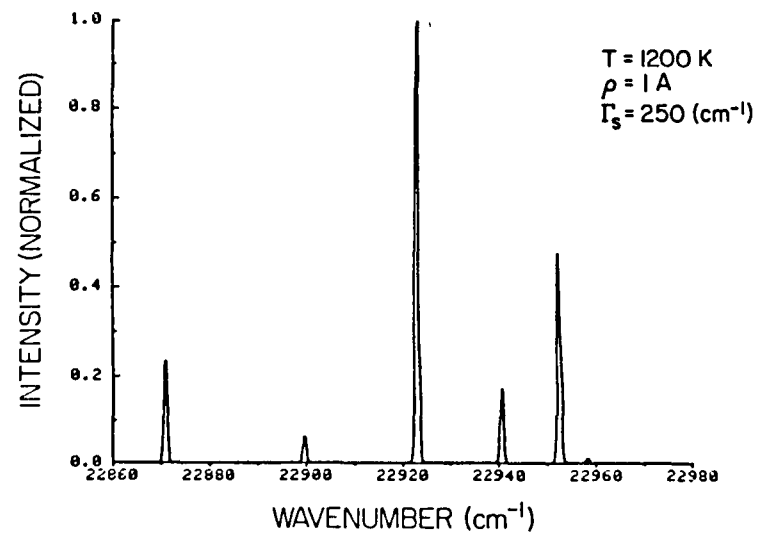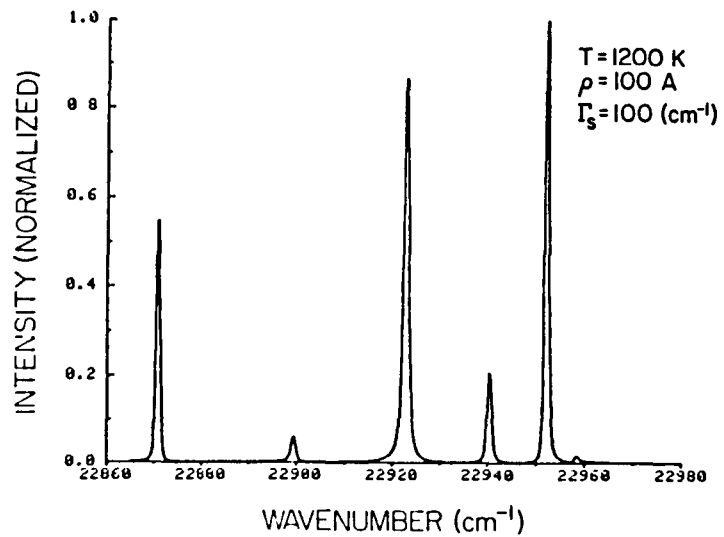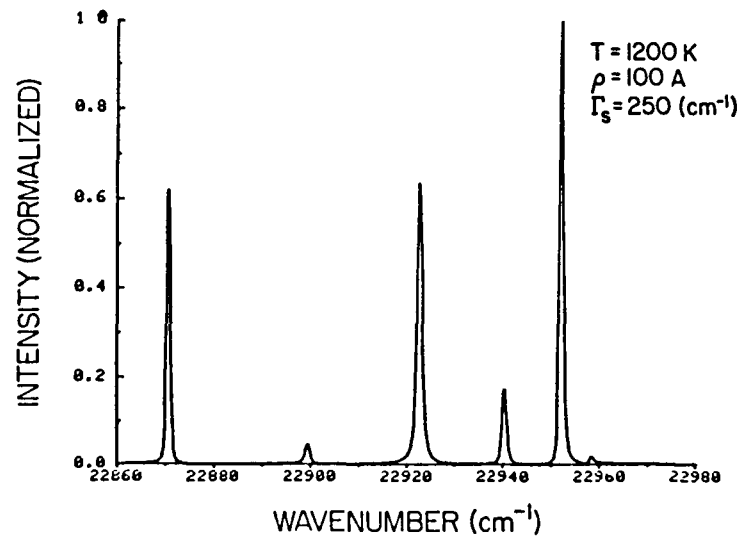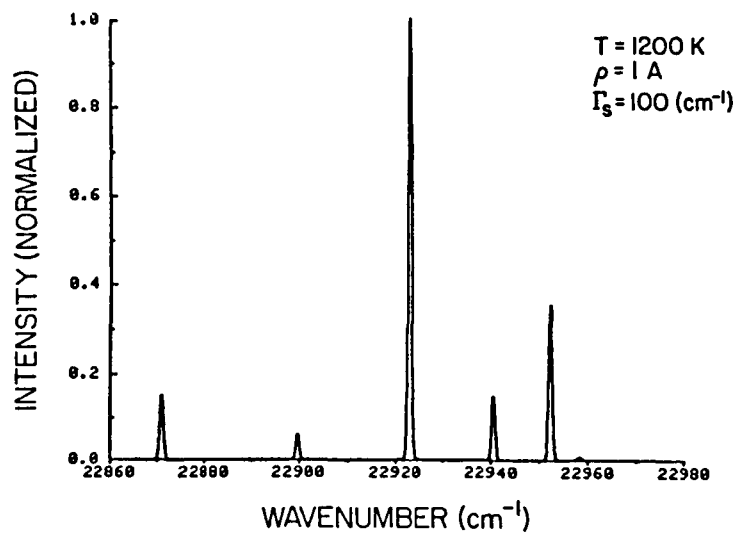
F. 5. Computed H_2 CAR Spectra at T = 1200 K.
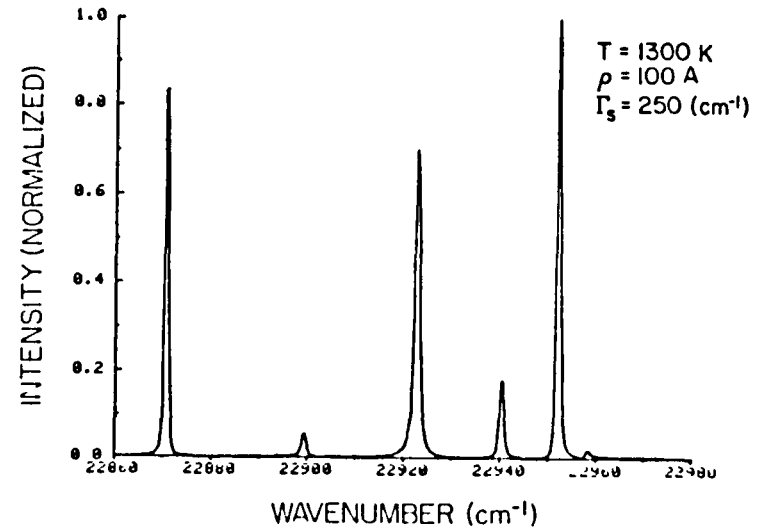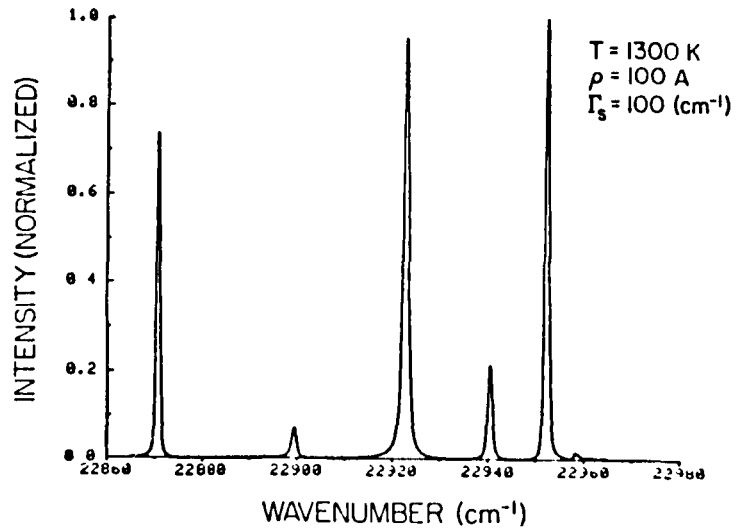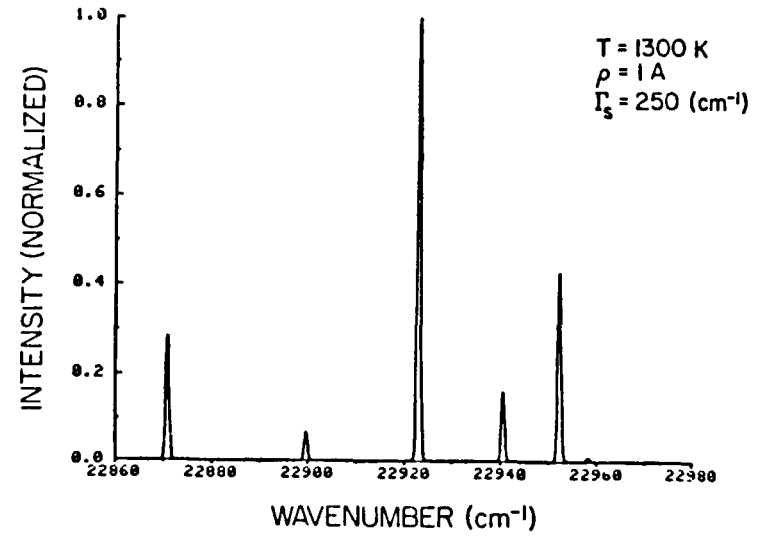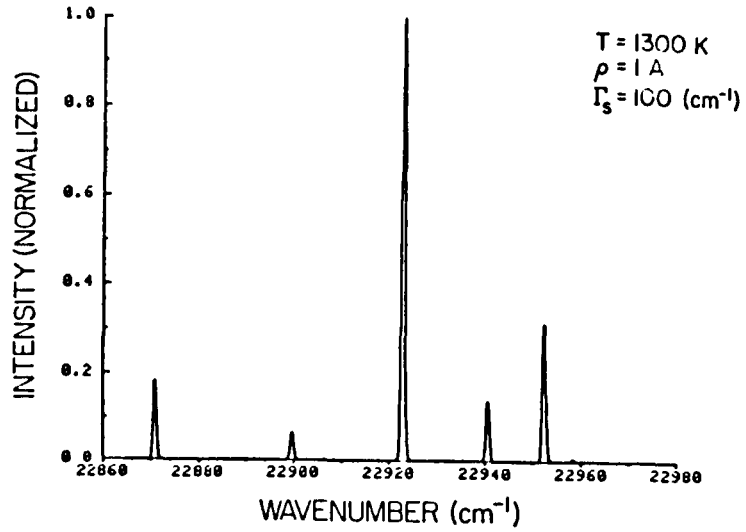
F. 6. Computed H_2 CAR Spectra at T = 1300 K.
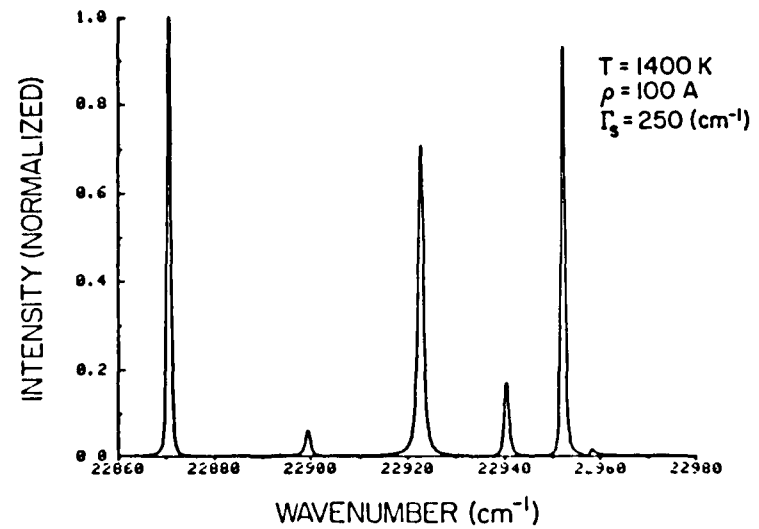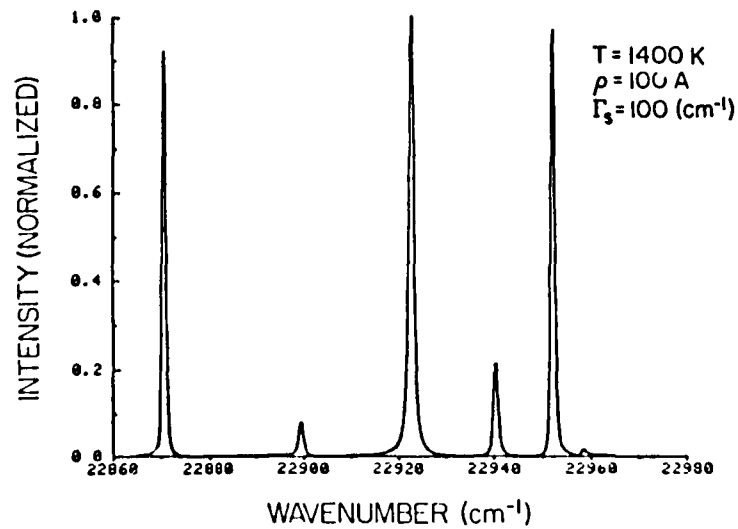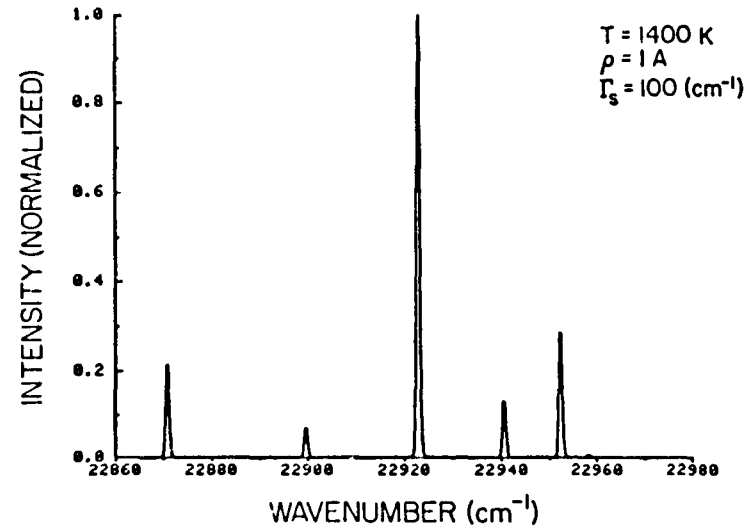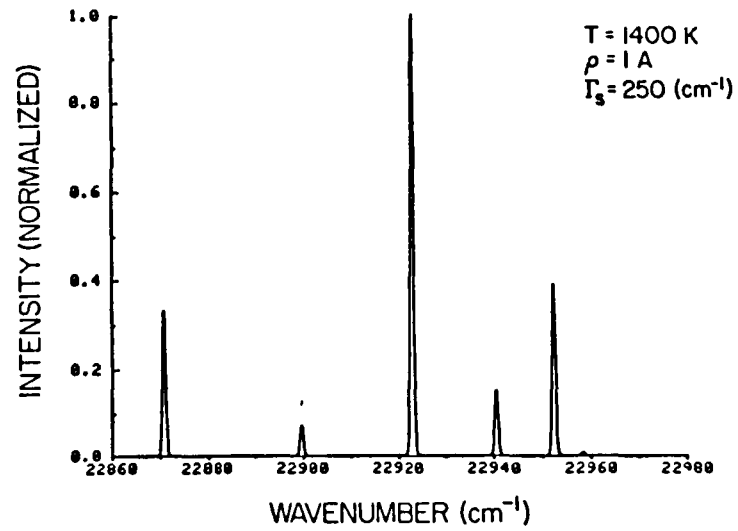
F. 7. Computed H_2 CAR Spectra at T = 1400 K.
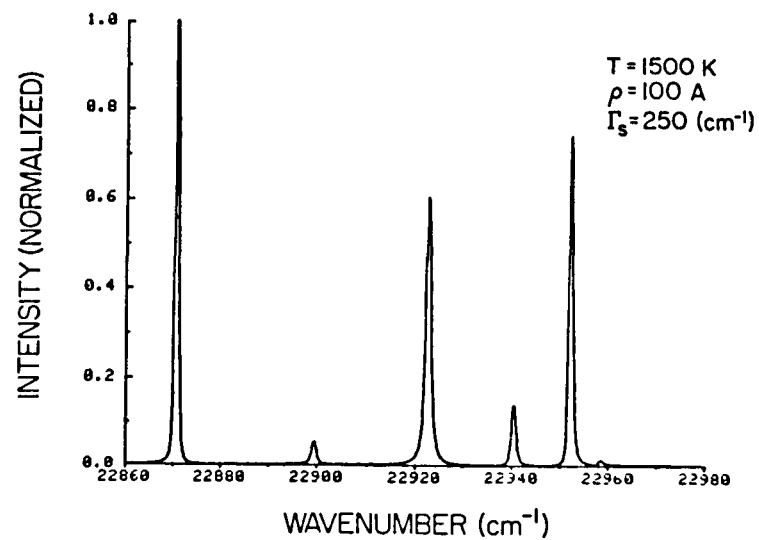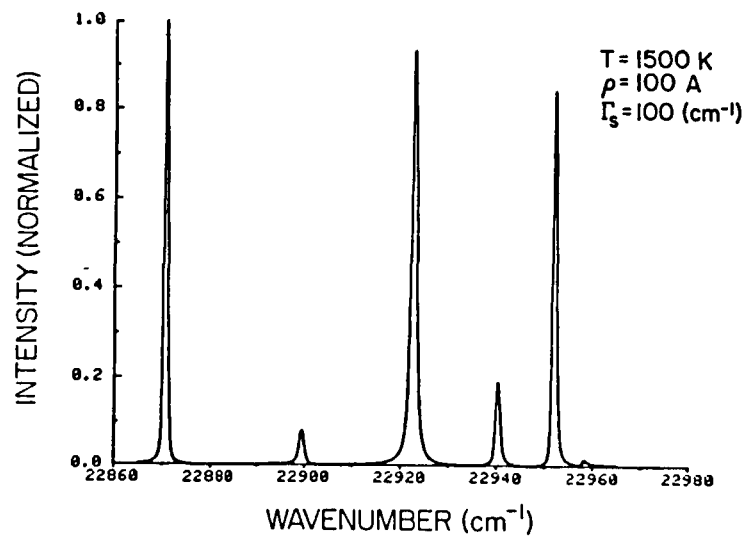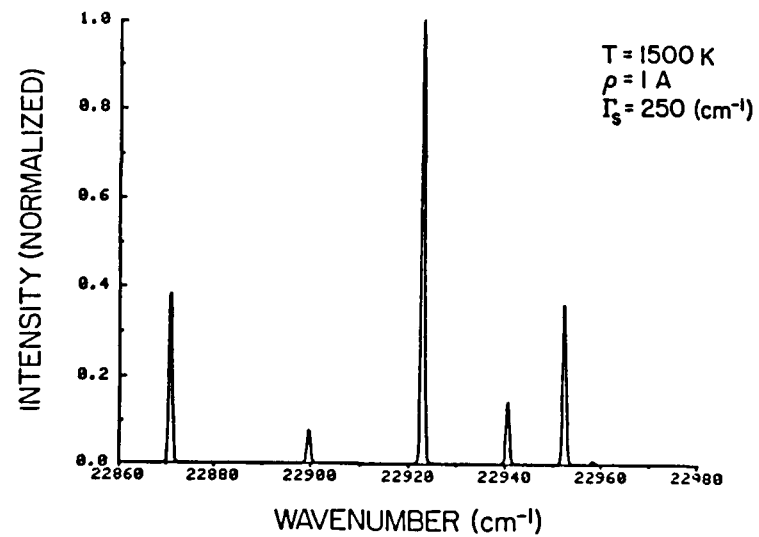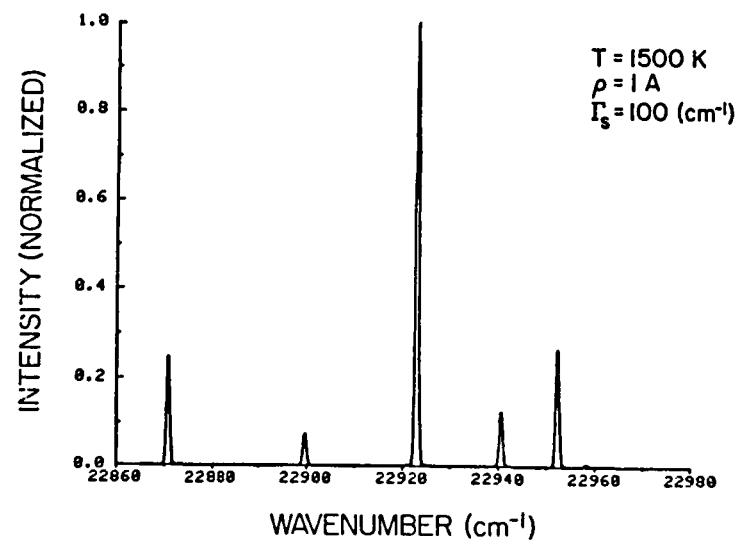
F. 8.   Computed H_2 CAR Spectra at T = 1500 K.
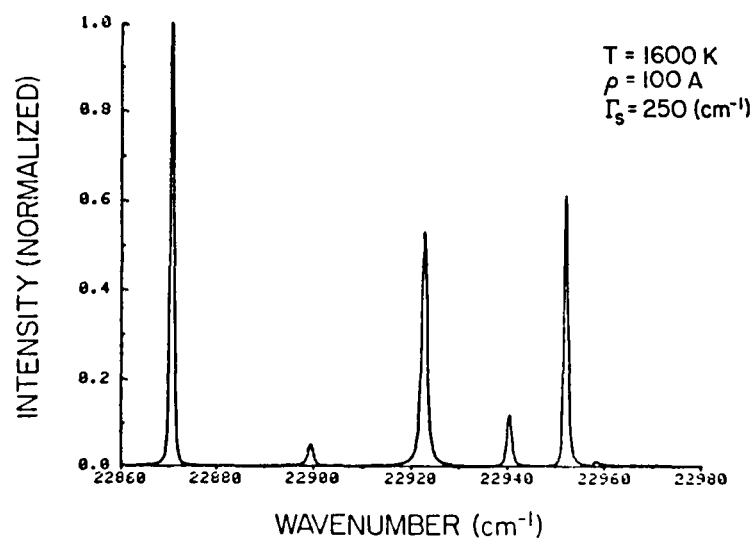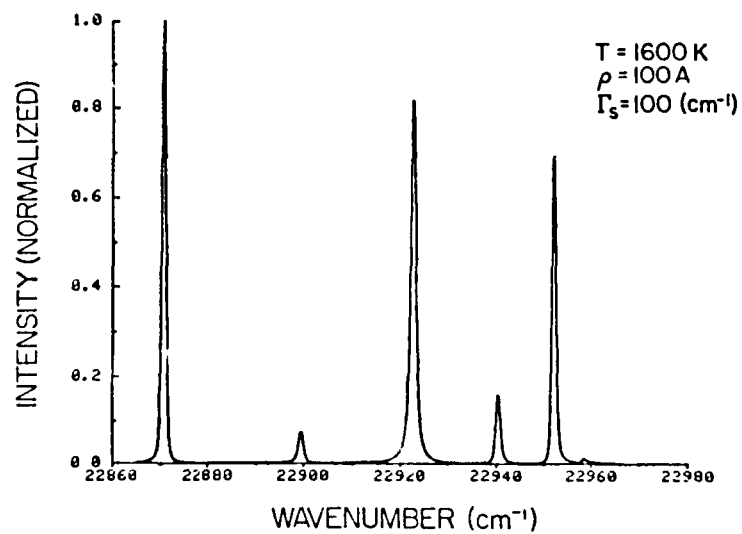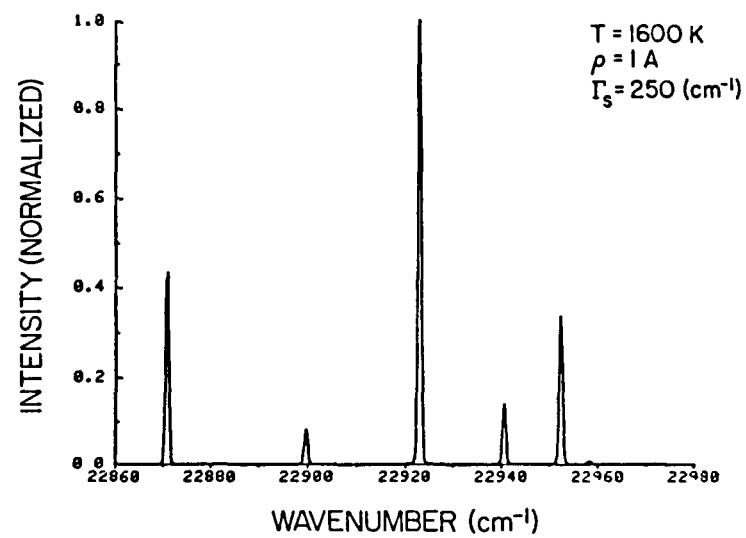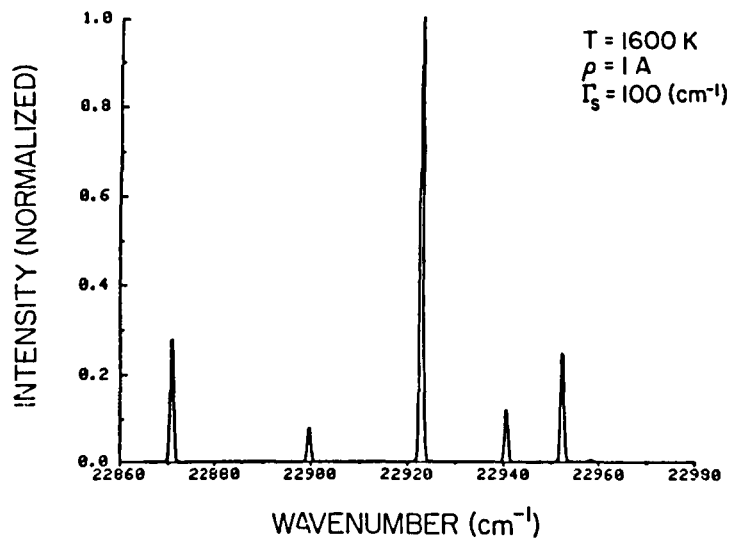
F. 9.   Computed H_2 CAR Spectra at T = 1600 K.
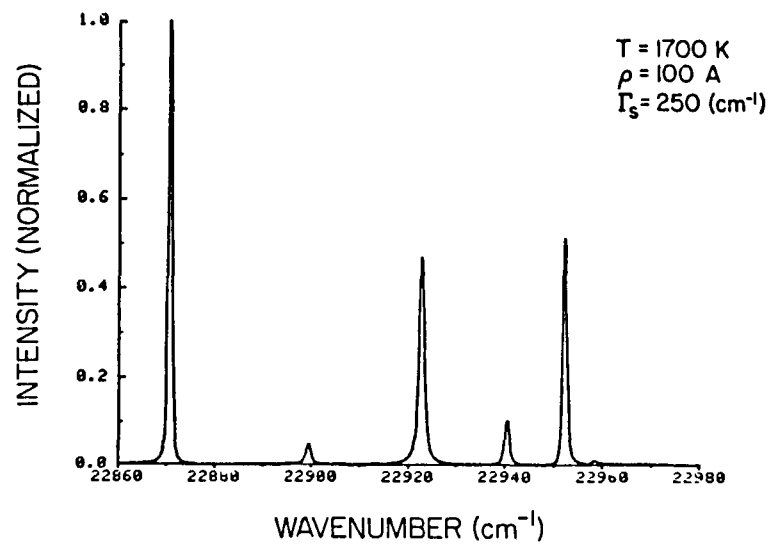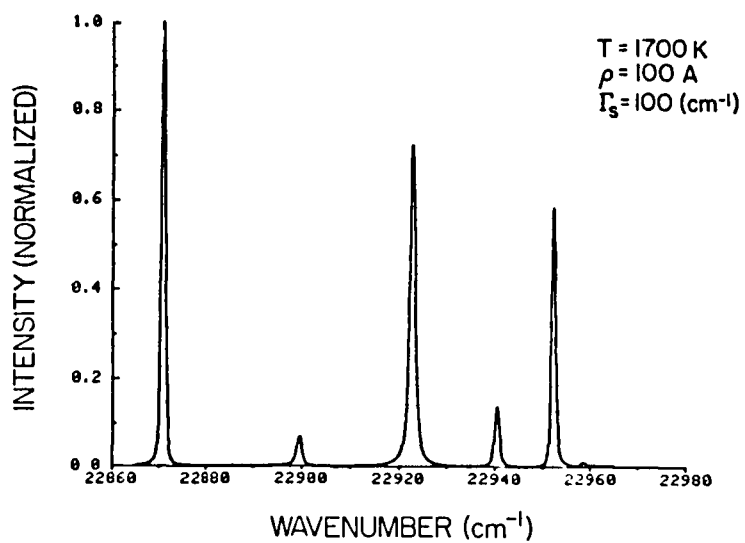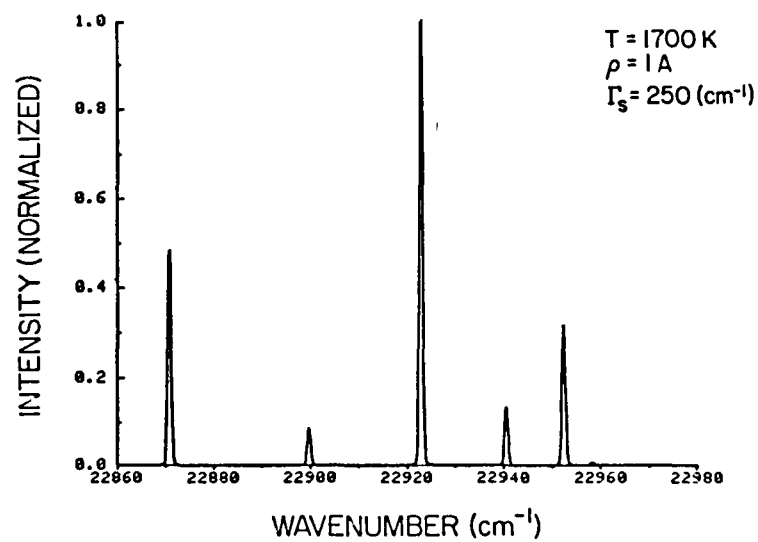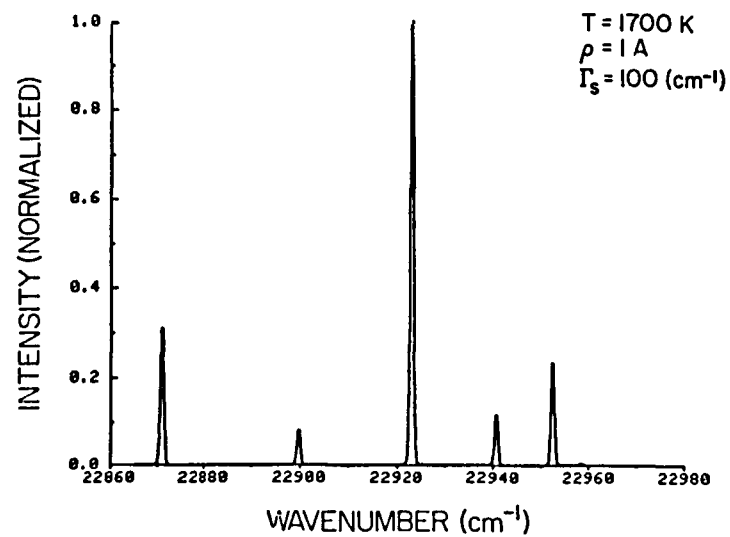
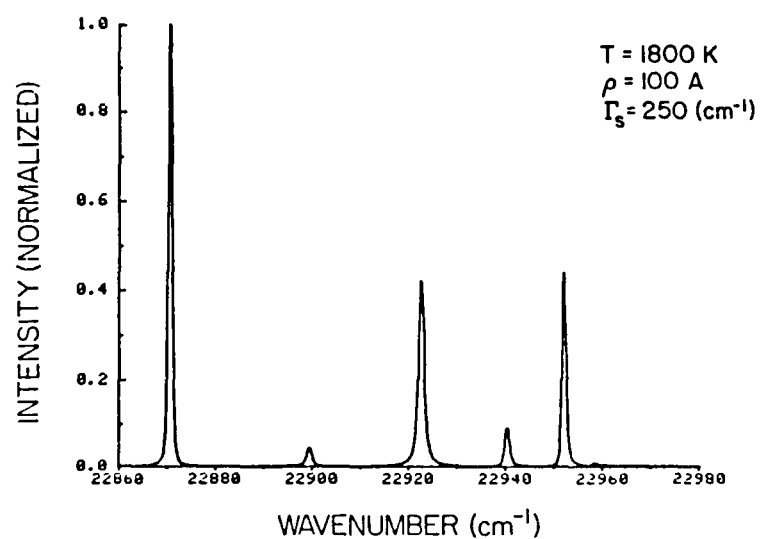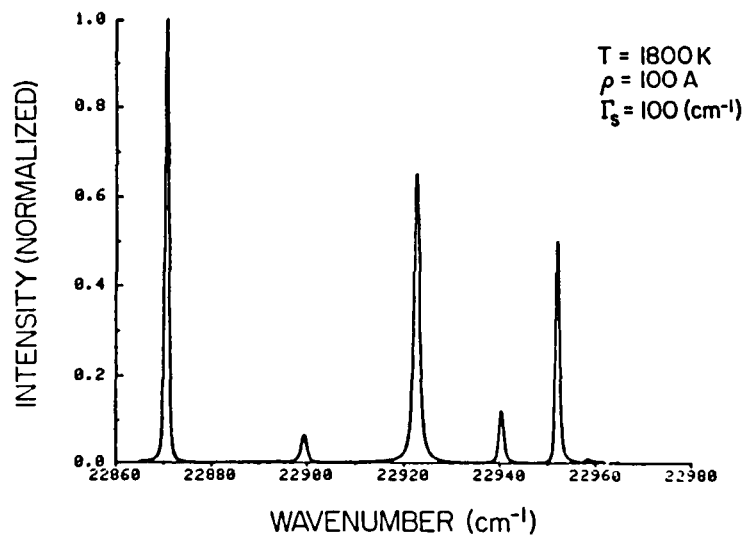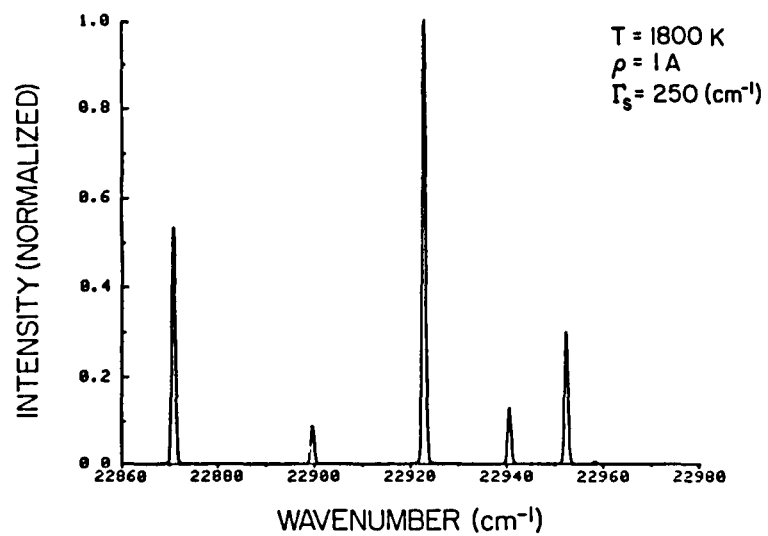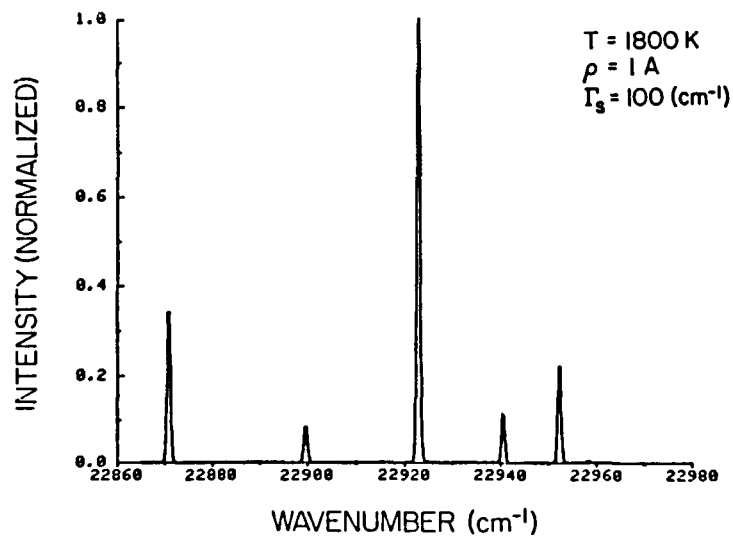F. 10.   Computed H_2 CAR Spectra at T = 1700 K.

F. 11. Computed H_2 CAR Spectra at T = 1800 K.

References

1. Eckbreth, A.C., Combust. Flame 39, 133 (1980).

2. Switzer, G.L., L.P. Gross, W.M. Roquemore, R.P. Bradley, P.W. Schreiber, and W.B. Roh, J. Energy 4, 209 (1980).

3. Attal, B., M. Pealat, and J.P. Taran, J. Energy 4, 135 (1980).

4. Druet, S. and J.P. Taran, "Coherent Anti-Stokes Raman Spectroscopy" in Chemical and Biological Applications of Lasers, Vol. 4, Academic Press, New York (1979) p. 187.

5. Nibler, J.W. and G.V. Knighten, Coherent Anti-Stokes Raman Spectroscopy in Topics in Current Physics, Vol. II, A. Weber, Ed., Chapter 7, Springer Verlag, Stuttgart (1977).

6. Shirley, J.A., A.C. Eckbreth, and R.J. Hall. Proceedings of the 16th JANNAF Combustion Meeting, CPIA Publication 309, 487 (1979).

7. Shirley, J.A., A.C. Eckbreth, and R.J. Hall, "Investigation of the Feasibility of CARS Measurements in Scramjet Combustion," Technical Report R79-954390-8 under Contract NASA1-15491, (1979).

8. Hall, R.J., Combust. Flame 35, 47 (1979).

9. Flytzanis, C., in Quantum Electronics: A Treatise, ed. by H. Rabin, C.L. Tang, Vol. 1 Academic Press, New York, (1975) p. 9.

10. Nibler, J.W. and G.V. Knighten, in Topics in Current Physics, Vol. II, Raman Spectroscopy of Gases and Liquids, ed. by A. Weber.

11. Easley, G.L., J. Quant. Spectro. Radiat. Transfer 22, 507 (1979).

12. Yuratich, M.A., Mole Phys. 38, 625 (1979).

13. Beiting, E.J., and J.C. Luthe (1982). Synthetically produced CAR spectra of N_2. Testing and Evaluation of Heat Recovery/Seed Recovery, Quarterly Report April-June 1982, Mississippi State University MHD Center Report FE-15601-9, Mississippi State, MS 39762, U.S.A.

14. Hall, R.J., Combust. Flame 35, 47 (1979).

15. Placzek, G. and E. Teller, Z. Physik 81, 209 (1933).

16. Hall, R.J. Appl. Spectro. 34, 700 (1980).

17. Eckbreth, A.C. and R.J. Hall, "CARS Concentration Sensitivity with and without Nonresonant Background Suppression", UTRC Report #R80-954628-1.

18. Weber, A. "High Resolution Studies of Gases" in The Raman Effect ed. A. Anderson, Marcel Dekker, New York, 1973.

19. Dicke, R.H. Phys. Rev. 89, 472 (1953).

20. Murray, J.R. and A. Javan, J. Mole. Spectro. 29, 502 (1969).

21. Hunt, R.H., W.L. Barnes and P.J. Brannon, Phys. Rev. A 1, 1570 (1970).

22. Allin, E.J., A.D. May, B.P. Stoicheff, J.C. Stryland, and H.L. Welsh, Appl. Opt. 6, 1597 (1967).

23. Henesian, M.A. and R.L. Byer, J. Opt. Soc. Am. 68, 648 (1978).

24. Galatry, L., Phys. Rev. 122, 1218 (1961).

25. Lallemand, P., P. Simova, and G. Bret, Phys. Rev. Lett. 17, 1239, 1966.

26. Jost, W., "Diffusion in Solids, Liquids, Gases" Academic Press, N.Y., 1952.

27. Owyoung, A., Opt. Lett. 2, 91 (1978).

28. Harteck, P. and H.W. Schmidt, Zeit. Phys. Chem. Abt. B 21, 447 (1933).

29. Van Kranendonk, J., Can. J. Phys. 41, 433 (1963).

30. Lellemand, P. and P. Simova, J. Mole. Spectro 26, 262 (1968).

31. Brannon, P.J., C.H. Church, and C.W. Peters, J. Mole Spectro. 27, 44 (1968).

32. St. Peters, R.L., Opt. Letts. 4, 402 (1979).

33. May, A.D., V. Degen, J.C. Stryland and H.L. Welsh, Can. J. Phys. 39, 1769 (1961).

34. Foltz, J.V., D.H. Rank and T.A. Wiggins, J. Mole. Spectro. 21, 1966.

35. Regnier, P.R., F. Moya and J.P. Taran, AIAA 12, 826 (1974).

36. Barrell, H. and J.E. Sears, Trans. Roy. Soc. A 238, 1 (1939).

37. Owens, J.C., Appl. Opt. 6, 51 (1967).

38. Born, M. and E. Wolf, "Principles of Optics," 2nd edition, MacMillan Co., New York (1964) p. 94.

39. Koch, J., Nov. Act. Soc. Ups. 2, 61 (1909).

40. Wilke, V. and W. Schmidt, Appl. Phys. 18, 177 (1979).

41. Regnier, P.R., F. Moya, J.P. Taran, AIAA 12, 826 (1974).

42. Byer, R.L., Electro-Optical Systems Design, Feb. 1980, p. 24.

43. Loree, T.R., R.C. Sze, D.L. Barker, P.B. Scott, IEE J. Quant. Electro. 15, 337 (1979).

44. Brink, D.J. and D. Prock, Opt. Lett. 7, 494 (1982).

45. Raizer, Yu.P., "Laser Induced Discharge Phenomena", Consultants Bureau, New York (1977).

46. Minck, R.W. and W.G. Rado, Physics of Quantum Electronics (Proc. Intern. Conf. San Juan, Puerto Rico, 1965), P. L. Kelley el at. ed., McGraw-Hill, New York (1966), p. 527.

47. Gill, D.H. and A.A. Dougal, Phys. Rev. Lett. 15, 845 (1965).

48. Minck, R.W., J. Appl. Phys. 35, 252 (1964).

49. Brown, S.C., "Basic Data of Plasma Physics", MIT Press, Cambridge, Mass. (1959).

50. Haught, A.F., R.G. Meyerland, D.C. Smith, Physics of Quantum Electronics of Quantum Electronics (Proc. Intern. Conf. San Juan, Puerto Rico, 1965), P.L. Kelley et al. ed., McGraw-Hill, New York (1966), p. 509.

51. Bevington, P.R., "Data Reduction and Error Analysis for the Physical Sciences", McGraw-Hill, New York (1969).

52. Eckbreth, A.C. and R.J. Hall, Combust. Flame 36, 87 (1979).

53. Beiting, E.J., CARS: Longitudinal pumping geometry for the dye laser, *Testing and Evaluation of Heat Recovery/Seed Recovery*, Quarterly Report January-March 1981, Mississippi State University, MHD Energy Center, Report FE-15601-4.

54. Adolf Meller Co. catalogue, "Electronic Optical Laser Materials and Components," Providence, Rhode Island.

55. Handbook of Chemistry and Physics, 49th Edition, R.C. Weast, editor in chief, Chemical Rubber Co., Cleveland, Ohio (1968).

56. Murphy, W.F., W. Holzer, and H.J. Bernstein, Appl. Spectro. 23, 211 (1969).

57. Penny, C.M., L.M. Goldman, and M. Lapp, Nature Phys. Sci. 235, 110 (1971).

58. Abbate, S., M. Gussoni, J. Mole Spectro. 73, 415 (1978).

59. Bhagavatam, S., "Scattering of Light and the Raman Effect", Andhra University, Waltais, India.

60. Stoicheff, B.P., "High Resolution Raman Spectroscopy" in Advances in Spectroscopy, ed. by H.W. Thompson, Interscience Publishers, Inc., New York (1959).

61. Gaufres, S. and S. Sportouch, J. Mole. Spectro. 39, 527 (1971).

62. Bovanich, J.P. and C. Brodbech, J. Quant. Spectro. Radiat. Trans. 16, 153 (1976).

63. Hall, R.J. and A.C. Eckbreth "CARS: Application to Combustion Diagnostics" in Laser Applications V, R.K.Erf. ed. Academic Press (1982).

64. Dunham, J.L., Phys. Rev. 41, 721 (1932).

65. Crawford, F.H., and T. Jorgensen, Jr., Phys. Rev. <u>49</u>, 745 (1936).

66. Mayer, J.E., and M. Goeppert-Mayer, <u>Statistical Mechanics</u>, John Wiley & Sons, New York, (1940).

67. Herzberg. G., <u>Molecular Spectra and Molecular Structure I</u>, "Spectra of Diatomic Molecules", Van Nostrand, Reinhold, New York (1950).

68. May, A.D., G. Varghese, J.C. Stryland, and H.L. Welsh, Can. J. Phys. <u>42</u>, 1058 (1964).

End of Document